

2019-12-17

# Ligand Design for Energy Conversion and Storage Applications

Heidebrecht, Joshua

---

Heidebrecht, J. (2019). Ligand Design for Energy Conversion and Storage Applications (Master's thesis, University of Calgary, Calgary, Canada). Retrieved from <https://prism.ucalgary.ca>.  
<http://hdl.handle.net/1880/111355>

*Downloaded from PRISM Repository, University of Calgary*

UNIVERSITY OF CALGARY

Ligand Design for Energy Conversion and Storage Applications

by

Joshua Heidebrecht

A THESIS

SUBMITTED TO THE FACULTY OF GRADUATE STUDIES  
IN PARTIAL FULFILMENT OF THE REQUIREMENTS FOR THE  
DEGREE OF MASTER OF SCIENCE

GRADUATE PROGRAM IN CHEMISTRY

CALGARY, ALBERTA

DECEMBER, 2019

© Joshua Heidebrecht 2019

## Preface

The negative impact of global warming on climate resulted in an overall ambient temperature increase of roughly 0.9 °C since the mid-nineteenth century, with an additional 0.2 °C expected for every incoming decade if the current trends persist.<sup>[1]</sup> As subtle as it may seem, this increase in temperature has major environmental implications through melting icecaps, raising ocean levels, ocean acidification, diminished agricultural production, increasing frequency of natural disasters, and reduction in biodiversity.<sup>[2–4]</sup> As carbon dioxide, CO<sub>2</sub>, is the most significant component of the greenhouse gases of anthropogenic origin (82% in the US), there has been a substantial effort in bringing society closer to “carbon neutrality” through the use of renewable energy sources and the reduction of coal-generated electricity. The target recommended by the Paris Agreement aims to limit global warming to less than 2 °C since the pre-industrial era.<sup>[1]</sup> However, even if all large-scale energy production was sourced through renewable technology, petroleum-based CO<sub>2</sub> emissions would persist through applications such as air transportation, which require high energy density fuels that novel battery technologies cannot compete with. To adhere to a closed carbon cycle, advancements in CO<sub>2</sub> sequestration and conversion to fuels is important, in addition to the implementation of renewable energy. This thesis will focus on advancing two areas of research aimed at mitigating the rise in atmospheric CO<sub>2</sub> concentration. Chapters 1 and 2 will outline progresses in grid energy storage using redox flow batteries (RFBs), aimed at enabling an increased proportion of renewable (mainly solar and wind) energy to be connected to the grid. Chapters 3, 4 and 5 will describe attempts at the electrocatalytic reduction of CO<sub>2</sub> to carbon monoxide (CO), which can be reconverted to fuels and create a carbon-neutral fuel cycle.

## Abstract

The contents of this thesis are divided into two topics that fall under the umbrella of energy conversion and storage. The first section focuses on tuning the standard reduction potential of the  $\text{Fe}^{3+/2+}$  redox couple with the aid of nitrogen-based ligands, in pursuit of an all-iron, water-based redox-flow battery. Also included is the synthesis and characterization of iron coordination complexes with redox-active ligands featuring quinone/hydroquinone functional groups. This study aims to exploit the potential of this system incorporating  $\text{Fe}^{3+/2+}$  and a redox non-innocent ligand for application in single-component redox-flow batteries.

The second portion of the thesis targets homogeneous single-site catalysts for the electrochemical reduction of  $\text{CO}_2$ . The ability of nickel and iron complexes incorporating a redox non-innocent bis(triazapentadienyl) ligand to promote this transformation was investigated. The nickel complex was identified as more promising and infrared spectroelectrochemistry was used to determine the fate of the metal during controlled potential electrolysis, as well as to identify the extent to which a large excess of ligand-based redox behavior impacts electrocatalytic  $\text{CO}_2$  reduction. The synthesis and characterization of other ligand scaffolds based on tetradentate bis(carbene) macrocycles and porphyrinoids is discussed, with alterations to the parent framework aimed at increasing solubility and stability during metal complexation. Also reported are efforts tailored towards the synthesis of ligands based on a bipyridine central donor with flanking phosphine chalcogenides. The phosphine oxide generated iron, nickel and rhenium complexes while the phosphine sulfide analog proved to be a surprisingly incompetent ligand.

## **Acknowledgements**

I am very grateful towards Professor Roland Roesler, who has guided me throughout both my BSc honors and graduate degree. He has promoted a curiosity and passion for science that has become an integral part of my daily life and his mentorship over the last few years is invaluable. I would also like to thank Prof. Warren Piers for instilling a genuine interest towards olefin polymerization and providing feedback and direction during synthetic meetings alongside Prof. Gregory Welch. Likewise, I would like to thank Prof. Todd Sutherland and Prof. Jeffrey Van Humbeck for their feedback and commitments towards my annual meetings and as a late addition to my committee, in addition to Prof. Michele Dolgos as my internal/external examiner.

I want to thank the Roesler group members during my tenure as a grad student, Dr. Chris Gendy, Braulio Puerta Lombardi, Alexander Harrison, Yanmin Jiang and Devon Louwe, as well as Zachary Dubrawski and Dr. Janina Willkommen for an amazing working environment and friendships that I count on lasting for many years to come.

To my best friend and love of my life, I want to thank my wife Kristina Heidebrecht for her constant support. I can honestly say that I wouldn't be half the man I am today without her amazing personality by my side. I also wouldn't be here without the loving support of my parents, in which words cannot express the gratitude I have towards my family

Most of all, I give praise to God, for nothing would be possible if not for his grace.

## Table of Contents

Preface .....	ii
Abstract .....	iii
Acknowledgements .....	iv
Table of Contents .....	v
List of Figures .....	vii
List of Tables.....	x
List of Schemes .....	xi
List of Symbols, Abbreviations and Nomenclature .....	xii
 CHAPTER 1 – INTRODUCTION TO REDOX FLOW BATTERIES.....	1
1.1 Intermittency of Renewable Energy .....	1
1.2 Redox Flow Batteries.....	2
1.3 Organic-based Electrolytes and Redox-active Ligands .....	8
1.4 Original work.....	12
 CHAPTER 2 – IRON-BASED REDOX-FLOW BATTERIES .....	14
2.1 Introduction .....	14
2.2 All-iron, all-soluble aqueous RFB .....	15
2.3 Redox Active Ligands for Application in Symmetric RFBs.....	18
2.4 Conclusion.....	27
2.5 Experimental.....	27
 CHAPTER 3 – INTRODUCTION TO THE ELECTROCHEMICAL REDUCTION OF CARBON DIOXIDE .....	34
3.1 Background Information .....	34
3.2 Homogeneous Catalysis for the Electrochemical Reduction of CO <sub>2</sub> .....	36
3.3 Mechanistic Insight and Ligand Design Considerations .....	38
3.4 Conclusion.....	41
 CHAPTER 4 – LIGAND-CENTERED ELECTROCHEMICAL CO <sub>2</sub> REDUCTION WITH A NICKEL BIS(TRIAZAPENTADIENYL) COMPLEX <sup>[144]</sup> .....	43
4.1 Author Contributions .....	43
4.2 Background Information .....	43
4.3 Synthesis and Electrochemical Analysis of Ni(TAPPy) <sub>2</sub> .....	45
4.4 Infrared Spectroelectrochemistry (IR-SEC) .....	48
4.5 Ligand Modification and Reaction with CO <sub>2</sub> .....	51
4.6 Iron-based TAPPy complexes .....	55
4.7 Experimental.....	61
 CHAPTER 5 – BIS(N-HETEROCYCLIC CARBENE) MACROCYCLES AND PORPHYRINIDS .....	66
5.1 Background Information .....	66
5.2 Unconjugated Macrocyclic Biscarbene ligands.....	68

5.3 Unsaturated Carbene-porphyrinoids .....	72
5.4 Experimental.....	75
CHAPTER 6 – CONCLUSIONS AND FINAL THOUGHTS.....	81
CHAPTER 7 – FUTURE DIRECTIONS.....	84
7.1 Background Information .....	84
7.2 Bipyridine-Based Phosphine Chalcogenides with Iron and Nickel.....	85
7.3 Bimetallic Rhenium Complexes .....	88
7.4 Experimental.....	91
References .....	96
Permissions .....	105

## List of Figures

<b>Figure 1-1</b> Wind energy supplied during daily peak demand in Germany over a year, as a percentage proportion of the total energy consumption at that time. Reproduced with permission from reference 6.....	1
<b>Figure 1-2</b> Energy storage applications based on power output and amount of energy stored (Abbreviations: Supercharged magnetic energy storage (SMES) and compressed air energy storage (CAES)). Reproduced with permission from reference 10. ....	2
<b>Figure 1-3</b> Schematic of an all-soluble RFB (top) and a mixed RFB (bottom). Reproduced from reference 15. ....	4
<b>Figure 1-4</b> Distribution of costs for a 4 MWh all-vanadium RFB <sup>[14,42]</sup> .....	7
<b>Figure 1-5</b> Selected organic materials and their corresponding reduction potentials in reference to Ag/AgCl.....	9
<b>Figure 1-6</b> Cyclic voltammogram of 0.4M [Fe(TEOA)OH] <sup>-2-</sup> and 0.4M Fe(CN) <sub>6</sub> <sup>3-/4-</sup> in a 3M sodium hydroxide solution. Reproduced with permission from reference 31. ....	11
<b>Figure 2-1</b> Solid-state structures of pseudo-octahedral complexes <b>2.2</b> (left) and <b>2.3</b> (right). The thermal ellipsoids are drawn at 50% probability. Selected bond lengths (Å) and angles (deg) for complex <b>2.3</b> : Co1–N3 = 1.861(2), Co1– N1 = 1.936(2), Co1–N5 = 1.937(2), N3–C7 = 1.330(4), N3–C11 = 1.343(4), N1– C6 = 1.312(4), N2–C6 = 1.331(4), N5–C12 = 1.311(4), N4–C12 = 1.330(4); N1–Co1– N5 = 163.68(9), N3–Co1–N30 = 178.96(15).....	17
<b>Figure 2-2</b> CVs of 1mmol solutions of complex <b>2.2</b> (left) and Fe(bpy) <sub>3</sub> SO <sub>4</sub> (right) at 0.1V s <sup>-1</sup> under argon. Conditions: 0.1 M Na <sub>2</sub> SO <sub>4</sub> , H <sub>2</sub> O, glassy carbon disk working electrode, Pt wire counter electrode, saturated Ag/AgCl reference electrode.....	17
<b>Figure 2-3</b> Solid state structure of the cationic complex [ <b>2.4</b> ] <sup>2+</sup> at 50% probability ellipsoids.....	20
<b>Figure 2-4</b> CV of a 1mmol solution of complex <b>2.4</b> at 0.1V s <sup>-1</sup> under argon. Conditions: 0.1 M TBAPF <sub>6</sub> , acetonitrile, glassy carbon disk working electrode, Pt wire counter-electrode, Ag/AgCl pseudo-reference electrode and internally referenced to ferrocene. ....	20
<b>Figure 2-5</b> CV of a 1mmol solution of complex [ <b>2.4</b> ]SO <sub>4</sub> at 0.1V s <sup>-1</sup> under argon. Conditions: 0.01 M HCl, water, glassy carbon disk working electrode, Pt wire counter electrode, saturated Ag/AgCl reference electrode.....	22



<b>Figure 2-6</b> CV of a 1mmol solution of complex <b>2.6</b> at 0.1 V s <sup>-1</sup> under argon. Conditions: 0.1 M TBAPF <sub>6</sub> , acetonitrile, glassy carbon disk working electrode, Pt wire counter electrode, Ag/AgCl pseudo-reference electrode and internally referenced to ferrocene. ....	24
<b>Figure 2-7</b> Solid-state structure of pseudo-octahedral complex <b>2.7</b> in a combination of thermal ellipsoids at 50% probability and wireframe. ....	26
<b>Figure 3-1</b> Tafel plots of selected catalysts for the electrochemical reduction of CO <sub>2</sub> to CO. (Abbreviations: iron tetraphenylporphyrin (TPPFe), <i>o,o'</i> -phenolic-TPPFe (CAT), bis( <i>o,o'</i> -phenolic)bis(pentafluorophenyl)-TPPFe (FCAT), <i>p</i> -trimethylammonium-TPPFe (WSCAT). Reproduced with permission from reference 118. ....	37
<b>Figure 3-2</b> Mechanism of CO <sub>2</sub> reduction with selected manganese catalysts .....	38
<b>Figure 3-3</b> Selected complexes with common ligand platforms electrocatalytic reduction of CO <sub>2</sub> <sup>[103,141–143]</sup> .....	42
<b>Figure 4-1</b> Structural comparison of Ni(TAPPy) <sub>2</sub> with nickel complexes <b>A–E</b> capable of catalyzing the electrochemical reduction of CO <sub>2</sub> . Below each structure are the major products formed during electrochemical reduction. ....	45
<b>Figure 4-2</b> Top: CV of Ni(TAPPy) <sub>2</sub> (0.50 mM) at 0.1 V s <sup>-1</sup> under Ar, with cathodic peak current ( <i>i</i> <sub>pc</sub> ) versus the square root of scan rate for the one-electron reduction of Ni(TAPPy) <sub>2</sub> under Ar (inset). Bottom: CVs of Ni(TAPPy) <sub>2</sub> (0.50 mM, three consecutive scans) at 0.1 V s <sup>-1</sup> under Ar (black) and CO <sub>2</sub> (red). Conditions: 0.1 M <sup>n</sup> Bu <sub>4</sub> NPF <sub>6</sub> , DMF, glassy carbon disk working electrode, Pt wire counter electrode, Ag/AgCl reference electrode. Background scans shown in grey. ....	46
<b>Figure 4-3</b> IR-SEC spectra of Ni(TAPPy) <sub>2</sub> (0.5 mM). Top: Electrolysis from -2.10 to -2.45 V in 0.05 V increments under CO <sub>2</sub> . Bottom: Electrolysis of Ni(TAPPy) <sub>2</sub> at -2.45 V under <sup>12</sup> CO <sub>2</sub> (red) and <sup>13</sup> CO <sub>2</sub> (blue). Conditions: 0.2 M <sup>n</sup> Bu <sub>4</sub> NPF <sub>6</sub> , DMF...49	49
<b>Figure 4-4</b> IR-SEC spectra of Ni(TAPPy) <sub>2</sub> (0.5 mM) at -2.45 V with (blue) and without (red) the addition of 2.5 mM [Ni(TMC)] <sup>2+</sup> under CO <sub>2</sub> . The green trace corresponds to the IR-SEC spectra of [Ni(TMC)] <sup>2+</sup> at -2.45 V in a CO saturated solution. Conditions: 0.2 M <sup>n</sup> Bu <sub>4</sub> NPF <sub>6</sub> , DMF. ....	51
<b>Figure 4-5</b> <sup>1</sup> H NMR spectra for KTAPPy in THF-d <sup>8</sup> (top) and the reaction mixture between KTAPPy and CO <sub>2</sub> (bottom). ....	53
<b>Figure 4-6</b> Solid-state structure of TAPPy-Br with 50% probability ellipsoids. ....	54
<b>Figure 4-7</b> Solid state structures of Fe(TAPPy) <sub>3</sub> from reactions using an iron(III) source (left, Monoclinic C) and an iron (II) source (right, Triclinic) shown with 50% probability ellipsoids. <sup>[175]</sup> .....	57

<b>Figure 4-8</b> Cyclic voltammogram of potential $\text{Fe}(\text{TAPPy})_2(\text{CO})_2$ (1.0 mM) at $0.1 \text{ V s}^{-1}$ under Ar (black), $\text{CO}_2$ (Dashed line) and Ar after exposure to $\text{CO}_2$ (grey) . Conditions: $0.1 \text{ M } ^n\text{Bu}_4\text{NPF}_6$ , DMF, glassy carbon disk working electrode, Pt wire counter electrode, Ag/AgCl reference electrode. ....	58
<b>Figure 4-9</b> Cyclic voltammogram of HTAPPy (1.0 mM) at $0.1 \text{ V s}^{-1}$ under Ar. Conditions: $0.1 \text{ M } ^n\text{Bu}_4\text{NPF}_6$ , DMF, glassy carbon disk working electrode, Pt wire counter electrode, Ag/AgCl reference electrode. ....	59
<b>Figure 4-10</b> Cyclic voltammogram of $\text{Fe}(\text{TAPPy})_3$ (1.0 mM) at $0.1 \text{ V s}^{-1}$ under Ar (black) and $\text{CO}_2$ (Dashed line). Conditions: $0.1 \text{ M } ^n\text{Bu}_4\text{NPF}_6$ , DMF, glassy carbon disk working electrode, Pt wire counter electrode, Ag/AgCl reference electrode. Background scan shown in grey. ....	60
<b>Figure 5-1</b> Selected carbene-based catalysts for the electrochemical reduction of $\text{CO}_2$ ..	67
<b>Figure 7-1</b> Selected catalysts for electrochemical $\text{CO}_2$ reduction based on 2,2'-bipyridine ligand frameworks.....	85
<b>Figure 7-2</b> Solid state structures of complex <b>7.4</b> (left) and <b>7.5</b> (right) drawn at 50% probability ellipsoids and wireframe.....	87
<b>Figure 7-3</b> Solid state structures of homotrimetallic rhenium complex (left) and complex <b>7.6</b> (right) drawn at 50% probability ellipsoids and wireframe. ....	88
<b>Figure 7-4</b> Cyclic voltammogram of complex <b>7.6</b> (1.0 mM) at $0.1 \text{ V s}^{-1}$ under Ar (black) and $\text{CO}_2$ (Dashed line) with the background scans shown in grey. Conditions: $0.1 \text{ M } ^n\text{Bu}_4\text{NPF}_6$ , DMF, glassy carbon disk working electrode, Pt wire counter electrode, Ag/AgCl reference electrode and internally referenced to ferrocene.....	90

## List of Tables

<b>Table 1-1</b> Half reactions, open cell voltage and electrolyte of selected RFBs	5
<b>Table 3-1</b> Standard Reduction Potentials in aqueous solutions for selected CO <sub>2</sub> reduction pathways (Referenced to SHE)	35
<b>Table 4-1</b> Controlled potential electrolysis (CPE) data <sup>a</sup>	48

## List of Schemes

<b>Scheme 2-1</b> Synthesis of ligand 2.1 and the corresponding iron complex 2.2.....	15
<b>Scheme 2-2</b> Synthesis of cobalt complex 2.3 .....	16
<b>Scheme 2-3</b> Synthesis of 1,10-phenanthroline-5,6-dione and its iron complexes.....	19
<b>Scheme 2-4</b> Synthesis of the iron coordination homoleptic complex 2.6. ....	23
<b>Scheme 2-5</b> Synthesis of the homoleptic iron complex 2.7 .....	26
<b>Scheme 4-1</b> Synthesis of KTAPPy·THF and Ni(TAPPy) <sub>2</sub> . ....	46
<b>Scheme 4-2</b> Potential reactivity of dissociated ligand with carbon dioxide to form carbonate-containing products.....	52
<b>Scheme 4-3</b> Synthesis of TAPPy-Br .....	54
<b>Scheme 4-4</b> Attempted synthesis of Synthesis of Fe <sup>II</sup> (TAPPy) <sub>2</sub> L <sub>2</sub> .....	56
<b>Scheme 4-5</b> Synthesis of Fe(TAPPy) <sub>3</sub> .....	59
<b>Scheme 5-1</b> Proposed catalyst platforms (right) based on known catalysts incorporating porphyrin and pyridine-based macrocycles (left) .....	68
<b>Scheme 5-2</b> Synthetic pathway for proligand 5.1 .....	70
<b>Scheme 5-3</b> Synthetic pathway for proligand 5.4.....	71
<b>Scheme 5-4</b> Selected complexation attempts with proligand 5.4 .....	72
<b>Scheme 5-5</b> Proposed synthetic pathway for a meso-substituted carbene porphyrinoid. ....	74
<b>Scheme 7-1</b> Synthesis of free phosphine 7.1 .....	85
<b>Scheme 7-2</b> Synthesis of oxidized phosphines 7.2 and 7.3.....	86
<b>Scheme 7-3</b> Synthesis of coordination complexes 7.4 and 7.5.....	87
<b>Scheme 7-4</b> Potential proligands and ligands based on a pentadentate N5 complex used for electrochemical CO <sub>2</sub> reduction <sup>[231]</sup> .....	91

## List of Symbols, Abbreviations and Nomenclature

Symbol	Definition
Å	angstrom (unit), $10^{-10}$ m
AI-EES	Alberta Innovates Energy and Environmental Solutions
Ar	aryl
atm	atmosphere (unit)
ATR	attenuated total reflectance
Bpy	2,2'-bipyridine
<sup>n</sup> Bu	butyl (normal)
<sup>t</sup> Bu	tertiary-butyl
°C	degree Celsius (centigrade) (unit)
CAES	compressed air energy storage
CFREF	Canada First Research Excellence Fund
CPE	controlled potential electrolysis
CV	cyclic voltammogram
d <sub>n</sub>	deuterated isotopologue, where n = number of deuterium atoms
DDQ	2,3-dichloro-5,6-dicyano-1,4-benzoquinone
Dipp	2,6-diisopropylphenyl
DCM	dichloromethane
DFT	density functional theory
DMF	<i>N,N</i> -dimethylformamide
DMSO	dimethylsulfoxide
e <sup>-</sup>	electron
ESI	electro-spray ionization
Fc	ferrocene
GC	gas chromatography
HRMS	high resolution mass spectrometry
i <sub>pc</sub>	cathodic peak current
IR	infrared
KHMDS	potassium hexamethyldisilazide
L	ligand
M	molar (unit)
M	metal
min	minutes
<i>m/z</i>	mass to charge ratio
NASA	National Aeronautics and Space Administration
NHC	N-heterocyclic carbene
NHE	normal hydrogen electrode
NMR	nuclear magnetic resonance

o	ortho
OAc	acetate
p	para
PCET	proton coupled electron transfer
ppm	parts per million
py	pyridine
R	generic hydrocarbon group
RFB	redox-flow battery
SEC	spectroelectrochemistry
SHE	standard hydrogen electrode
SMES	supercharged magnetic energy storage
TAPPy	1,3,5-triazapentadienyl-2,4-bis(2-pyridyl)
TBAPF <sub>6</sub>	tetra-n-butylammonium hexafluorophosphate
TEMPO	(2,2,6,6-Tetramethylpiperidin-1-yl)oxyl
terpy	2,2':6',6''-terpyridine
TMC	1,4,8,11-tetramethyl-1,4,8,11-tetraazacyclotetradecane
TOF	turnover frequency
tol	toluene
TEOA	triethanolamine
THF	tetrahydrofuran
δ	chemical shift in ppm

## Chapter 1 – Introduction to Redox Flow Batteries

### 1.1 Intermittency of Renewable Energy

The renewable energy provided by wind and solar radiation provides ideal means to decrease CO<sub>2</sub> emissions, yet it is also notorious for intermittent availability, frequently and reliably leading to situations where there is a mismatch between energy supply and demand.<sup>[5]</sup> Increasing the proportion of wind and solar energy in the electricity network further exacerbates these issues, leading to the need for a load-leveling method that needs to be reliable, responsive, inexpensive, and capable of handling huge loads. **Figure 1.1** shows the wind energy supplied during daily peak demand in Germany over a year, as a percentage proportion of the total energy consumption at that time.<sup>[6]</sup>

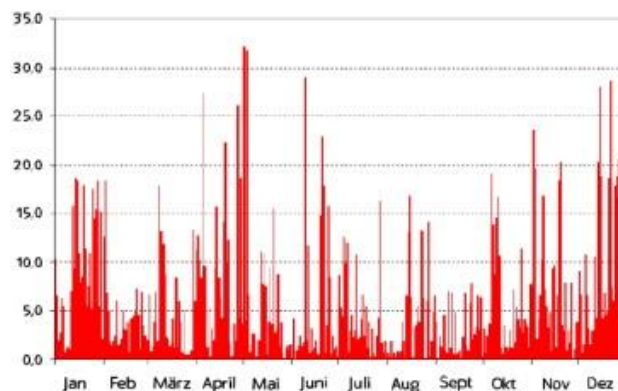


**Figure 1-1** Wind energy supplied during daily peak demand in Germany over a year, as a percentage proportion of the total energy consumption at that time. Reproduced with permission from reference 6.

These reliable discrepancies between supply and demand result in the destabilization of electrical grids when over 20% of wind and solar energy is incorporated in the energy generation capacity.<sup>[7,8]</sup> However, estimations from Bloomberg New Energy Finance propose that renewables could supply up to 50% of the world's electricity by 2050.<sup>[9]</sup> This estimation takes into account an expected decrease in the costs of energy

storage, as energy storage can alleviate these intermittencies at the grid level. Current methods of grid energy storage utilize gravitational or kinetic energy as well as pressure, in form of pumped hydro, flywheels, and compressed air, but such facilities can be geographically or geologically limited and have their intrinsic drawbacks (*vide infra*).<sup>[5,10]</sup> Other alternatives include the use of large-scale batteries or storing the excess energy in the form of chemical bonds, *i.e.* fuels

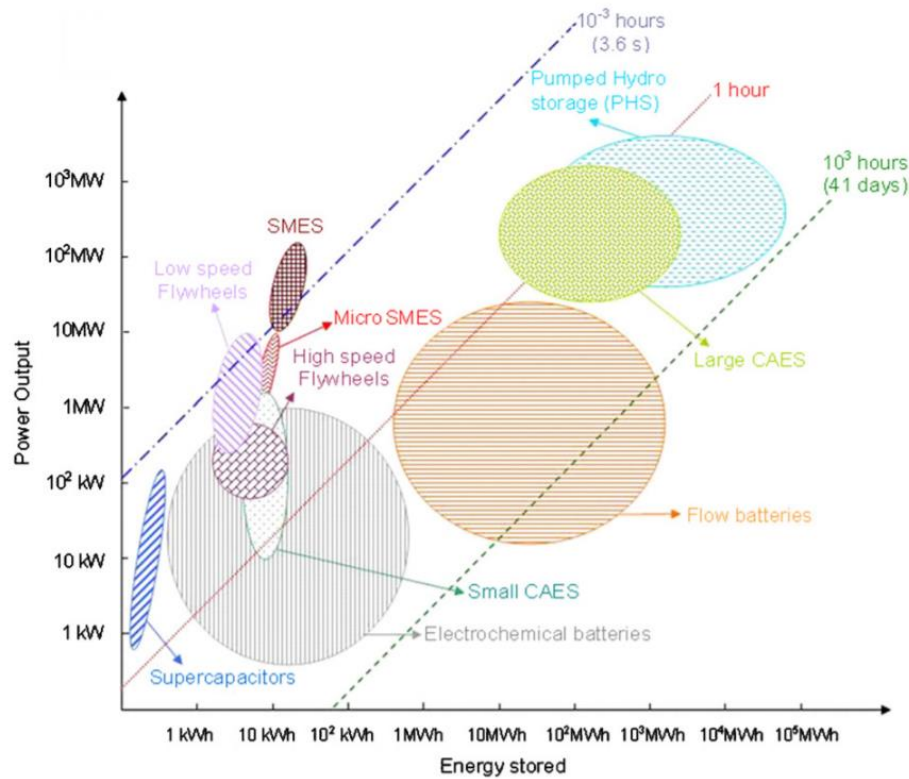


**Figure 1-2** Energy storage applications based on power output and amount of energy stored (Abbreviations: Supercharged magnetic energy storage (SMES) and compressed air energy storage (CAES)). Reproduced with permission from reference 10.

## 1.2 Redox Flow Batteries

The use of grid energy storage for charging/discharging applications requires installments that are capable of storing large amounts of electricity. Different energy storage methods are ranked in **Figure 1.2** based on power output and the amount of energy



stored.<sup>[10]</sup> Moving towards the top right of the graph leads to more promising grid energy storage opportunities by being able to provide a large amount of power for a prolonged period of time.

Currently “pumped hydro” represents over 95% of the global grid storage capacity as it is relatively inexpensive, maintains a long calendar life and can store large amounts of energy with high discharge rates.<sup>[11]</sup> Pumped hydro has been used to increase the compatibility between the constant energy output of nuclear power plants and the variable energy demand of the electrical grid. However, geographical restrictions and environmental impact limit the feasibility of this method in numerous circumstances. Compressed air energy storage (CAES) typically utilizes large underground caverns for energy storage, yet this option is restricted by geology.<sup>[11]</sup> A promising alternative is the use of large-scale batteries that could be implemented without major geographical restrictions. Globally, 5.5 GW of battery storage has been installed, with decreased prices leading to increased utilization over the last couple of years.<sup>[12]</sup> For batteries to be applicable to grid storage of renewable energy, they need to be compatible with a large number of charge/discharge cycles, have quick response rates, as well as reasonable capital costs.<sup>[13]</sup> Redox-flow batteries (RFBs) represent a promising alternative to conventional electrochemical systems such as lithium-ion and lead-acid batteries. This is because RFBs store the energy in liquid electrolytes and hence they are not subjected to the intrinsic solid-electrolyte degradation processes that limit the life of conventional batteries.<sup>[14]</sup> A representation of a classic, all-soluble (top) and a mixed (bottom) redox flow battery is shown in **Figure 1.3**.<sup>[15]</sup>

An all-soluble RFB stores the active species in external reservoirs and pumps it through the cell, enabling the power (W) and storage capacity ( $\text{Wh}^{-1}$ ) to be modified separately while maintaining capacity for over 20,000 cycles in certain designs. The power of the system is determined by the design of the battery stack, and can be tuned by changing the open cell voltage through electrolyte design, size of the electrodes (current collectors)

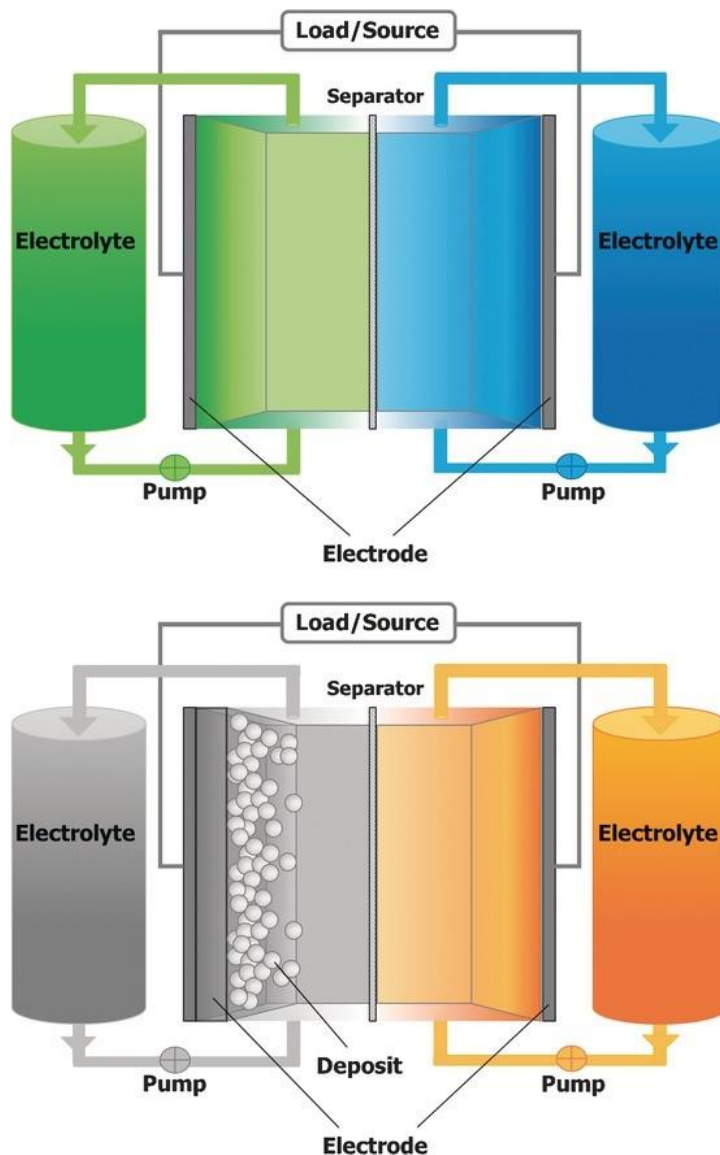


**Figure 1-3** Schematic of an all-soluble RFB (top) and a mixed RFB (bottom). Reproduced from reference 15.

and the number of cells in a stack. The energy storage capacity can also be modified by simply increasing the volume of the external electrolyte tanks, as well as by changing the concentration of redox-active species in solution.<sup>[7]</sup> The development of modern redox flow batteries was pioneered by NASA in the 1970s, with a system featuring the  $\text{Fe}^{3+}/\text{Fe}^{2+}$  redox couple for the anolyte solution and the  $\text{Cr}^{3+}/\text{Cr}^{2+}$  redox couple for the catholyte, as well as a hydrochloric acid – based supporting electrolyte.<sup>[7,16,17]</sup> The battery provided an open circuit voltage of 1.2V. This seminal work was followed a decade later by the all-vanadium redox flow battery, which has been extensively investigated since its discovery in 1986 and remains the most successful platform to date.<sup>[18–20]</sup>

**Table 1-1** Half reactions, open cell voltage and electrolyte of selected RFBs

System	Half Reactions	Cell Voltage	Electrolyte (Anode/Cathode)
All-Soluble			
All-Vanadium	Anode: $\text{V}^{2+} \xleftarrow{\text{charge}} \xrightarrow{\text{discharge}} \text{V}^{3+} + \text{e}^-$	1.4V	$\text{H}_2\text{SO}_4 / \text{H}_2\text{SO}_4$
	Cathode: $\text{VO}_2^+ + \text{e}^- \xleftarrow{\text{charge}} \xrightarrow{\text{discharge}} \text{VO}^{2+}$		
Vanadium-Polyhalide	Anode: $\text{V}^{2+} \xleftarrow{\text{charge}} \xrightarrow{\text{discharge}} \text{V}^{3+} + \text{e}^-$	1.3V	$\text{VCl}_3\text{-HCl} / \text{NaBr-HCl}$
	Cathode: $\frac{1}{2} \text{Br}_2 + \text{e}^- \xleftarrow{\text{charge}} \xrightarrow{\text{discharge}} \text{Br}^-$		
Bromine-Polysulfide	Anode: $2\text{S}_2^{2-} \xleftarrow{\text{charge}} \xrightarrow{\text{discharge}} \text{S}_4^{2-} + 2\text{e}^-$	1.5V	$\text{NaS}_2/\text{NaBr}$
	Cathode: $\frac{1}{2} \text{Br}_2 + \text{e}^- \xleftarrow{\text{charge}} \xrightarrow{\text{discharge}} \text{Br}^-$		
Iron-Chromium	Anode: $\text{Fe}^{2+} \xleftarrow{\text{charge}} \xrightarrow{\text{discharge}} \text{Fe}^{3+} + \text{e}^-$	1.2V	$\text{HCl}/\text{HCl}$
	Cathode: $\text{Cr}^{3+} + \text{e}^- \xleftarrow{\text{charge}} \xrightarrow{\text{discharge}} \text{Cr}^{2+}$		
Hybrid			
Zinc-Bromine	Anode: $\text{Zn} \xleftarrow{\text{charge}} \xrightarrow{\text{discharge}} \text{Zn}^{2+} + 2\text{e}^-$	1.8V	$\text{ZnBr}_2/\text{ZnBr}_2$
	Cathode: $\text{Br}_2 + 2\text{e}^- \xleftarrow{\text{charge}} \xrightarrow{\text{discharge}} 2\text{Br}^-$		
Zinc-Cerium	Anode: $\text{Zn} \xleftarrow{\text{charge}} \xrightarrow{\text{discharge}} \text{Zn}^{2+} + 2\text{e}^-$	2.4V	$\text{CH}_3\text{SO}_3\text{H}/\text{CH}_3\text{SO}_3\text{H}$
	Cathode: $2\text{Ce}^{4+} + 2\text{e}^- \xleftarrow{\text{charge}} \xrightarrow{\text{discharge}} 2\text{Ce}^{3+}$		

Both the Fe/Cr and all-vanadium RFBs have been tested in commercial applications, along with other systems such as bromine/polysulfide, vanadium/bromine

and hybrid zinc/bromide RFBs involving zinc deposition.<sup>[15,21,22]</sup> In addition to commercial applications, a multitude of metal-based systems have been explored, including Zn/Ce,<sup>[23]</sup> Zn/Ni,<sup>[24]</sup> Ru/Organic,<sup>[25,26]</sup> uranium diketonates,<sup>[27]</sup> Mn/V,<sup>[28]</sup> all-Cu,<sup>[29]</sup> all-Fe,<sup>[30,31]</sup> soluble lead-acid,<sup>[32]</sup> Ti/Fe,<sup>[33]</sup> Cu/PbO<sub>2</sub>,<sup>[34]</sup> and Li/nonmetal<sup>[35,36]</sup>. The representative half reactions, cell potentials and electrolytes of a few of the aforementioned RFBs are shown in **Table 1.1**. Intrinsic to different redox couples are the standard reduction potentials of the two active species, which determine the open circuit voltage, and the solubility, which impacts the energy density. Also essential are the redox kinetics, which can limit the current density at the electrode, and the long-term stability of the redox-active species. The electrolyte determines the conductivity of the solution, directly influencing the ohmic losses and hence the efficiency of a given RFB, and also impacts the solubility and stability of the active species. Electrolytes based on acidic solutions are generally preferred, as the inherent conductivity of the solution is much higher in water/acid (6M HCl: 0.84 ohm<sup>-1</sup>cm<sup>-1</sup>, 1M HCl: 0.33 ohm<sup>-1</sup>cm<sup>-1</sup>) compared to common organic solvents such as acetonitrile (1M TBAPF<sub>6</sub>: 0.031 ohm<sup>-1</sup>cm<sup>-1</sup>), dimethylformamide (1M TBAPF<sub>6</sub>: 0.0145 ohm<sup>-1</sup>cm<sup>-1</sup>) or tetrahydrofuran (1M TBAPF<sub>6</sub>: 0.0027 ohm<sup>-1</sup>cm<sup>-1</sup>).<sup>[37]</sup> However, aqueous solutions constrain the maximum open circuit voltage of the battery within the electrochemical solvent window of water, which is determined by the potentials for oxygen and hydrogen evolution at the anode and cathode, respectively. By comparison, organic solvents enable a larger open circuit voltage as the potential window is much larger (H<sub>2</sub>O/glassy carbon: ~2V; acetonitrile/TBAPF<sub>6</sub>: ~5.5V).<sup>[38]</sup> The relatively narrow electrochemical solvent window of water can be expanded using electrodes that inhibit the development of hydrogen and oxygen (increase the overpotential).

Some of the weaknesses associated with RFBs include low energy density, high cost of the membrane and electrolyte active species, as well as the possibility for crossover contamination. Crossover contamination is the permeation of the active species through the membrane and can lead to efficiency losses, capacity decay and deleterious side reactions, well illustrated in the case of the Fe/Cr battery.<sup>[7,39]</sup> The use of the same metal in both compartments (single-component RFB) can alleviate some of these issues. The vanadium species that crosses through the membrane in an all-vanadium RFB can be converted into the active material through reduction/oxidation and only leads to a decrease in current efficiency but not a loss in capacity.<sup>[39,40]</sup> Further improvements to the initial all-vanadium battery have been implemented, including the use of a mixed-acid electrolyte for increasing conductivity, stability and solubility of the vanadium species, as well as advancements in membrane design.<sup>[41]</sup> The all-vanadium RFB continues to have the widest utilization in grid energy storage, however, it features a substantial capital contribution

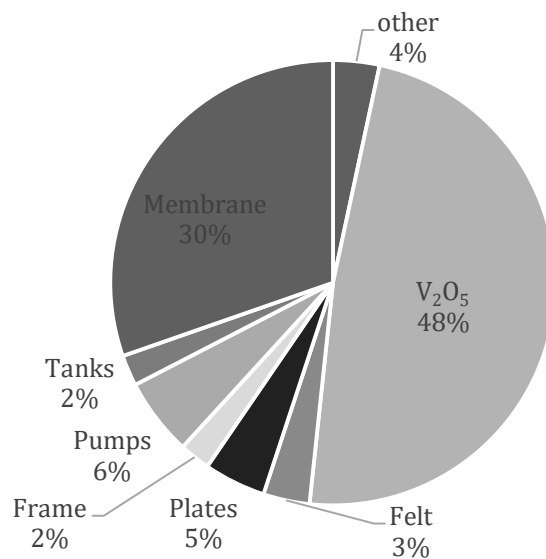


**Figure 1-4** Distribution of costs for a 4 MWh all-vanadium RFB<sup>[14,42]</sup>

from the metal source: A representative 4 MWh facility would have approximately 48% of the capital costs resulting from vanadium oxide alone with the second largest contributor being the membrane/separator.<sup>[8]</sup> The distribution of costs is shown in **Figure 1.4**.<sup>[14,42]</sup> The two main objectives for improving the economic feasibility of RFBs target reducing the cost of active species in solution through using inexpensive metals or organic-based active species, and eliminating the need for a membrane in single-electrolyte systems and hybrid RFBs.

### 1.3 Organic-based Electrolytes and Redox-active Ligands

Although transition metal based RFBs have featured substantial improvement since their discovery in the 1970s, organic (hydrocarbon-based) active species offer more flexibility for tuning both reduction potentials and solubility, while potentially lowering the cost of the active species. The use of organic redox-active species in RFBs emerged in 2009, when chloroanil was used in the catholyte solution, coupled with a cadmium anode in a mixed RFB.<sup>[43]</sup> The first asymmetric all-organic battery quickly followed in 2011, incorporating (2,2,6,6-tetramethylpiperidin-1-yl)oxyl (TEMPO) and N-methylphthalimide.<sup>[44]</sup> Systems utilizing organic components continue to be developed, with common frameworks based on quinones/anthraquinones, alkoxybenzenes, viologens and TEMPO, as shown in **Figure 1.5** together with their representative reduction potentials. Polymeric organic compounds have also been used to circumvent the diffusion through the membrane while maintaining activity as a charge carrier.<sup>[43,45–52]</sup>

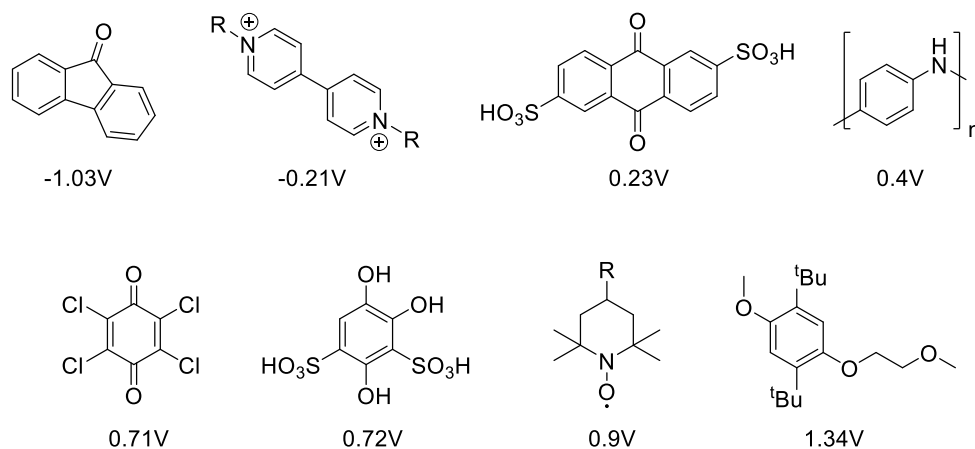


**Figure 1-5** Selected organic materials and their corresponding reduction potentials in reference to Ag/AgCl

However, even with the development of organic-based active species and continued research into inorganic RFBs, no economically viable RFB for large-scale energy storage is currently available. New electrolytes are needed in order to compete with conventional electrochemical batteries (mostly lithium-ion) and other large-scale storage options. Ligand design can play an important role in the future for RFBs: the reduction potential, electrode kinetics, solubility and stability of inorganic redox couples can be balanced with appropriate structural motifs. The reduction potential of a  $M^{n+1}/M^n$  system can be then modified with the appropriate choice of ligands, where the use of strong  $\sigma/\pi$  donors increases the electron density at the metal center, resulting in an increased stability of higher oxidation states. In addition, ligands that are able to accept electron density can stabilize lower oxidation states, allowing for tuning towards both cathodic and anodic potentials through ligand design. This has been exemplified in aqueous solutions with inexpensive metals such as iron, where the conventional  $Fe^{3+}/Fe^{2+}$  redox couple is at 0.77V as a solvated ion in aqueous solution. Commercially available ligand-precursors can tune the reduction potential of the  $Fe^{2+}/Fe^{3+}$  redox couple, exploiting the available solvent window

of water. For example, triethanolamine (TEOA) induces a cathodic shift to -0.859V vs. SHE at pH 13, and tripyridyltriazine leads to an anodic shift to 1.484V vs. SHE at pH 0.<sup>[31]</sup> The pH of the electrolyte can also be used to shift the redox window of water in order to best suit the electrochemical demands of a given redox system.

The incorporation of appropriate ligands in redox flow batteries enables the use of inexpensive transition metals that would be ill-suited for such applications in their aquated form,  $M(OH_2)_6^n/M(OH_2)_6^{n+1}$ , because of the poor compatibility of their redox potentials with the redox window of water. Additional parameters towards ligand design need to be considered: minimal reorganization energy between oxidation states is needed to maintain fast response rates; the ligand framework needs to form stable complexes across both oxidation states to prevent demetallation or ligand dissociation/association reactions interfering with the electrochemical process; the solubility of the complex in solution needs to be addressed.<sup>[53]</sup> Additionally, the use of redox-active ligands provides an avenue towards single-active-component redox-flow batteries based on metal complexes. This area is relatively scarcely represented in the academic literature and provides modular access to a wide range of properties.<sup>[54–62]</sup>

Because of problems associated with membrane-crossover contamination, using the same electrochemically active component in both the anolyte and catholyte continues to be pursued, with the most notable example being the all-vanadium system. This eliminates capacity loss due to crossover. In addition to the all-vanadium system, there are all-copper,<sup>[29,63,64]</sup> all-iron,<sup>[31,65–67]</sup> all-lead<sup>[68]</sup> and all-chromium RFBs.<sup>[69]</sup> However, the majority of new RFBs using only one electrochemically active component involve deposition of a metallic plate. These are mixed systems that store energy in a solid medium



and effectively negate many of the advantages of RFBs. They are susceptible to dendrite formation and no longer allow for energy and power to be modified separately.<sup>[70]</sup> The all-iron mixed redox flow battery is of specific interest due to low cost and reduced toxicity of the redox active species, but due to the  $\text{Fe}^{2+/0}$  reduction potential at -0.44V vs. SHE, a relatively high amount of hydrogen can be produced while charging.<sup>[70,71]</sup> The pH of the system can be increased in order to minimize hydrogen production, yet this can lead to other deleterious effects, such as the precipitation of iron hydroxide. The use of coordination complexes has emerged as a solution in all-iron RFBs, stabilizing iron under basic conditions or tuning the reduction potential of the  $\text{Fe}^{2+/3+}$  redox couple.<sup>[59,72–76]</sup> Only one all-soluble, all-iron redox flow battery has been reported to date, using an iron tetraethanolamine /iron cyanide redox pair.<sup>[31]</sup> The corresponding cyclic voltammograms (CV) of the active species with their reduction potentials for this asymmetric system are shown in **Figure 1.6**.

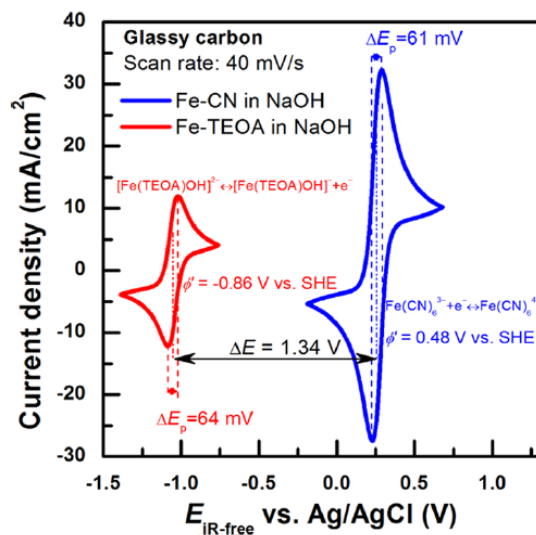


**Figure 1-6** Cyclic voltammogram of 0.4M  $[\text{Fe}(\text{TEOA})\text{OH}]^{-2-}$  and 0.4M  $\text{Fe}(\text{CN})_6^{3-/4-}$  in a 3M sodium hydroxide solution. Reproduced with permission from reference 31.

Although a voltage difference of 1.34 V was obtained, issues with current efficiency and resistance were observed. The crossover of triethanolamine, which can be oxidized under the utilized potentials, through the membrane was identified as a problem. The use of triethanolamine in the  $\text{Fe}(\text{CN})_6^{2-/3-}$  solution also led to changes in the electrochemical behavior, suggestive of a potential reaction of TEOA with  $\text{Fe}(\text{CN})_6^{3-}$ . Because of the incompatibility of the active species, new design principles need to be pursued in order to afford a stable all-iron, all-aqueous redox flow battery.

In addition to using the same electrochemically active component, the use of redox active ligands emerged as a desirable solution in symmetric redox flow batteries.<sup>[56–60,62]</sup> The design of the ligand has led to enhanced solubility, redox activity and improved stability of the overall system through functionalization, chelation and derivatization. Symmetric redox flow batteries reduce the issues associated with crossover of the active species in solution and eliminate the need for mixed-reactant electrolytes.<sup>[77–79]</sup> Only a few symmetric redox flow batteries have been reported, and they use either organic active species,<sup>[79–82]</sup> or metal coordination complexes incorporating redox-active ligands.<sup>[57–60,69,83]</sup> Other complexes incorporating redox-active ligands have been used for asymmetric redox flow batteries. The majority of these systems use electrolytes based on organic solvents in order to afford a greater open circuit voltage and enhanced solubility of the complexes, leading to increased energy density compared to aqueous solutions, but also higher internal resistance.

#### **1.4 Original work**

The original work reported herein was carried out within the framework of an AI-EES (Alberta Innovates – Energy and Environment Solutions) funded project (with Drs.

Birss and Roberts) aimed at exploring redox flow systems with high practical applicability potential in grid-storage devices. The project targeted primarily all-vanadium systems and also explored other options, which constituted the work described in the next chapter. The requirements of the targeted systems were:

1. Simplicity and low cost for large-scale applicability in grid-storage devices.
2. Water-based electrolytes for reduced ohmic losses and decreased environmental impact.
3. High concentration of active species ( $> 1\text{M}$ ) for acceptable energy density.
4. High stability.
5. Fast electrode kinetics for high current density

The identification of a single-component system to be tested in membrane-less systems targeted by the Roberts group would have been a bonus. Considering these factors, the synthesis and characterization of metal-coordination complexes suitable as potential charge carriers in RFBs will be described. Following initial testing of manganese, chromium, cobalt and iron systems, only the latter have been pursued.

## Chapter 2 – Iron-based Redox-Flow Batteries

### 2.1 Introduction

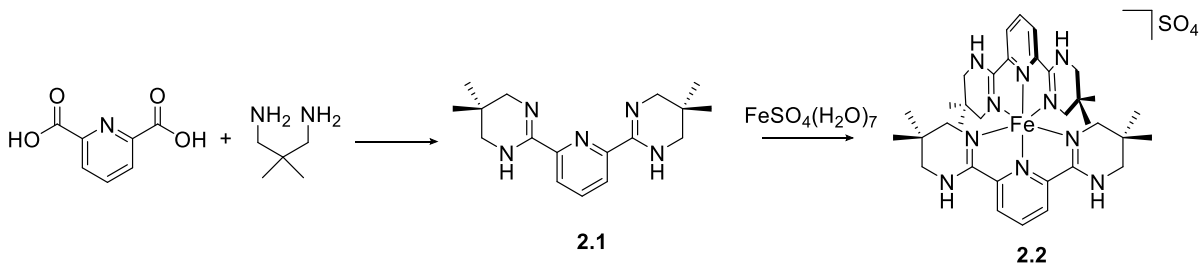
Initial work targeted an all-iron, all-soluble aqueous redox flow battery using ligand design to tune the  $\text{Fe}^{2+/3+}$  redox couple. 2,2'-bipyridine (bpy) complexes continue to be investigated as charge carriers in RFBs as cost effective, electrochemically reversible and stable systems.<sup>[25,57,84,85]</sup> With commercial availability and stability under a wide range of conditions, the tris(2,2'-bipyridine)iron complex was identified as a potential charge carrier in the catholyte solution. The tris(2,2'-bipyridine)iron complex has been extensively studied, with 2,2'-bipyridine acting as an efficient  $\pi$  acceptor for shifting the  $\text{Fe}^{2+/3+}$  redox couple to more anodic potentials.<sup>[86]</sup> The resulting  $\text{Fe}^{2+/3+}$  redox couple appears at 1.04V vs. SHE with reversible electrochemistry, moderate solubility and stability in a variety of solvents.<sup>[85,87]</sup> Tris(2,2'-bipyridine)iron sulfate was synthesized by simply mixing hydrated iron sulfate and commercial 2,2'-bipyridine in methanol overnight, leading to near-quantitative yields after removing volatiles in vacuo. The sulfate salt was preferred over halides, which had been shown to be capable of exchange with 2,2'-bipyridine.<sup>[87]</sup>

Suitable ligand frameworks for anolyte solution complexes usually involve hard, chelating bases such as EDTA, citrate, TEOA or other amines, in order to increase the electron density at the metal center. Chelation helps stabilizing the complexes, however, the alkoxides require a basic pH for increased stability and would not be compatible with tris(2,2'-bipyridine)iron sulfate in the catholyte. Following the remarkable success of 2,2':6',6''-terpyridine ligands (terpy) in coordination chemistry and catalysis, other symmetric, neutral NNN-pincer ligands with pyridine central moieties and unsaturated nitrogen pendant donors have been pursued. Ligand **2.1** was deemed accessible via one

straightforward synthetic step from commercially available starting materials, and the resultant complexes were expected to be soluble in both water and organic solvents. The presence of nitrogen atoms capable to form hydrogen bonds in the ligand framework of **2.1** was expected to enhance the water solubility of its complexes and to offer the possibility to act as neutral(diiminopyridine), mono- (amidoiminopyridine) or dianionic (diamidopyridine) ligand, potentially stabilizing different oxidation states.

## 2.2 All-iron, all-soluble aqueous RFB

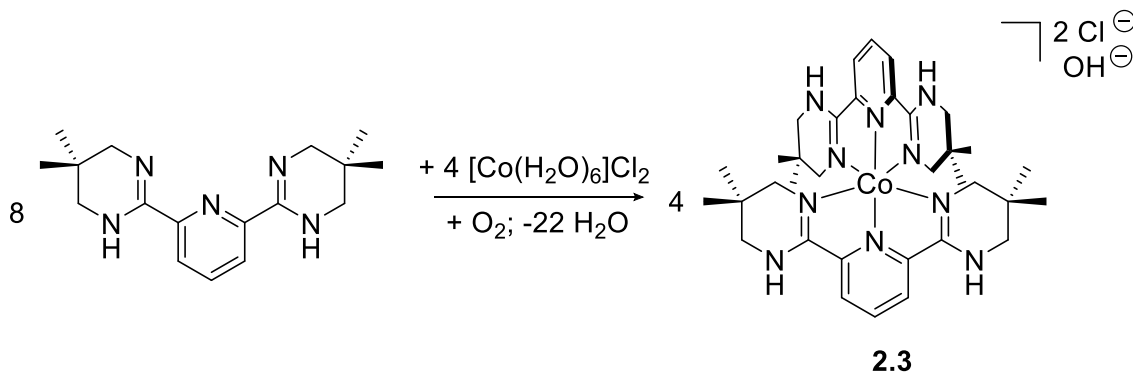
The synthesis of the NNN-pincer ligand **2.1** was carried out via a simple condensation reaction, following the modification of a procedure reported for an anionic phenylene analog (**Scheme 2.1**).<sup>[88]</sup> The product was obtained by refluxing dipicolinic acid and 2,2-dimethylpropane-1,3-diamine in ethylene glycol, with the use of p-toluenesulfonic acid as a catalyst.<sup>[89]</sup>



**Scheme 2-1** Synthesis of ligand **2.1** and the corresponding iron complex **2.2**

The corresponding iron complex **2.2** was synthesized by refluxing a methanol solution containing two equivalents of **2.1** and hydrated iron(II) sulfate overnight. Single crystals of complex **2.2** were grown by slow evaporation from a concentrated solution of **2.2** in acetonitrile; however, they were of low quality, so the resultant solid state structure revealed connectivity but could not be used for determination of bond lengths and angles. Although bond lengths and angles cannot be determined from complex **2.2**, the pseudo

octahedral structure is similar to that of the corresponding cobalt (III) complex **2.3**. This was synthesized by refluxing a methanol solution containing two equivalents of **2.1** and cobalt(II) chloride hexahydrate in air overnight (**Scheme 2.2**). Under exclusion of air, the reaction failed to produce the desired compound, confirming that atmospheric oxygen was responsible for the oxidation of Co(II) to Co(III).



**Scheme 2-2** Synthesis of cobalt complex **2.3**

Single crystals suitable for X-ray crystallography were obtained by slow evaporation of a concentrated solution of **2.3** in a methanol–toluene mixture. Two of the chloride ions are weakly hydrogen bonded to the cation ( $\text{Cl1}\cdots\text{N2} = 3.177(4) \text{ \AA}$ ) while the third bridges the cations via weak hydrogen bonds, forming a linear supramolecular arrangement ( $\text{Cl2}\cdots\text{N4} = 3.208(4) \text{ \AA}$ ). The N1–C6 and N2–C6 bonds are very similar in length ( $1.312(4)$  and  $1.331(4) \text{ \AA}$ , respectively), indicating extensive electron delocalization over the amidine fragment. Additional characterization of the cobalt complex and a visual representation of hydrogen bonding of the amidine fragment with counterions can be found in a recently published article.<sup>[89]</sup>

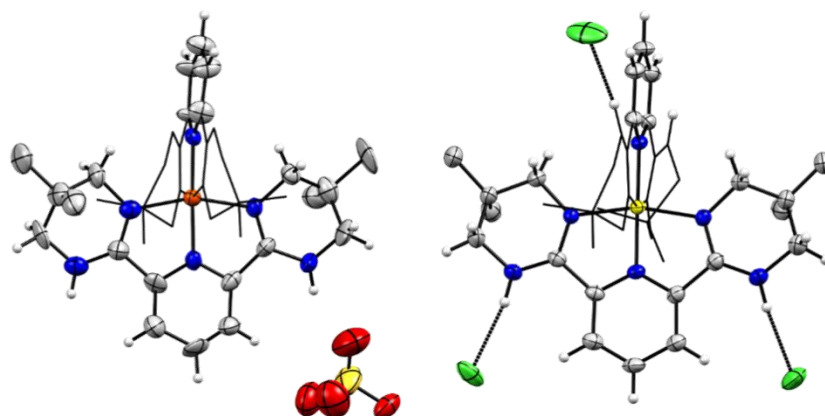


**Figure 2-1** Solid-state structures of pseudo-octahedral complexes **2.2** (left) and **2.3** (right). The thermal ellipsoids are drawn at 50% probability. Selected bond lengths (Å) and angles (deg) for complex **2.3**: Co1–N3 = 1.861(2), Co1–N1 = 1.936(2), Co1–N5 = 1.937(2), N3–C7 = 1.330(4), N3–C11 = 1.343(4), N1–C6 = 1.312(4), N2–C6 = 1.331(4), N5–C12 = 1.311(4), N4–C12 = 1.330(4); N1–Co1–N5 = 163.68(9), N3–Co1–N30 = 178.96(15).

The cyclic voltammogram of complex **2.2** in 0.1M Na<sub>2</sub>SO<sub>4</sub> solution reveals an Fe<sup>2+/3+</sup> redox couple at 0.12 V vs. SHE. The redox couple is reversible with a 62mV peak

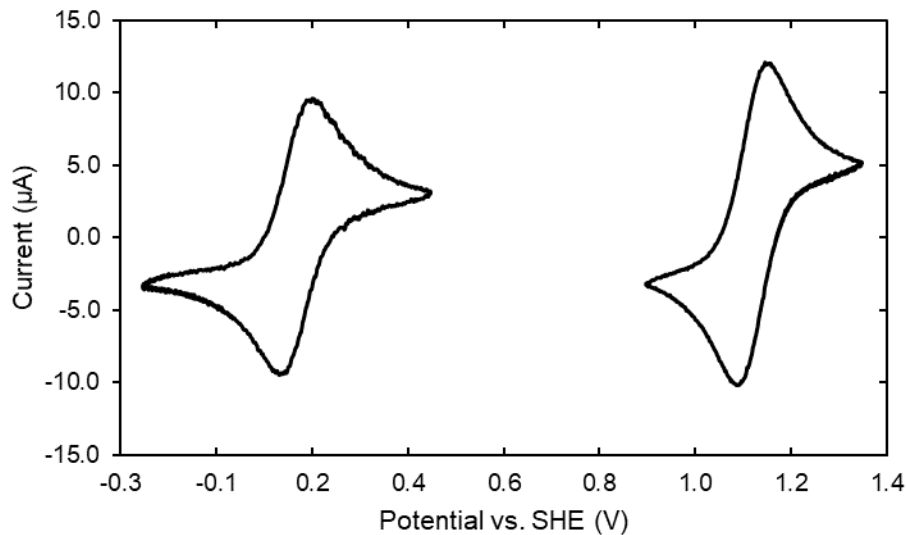


**Figure 2-2** CVs of 1mmol solutions of complex **2.2** (left) and Fe(bpy)<sub>3</sub>SO<sub>4</sub> (right) at 0.1V s<sup>-1</sup> under argon. Conditions: 0.1 M Na<sub>2</sub>SO<sub>4</sub>, H<sub>2</sub>O, glassy carbon disk working electrode, Pt wire counter electrode, saturated Ag/AgCl reference electrode.

separation and doesn't contain any other observable features within the solvent window of water. (**Figure 2.2**).

The initial targets for an all-iron redox flow battery were achieved with the current system, where the syntheses of both redox pairs are simple, high yielding and stem from commercially available reagents. When complex **2.2** is combined with  $\text{Fe}(\text{bpy})_3\text{SO}_4$ , a potential difference of 0.92V is obtained, in comparison to a 1.12 V for the mixed all-iron RFB that involves deposition of metallic iron (**Figure 2.2**). Complex **2.2** maintains stability in aqueous solution, as the cyclic voltammetry shows no changes after 6 months of storage (1mmol solution of **2.2** in 0.1M  $\text{Na}_2\text{SO}_4$ ). Both complex **2.2** and  $\text{Fe}(\text{bpy})_3\text{SO}_4$  showed reasonable electrode kinetics in the preliminary analysis (based on small peak separation in the voltammogram). The concentration of complex **2.2** in aqueous solutions was low (*ca.* 0.2M), although modification of the ligand backbone to increase solubility remains an option.

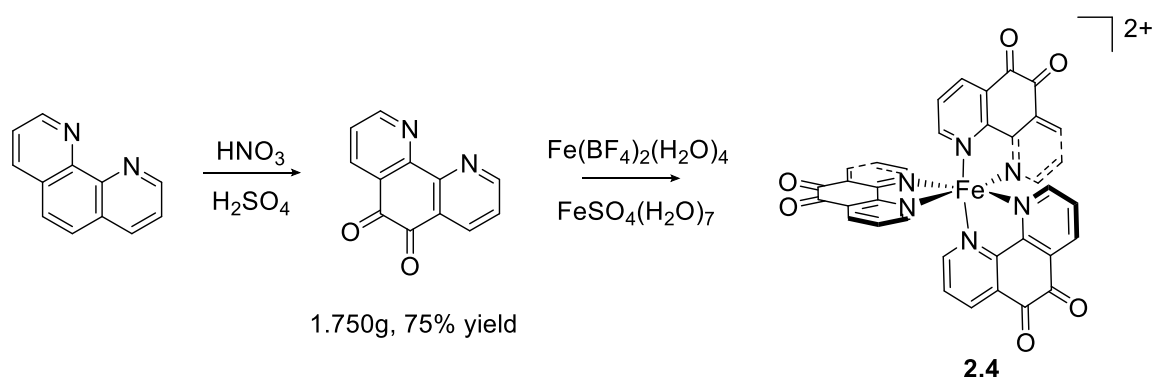
The synthesis of complex **2.2** and  $\text{Fe}(\text{bpy})_3\text{SO}_4$  was scaled up to 25 grams and provided to the Roberts group at the University of Calgary for testing within a small scale RFB. An H-cell can be used for preliminary testing of cycling efficiency and is proposed for future work.

### **2.3 Redox Active Ligands for Application in Symmetric RFBs**

Parallel to the work on the asymmetric all-iron all-aqueous redox flow battery, iron coordination complexes featuring redox active ligands for symmetric RFBs that could be used in a membrane-less RFBs were pursued. Quinone-based organic compounds have shown promising electrochemical behavior for use in organic RFBs, so ligands incorporating quinone or hydroquinone functional groups were identified.



The electrochemical behavior of 1,10-phenanthroline-5,6-dione metal complexes is relatively well understood, with a pH-dependent 2 electron reduction of the quinone to generate the corresponding catecholate.<sup>[90,91]</sup> The ligand framework is also capable of delocalizing electron density throughout the  $\pi^*$  orbital, leading to an anodic shift of metal redox potentials for coordinated complexes. The majority of electrochemical characterization of known homoleptic iron complex **2.4** involved the use of organic solvents; <sup>[92–94]</sup> we tested its suitability as electrolyte in a symmetric redox flow battery operating in acidic aqueous conditions. 1,10-phenanthroline-5,6-dione is synthesized from 1,10-phenanthroline by oxidation in a nitric acid/sulfuric acid solution. The ligand can be simply collected by filtration and did not need any additional purification before complexation with iron. The synthesis of iron complex **2.4** proceeds readily by refluxing the corresponding iron salt with the ligand in a methanol solution (**Scheme 2.3**). Single crystals suitable for X-ray diffraction were grown by layering a concentrated acetonitrile solution of **2.4**(BF<sub>4</sub>)<sub>2</sub> in benzene. The resulting homoleptic pseudo-octahedral iron complex crystallizes as a racemic crystal containing both enantiomers; the structure of the right-handed enantiomer can be seen in **Figure 2.3**.



**Scheme 2-3** Synthesis of 1,10-phenanthroline-5,6-dione and its iron complexes

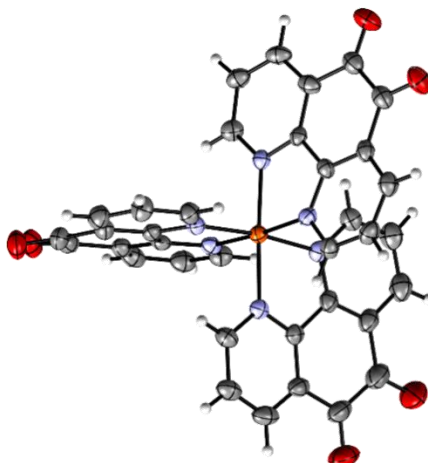


**Figure 2-3** Solid state structure of the cationic complex  $[2.4]^{2+}$  at 50% probability ellipsoids.

The electrochemistry of complex  $2.4(\text{BF}_4)_2$  in acetonitrile matches literature values with the  $\text{Fe}^{2+/3+}$  redox couple at 1.36 V vs. SCE and a single wave for the ligand reduction at -0.18 V, resulting into a potential difference of 1.54 V (**Figure 2.4**). The  $\text{Fe}^{2+/3+}$  redox couple is reversible and well separated from the ligand reduction, although the complex is

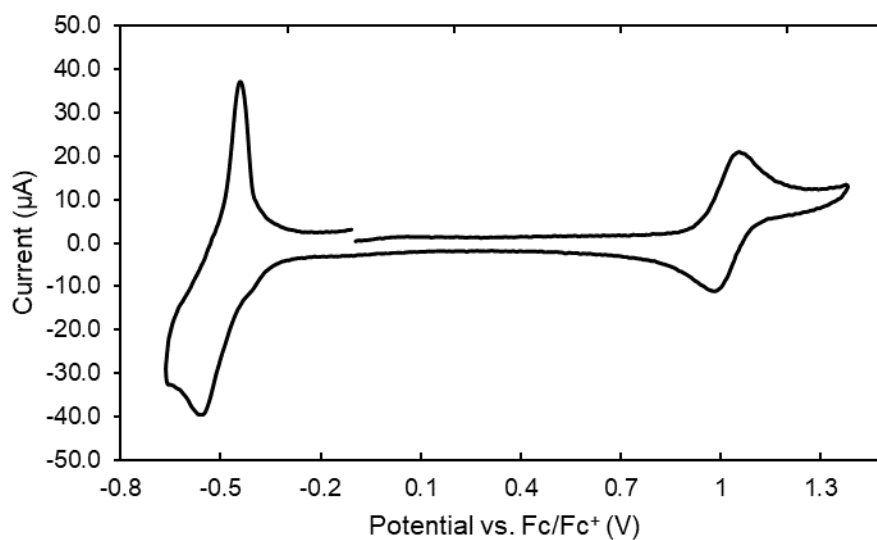


**Figure 2-4** CV of a 1 mmol solution of complex **2.4** at  $0.1 \text{ V s}^{-1}$  under argon. Conditions: 0.1 M TBAPF<sub>6</sub>, acetonitrile, glassy carbon disk working electrode, Pt wire counter-electrode, Ag/AgCl pseudo-reference electrode and internally referenced to ferrocene.

known to adsorb onto glassy carbon surfaces under reducing potentials in organic solvents. This was confirmed in the experimental voltammogram featuring a very narrow, symmetric feature corresponding to the oxidation of the ligand, which is suggestive of a non-diffusion process.

After preliminary characterization of the electrochemical behavior of **2.4**(BF<sub>4</sub>)<sub>2</sub> in acetonitrile, the corresponding iron sulfate complex was synthesized, aiming for increased water solubility. With the Fe<sup>2+/3+</sup> redox couple at a highly anodic potential, the use of an acidic solution was necessary in order to shift the reduction potential of water oxidation to more anodic potentials. Because of the pH dependence of the reduction of 1,10-phenanthroline-5-6-dione redox couple, the potential for ligand reduction was also shifted to 0.3 V vs. Ag/AgCl, at a potential that would avoid proton reduction while charging. However, at this pH the quinone redox couple had a large peak separation between oxidation and reduction that is consistent with electrochemically irreversible reactions and is detrimental for the kinetics of the system. The electrochemical irreversibility could be due to an equilibrium involving the partial hydrolysis of the dione to afford a geminal diol that is redox-inactive. This type of transformation is known to occur under acidic conditions.<sup>[92]</sup> In addition, the Fe<sup>2+/3+</sup> redox couple was no longer reversible at a pH of 2, with the reduction of generated Fe<sup>3+</sup> back to Fe<sup>2+</sup> producing very low current (**Figure 2.5**). Unfortunately, higher pH solutions could not be utilized for increasing the stability of the Fe<sup>2+/3+</sup> couple because of the aforementioned water oxidation, and so complex **2.4** was deemed unsuitable for further studies in aqueous solutions.

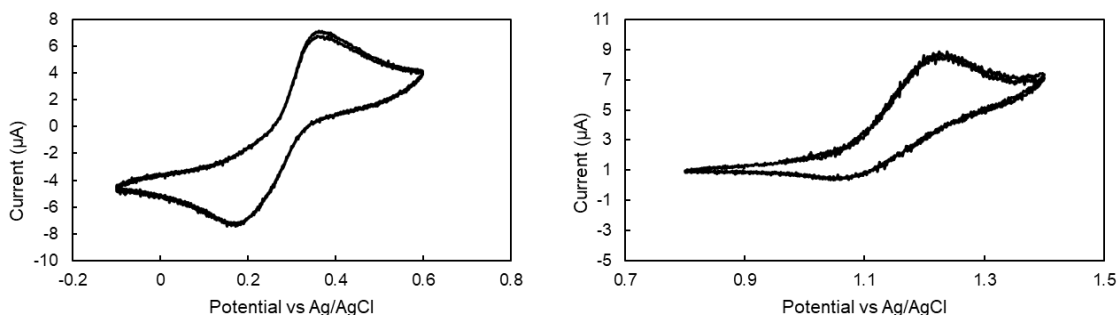
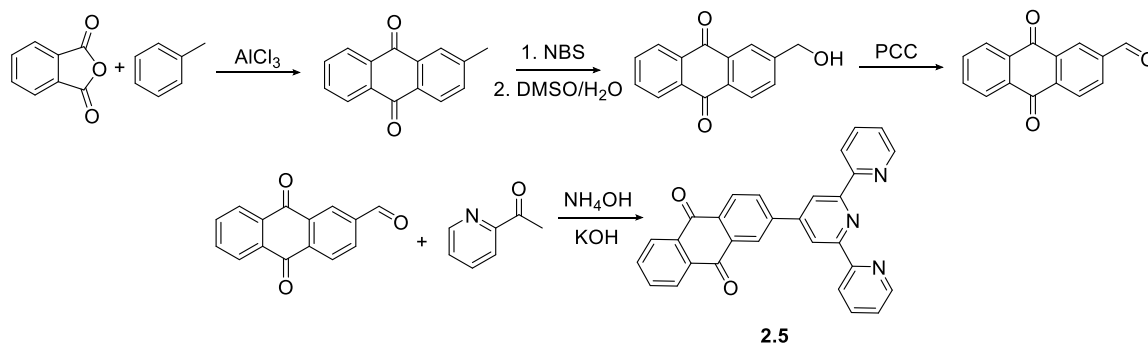


**Figure 2-5** CV of a 1mmol solution of complex **[2.4]**SO<sub>4</sub> at 0.1V s<sup>-1</sup> under argon. Conditions: 0.01 M HCl, water, glassy carbon disk working electrode, Pt wire counter electrode, saturated Ag/AgCl reference electrode.

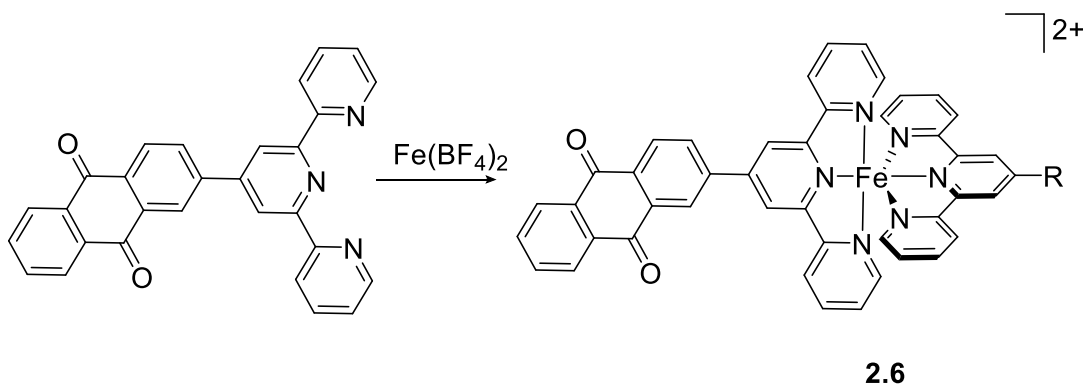
Based on the electrochemical results from complex **2.4**, a new ligand platform with greater stability of the Fe<sup>2+/3+</sup> redox couple and a ligand reduction that would be less prone to side reactivity was targeted. Computational work for screening a wide variety of quinone-based organic charge carriers regarded 9,10-anthraquinone frameworks as the most suitable candidates for the anolyte of an RFB, out of a total of 1710 computed redox couples.<sup>[95]</sup> In addition, utilizing a tridentate ligand such as terpyridine instead of a bipyridine backbone should increase the stability of the complex. With this in mind, a framework incorporating a 9,10-anthraquinone with a terpyridine central donor was identified as a potentially suitable ligand for an iron-based symmetric RFB. The para-substituted terpyridine **2.5** was synthesized, with the synthetic pathway building the central



**Scheme 2.4** Synthesis of 9,10-anthroquinone substituted terpyridine **2.5**

terpyridine framework from acetylpyridine, ammonia and a substituted aldehyde (**Scheme 2.4**).<sup>[96,97]</sup>

Multiple pathways for the synthesis of the 9,10-anthraquinone substituted aldehyde were attempted with the pathway that ultimately proved successful outlined in **Scheme 2.4**. A Friedel-Crafts acylation with toluene and phthalic anhydride afforded 2-methylantraquinone in high yields. This was subsequently brominated, hydrolyzed and oxidized in order to deliver 9,10-dioxo-9,10-dihydroanthracene-2-carbaldehyde as a light brown solid. The aldehyde was then reacted with 2-acetylpyridine and ammonium hydroxide to form the para-substituted terpyridine **2.5**. This was purified using column chromatography prior to complexation, with either iron sulfate or iron tetrafluoroborate affording the respective iron complexes (**Scheme 2.5**). When iron sulfate was used as an iron source, the resulting product was insoluble in water and had a low solubility in organic solvents, leading to the remainder of work focusing on the iron tetrafluoroborate complex **2.6**.



**Scheme 2-4** Synthesis of the iron coordination homoleptic complex **2.6**.

Layering a concentrated solution of **2.6** in acetonitrile with benzene resulted in what appeared to be a single-domain crystalline material, however, when the sample was sent to

the Canadian Light Source for analysis, it was polysynthetic in nature and only diffracted out to 1.8 Å. Additional crystallization attempts are ongoing in order to determine the solid state structure, although microcrystalline products are reproducibly obtained. ESI-MS confirmed the presence of the dication **2.6** as the most abundant species (ESI HRMS:  $m/z$  calc. for  $[\text{C}_{58}\text{H}_{34}\text{N}_6\text{O}_4\text{Fe}]^{2+}$ : 467.0990. Found: 467.1013). Electrochemical analysis by cyclic voltammetry in acetonitrile revealed an  $\text{Fe}^{2+/3+}$  redox couple at 0.74 V vs.  $\text{Fc}/\text{Fc}^+$  with approximately 61 mV peak separation, and a ligand reduction at -1.12 V with a 122 mV peak separation (**Figure 2.6**).

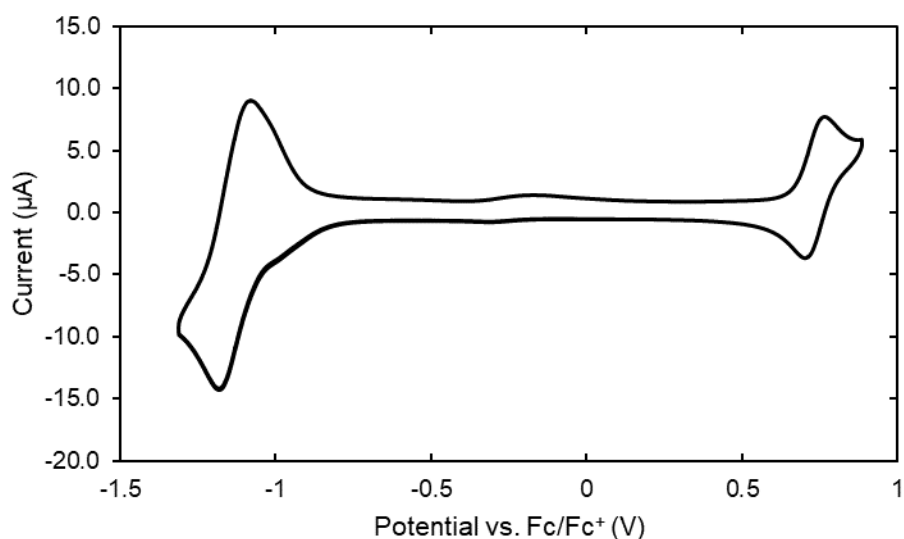
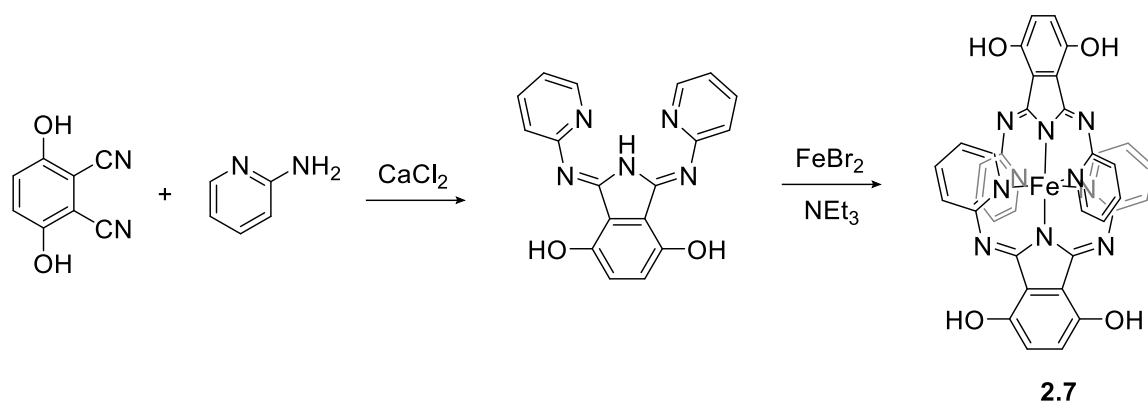


**Figure 2-6** CV of a 1mmol solution of complex **2.6** at  $0.1\text{ V s}^{-1}$  under argon. Conditions: 0.1 M TBAPF<sub>6</sub>, acetonitrile, glassy carbon disk working electrode, Pt wire counter electrode, Ag/AgCl pseudo-reference electrode and internally referenced to ferrocene.

A potential difference of 1.86 V is observed, with peak separations maintained across scan rates revealing an electrochemically reversible process. Furthermore, based on current density and peak separation, the ligand undergoes a two electron reduction process, leading to increased energy density for the anolyte solution without voltage losses. With

promising electrochemical features, cycling of the complex with an H-Cell and chronoamperometry is planned for future work but has not been completed to date.

An additional ligand scaffold was prepared parallel to the work on complex **2.6**, featuring a tridentate nitrogen based ligand and a hydroquinone/quinone functional group. With bipyridylimino isoindoline complexes showing promising reversibility and cycling as an anolyte, the corresponding hydroquinone 1,3-bis(2-pyridylimino)-4,7-dihydroxyisoindole was targeted.<sup>[83]</sup> The addition of alcohol functional groups on the parent bipyridylimino isoindoline framework could also tailor the solubility of the complex in polar solvents, in addition to providing a suitable redox couple for cycling efficiency. 1,3-bis(2-pyridylimino)-4,7-dihydroxyisoindole was synthesized by refluxing 2-amino pyridine and dicyanohydroquinone in 1-butanol with  $\text{CaCl}_2$  for 20 days.<sup>[98]</sup> The synthesis was low yielding (17%) but afforded the ligand in high purity for further complexation with anhydrous  $\text{FeBr}_2$  in the presence of a base (**Scheme 2.6**).<sup>[99]</sup> Other attempts at complexation included deprotonation of the ligand precursor with KHMDS and the use of  $\text{Fe}_2\text{Cl}_4(\text{THF})_3$  or anhydrous  $\text{FeCl}_2$ , although a crude black product was formed after each attempt. This was extracted with DCM and the solution was layered with pentane. This resulted in the precipitation of relatively large fraction of the material as an amorphous black solid that was filtered off, while a small amount of material crystallized on the walls of the vessel. A single crystal was analyzed by x-ray diffraction, revealing a neutral, homoleptic iron complex with a pseudo-octahedral geometry. The resulting solid-state structure shows hydrogen bonding between the alcohols and imines of the ligand, assisting a planar structure with a conjugated  $\pi$  system (**Figure 2.7**).



**Scheme 2-5** Synthesis of the homoleptic iron complex **2.7**

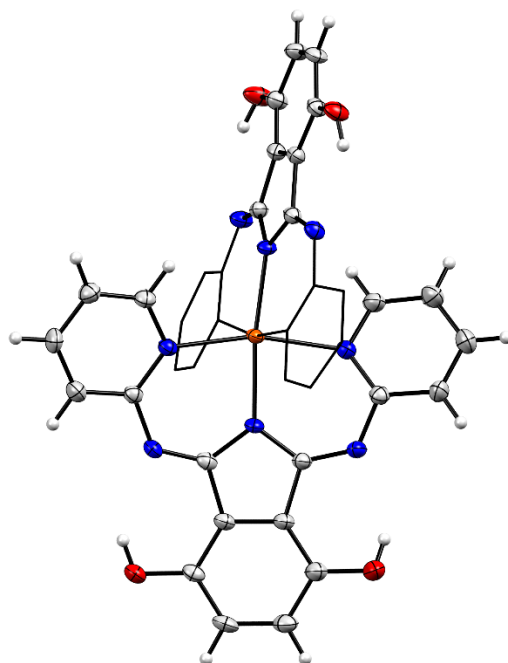


**Figure 2-7** Solid-state structure of pseudo-octahedral complex **2.7** in a combination of thermal ellipsoids at 50% probability and wireframe.

Attempts at large scale purification of **2.7** were unsuccessful, in each case yielding the same amorphous black precipitate that was difficult to characterize and did not provide a satisfactory elemental analysis. Cyclic voltammetry of this product **2.7** showed multiple redox features and poor resolution. With a low-yielding ligand synthesis and poor



electrochemical results after unsuccessful attempts at purification, investigations of complex **2.7** were halted and efforts were directed towards the aforementioned complex **2.6**.

## **2.4 Conclusion**

The synthesis and characterization of iron coordination complexes for targeted use in redox flow batteries has been discussed. An all-iron, all-soluble system based on  $[\text{Fe}(\text{bpy})_3]^{2+}$  and complex **2.2** revealed a potential difference of 0.92 V with reversible  $\text{Fe}^{2+/3+}$  redox couples, all within the solvent window of water. The syntheses of both complexes was scaled up for chronoamperometry testing in an H-Cell. Although the use of some quinone-based ligands resulted in poor electrochemical behavior (**2.4**) or difficulty in purification (**2.7**), an iron coordination complex featuring an anthraquinone-substituted terpyridine **2.6** shows promising redox activity as a single complex for anolyte and catholyte solutions. It should be noted that the solubility of the aforementioned complexes is lower than required for practical applications, but they could be functionalized with solubilizing groups in subsequent studies in order to increase the energy density of the system.

## **2.5 Experimental**

### **Ligand 2.1**

Pyridine-2,6-dicarboxylic acid (14.460g, 86.5mmol), 2,2-dimethylpropane diamine (24.00mL, 200mmol) and p-toluenesulfonic acid monohydrate (1.335g, 7mmol) were placed in a 250 mL round bottom flask equipped with magnetic stirrer and refluxed overnight in 150 mL of ethylene glycol. After cooling the resulting solution in an ice bath, the white solid that precipitated was collected by filtration and suspended in water (20 mL)

in an ultrasonic bath in order to remove residual glycol. The suspension was filtered and washed with slight amounts of acetone to afford compound **2.1** (17.031g, 66% yield) as a white powder.  $^1\text{H}$  NMR (400 MHz, methanol- $d_4$ ):  $\delta$  1.00 (s, 12H), 3.14 (s, 8H), 7.92 (t, 1H), 8.11 (d, 2H,).  $^{13}\text{C}$  NMR (101 MHz, methanol- $d_4$ )  $\delta$  25.3, 27.0, 54.6, 122.8, 138.9, 151.2, 153.7.

### Complex 2.2

Compound **2.1** (10.000g, 33.4mmol) and iron (II) sulfate heptahydrate (3.704 grams, 13.3mmol) were placed in a 250 mL round bottom flask equipped with a magnetic stirrer and stirred overnight in 100mL of de-ionized water at room temperature. Afterwards, the water was removed in-vacuo and the resulting solid washed with acetone to remove additional ligand to afford complex **2.2** (10.780g, 86% yield) as a dark purple solid. MS (ESI HRMS):  $m/z$  calc. for  $[\text{C}_{34}\text{H}_{50}\text{N}_{10}\text{Fe}]^{2+}$ : 327.1779. Found: 327.1785.

### Complex 2.3

Ligand **2.1** (450 mg, 1.51 mmol) and cobalt(II) chloride hexahydrate (180 mg, 0.75 mmol) were refluxed overnight in methanol (15 mL) in a 100mL round bottom flask equipped with a magnetic stir bar under ambient atmosphere. The resulting black precipitate was subsequently filtered off and the filtrate was evaporated to dryness with a rotary evaporator. Complex **3** was isolated as a yellow-green solid. (402 mg, 73% yield).  $^1\text{H}$  NMR (400 MHz,  $\text{D}_2\text{O}$ ):  $\delta$  0.81 (s, 12H), 1.97 (s, 4H), 3.17 (s, 4H), 8.52 (d, 2H), 8.79 (t, 1H).  $^{13}\text{C}$  NMR (101 MHz,  $\text{D}_2\text{O}$ )  $\delta$  24.2, 27.8, 49.9, 54.3, 126.0, 143.8, 153.7, 157.2. HRMS (ESI):  $m/z$  calcd for  $\text{C}_{34}\text{H}_{49}\text{N}_{10}\text{CoCl}$ : 691.3162, found: 691.3138.

### **Fe(Bpy)<sub>3</sub>SO<sub>4</sub>**

2,2'-bipyridine (7.780g, 50mmol) and iron (II) sulfate heptahydrate (4.615g, 16.6mmol) were placed in a 250 mL round bottom flask equipped with a magnetic stirrer and stirred overnight in 100mL of de-ionized water at room temperature. Afterwards, the water was removed in-vacuo and the resulting iron complex was collected (10.305g, quantitative) MS (ESI HRMS):  $m/z$  calc. for  $[C_{30}H_{24}N_6Fe]^{2+}$ : 262.0700. Found: 262.0703.

### **1,10-phenanthroline-5,6-dione**

1,10-phenanthroline (2.000g, 11mmol) and KBr (2.001g, 17mmol) were dissolved in 20mL of  $H_2SO_4$  and 10mL of  $HNO_3$  in a 100mL round bottom flask equipped with a magnetic stir bar and reflux condenser. The resulting solution was heated to reflux for three hours, after which the solution was poured over 500mL of ice. The acidic solution was then neutralized with a 2M NaOH solution until the pH of the resulting solution was between 6 and 7, then the product was extracted out of the aqueous layer with 3 fractions of  $CHCl_3$  (50mL). The resulting organic solution was dehydrated with anhydrous  $Na_2SO_4$  and filtered, then brought to dryness under reduced pressure to afford 1,10-phenanthroline-5,6-dione (1.750g, 75% yield) as a yellow solid.  $^1H$  NMR (400 MHz, Chloroform-*d*)  $\delta$  9.09 (dd, 1H), 8.47 (dd, 1H), 7.57 (dd, 1H).  $^{13}C$  NMR (101 MHz,  $CDCl_3$ )  $\delta$  178.62, 156.38, 152.86, 137.29, 128.04, 125.61.

### **[2.4]SO<sub>4</sub>**

For testing in aqueous solutions, 1,10-phenanthroline-5,6-dione (1.000g, 4.8mmol) and  $FeSO_4(H_2O)_7$  (0.440g, 1.6mmol) were dissolved in 10mL of methanol and heated to reflux over a period of three hours. After cooling, the resulting solution was evaporated to dryness under reduced pressure and washed with slight amounts of acetone to afford **[2.4]SO<sub>4</sub>** (1.223g, 97% yield) as a dark red solid. For testing in organic solutions,  $Fe(BF_4)_2(H_2O)_6$

was used in place of  $\text{FeSO}_4(\text{H}_2\text{O})_7$ , however the procedure remained otherwise the same.

MS (ESI HRMS):  $m/z$  calc. for  $[\text{C}_{36}\text{H}_{18}\text{N}_6\text{O}_6\text{Fe}]^{2+}$ : 343.0313. Found: 343.0301.

### **Compound 2.5**

Phthalic anhydride (10.050g, 67.8mmol) and 40g of toluene were placed in a 250mL 3-neck round bottom flask equipped with a magnetic stir bar and connected to a bubbler under inert atmosphere. After cooling the suspension to 0 °C, anhydrous  $\text{AlCl}_3$  (20.072g, 151mmol) was added through a side arm with positive argon pressure and immediate HCl gas was formed. After 15 minutes, the solution became dark orange and was heated to 95°C over a period of 30 minutes and maintained at 95 °C for 2.5 hours. After heating, the solution was cooled in an ice bath and ice water was added to quench any residual  $\text{AlCl}_3$ . After quenching, 20mL of concentrated HCl was added to precipitate out carboxylic acid intermediate (16.840g) as a white powder, which was subsequently washed with cold water. After drying, the carboxylic acid intermediate was dissolved in 50mL of fuming sulfuric acid and heated to 100°C under inert atmosphere for 2 hours. After heating, the resulting solution was cooled in an ice bath and deionized water was added dropwise. The resulting suspension was filtered and washed with plenty of water to yield 2-methyl-9,10-Anthracenedione (12.247g, 81% yield) as a dark brown solid.

2-methyl-9,10-Anthracenedione (9.581g, 43mmol), N-bromosuccinimide (8.554g, 48mmol) and benzoyl peroxide (1.710g, 7mmol) were dissolved in 85mL of carbon tetrachloride in a 250mL round bottom flask equipped with a magnetic stir bar. The resulting solution was heated to reflux over a period of 24 hours, then cooled to room temperature. The resulting suspension was filtered and washed with 100mL of 20% NaOH,

followed by water and slight amount of acetone to yield 2-(bromomethyl)-9,10-Anthracenedione (11.945g, 92% yield) as a yellow solid.

2-(bromomethyl)-9,10-Anthracenedione (11.945g, 40mmol) was suspended in a DMSO/H<sub>2</sub>O mixture, (450mL DMSO and 650mL of H<sub>2</sub>O), and heated to 100 °C for 24 hours in a 2L three-neck round bottom flask equipped with a magnetic stir bar and reflux condenser. After heating, the solution was filtered while hot, and the filtrate cooled to room temperature precipitating the product from solution. The solid was collected by filtration to yield 2-(hydroxymethyl)-9,10-Anthracenedione as a brown solid (6.250g, 66% yield).

2-(hydroxymethyl)-9,10-Anthracenedione (6.250g, 26mmol) and pyridinium chlorochromate (8.125g, 38mmol) were dissolved in 315mL of dichloromethane in a 1L round bottom flask equipped with a magnetic stir bar. The resulting solution was heated to reflux for 12 hours. After heating, volatiles were removed with a rotary evaporator and the resulting solid was washed with water and acetone to remove residual starting material. After washing, 9,10-dihydro-9,10-dioxo-2-anthracenecarboxaldehyde (5.293g, 86% yield) was obtained as a light brown solid.

9,10-dihydro-9,10-dioxo-2-anthracenecarboxaldehyde (3.000g, 12.7mmol) was dissolved in 1.0L of ethanol, and a separate solution containing 2-acetylpyridine (3.020g, 25mmol), KOH (2.80g, 50mmol) and 100mL of concentrated ammonium hydroxide was added dropwise. The resulting suspension was stirred at room temperature for 24 hours, then heated to reflux for an additional 4 hours. After heating, the suspension was filtered and washed with ethanol to yield 4'-[9,10-Dioxo-9,10-dihydroanthracen-2-yl]-2,2':6',2''-terpyridine **5** (2.440g, 44% yield) as a crude light brown solid. This product was then purified by column chromatography using CHCl<sub>3</sub>, DCM, and THF as eluents.

### Complex 2.6

Complexation attempts with FeSO<sub>4</sub> resulted in insoluble precipitates, so complexes with Fe(BF<sub>4</sub>)<sub>2</sub> was used instead. Compound **2.5** (15mg, 0.03mmol) and Fe(BF<sub>4</sub>)(H<sub>2</sub>O)<sub>6</sub> (6mg, 0.015mmol) were dissolved in 10mL of acetonitrile in a 50mL round bottom flask equipped with a magnetic stir bar and reflux condenser. The resulting solution turned immediately to a dark purple solution, then was heated to reflux for 24 hours. After heating, the solution was evaporated to dryness in vacuo and the purple powder was subsequently washed with THF and pentane to remove residual impurities. MS (ESI HRMS): *m/z* calc. for [C<sub>58</sub>H<sub>34</sub>N<sub>6</sub>O<sub>4</sub>Fe]<sup>2+</sup>: 467.0990. Found: 467.1013.

### 1,3-bis(2-pyridylimino)-4,7-dihydroxyisoindole

Dicyanohydroquinone (1.002g, 6.3mmol), 2-aminopyridine (1.230g, 13.1mmol) and CaCl<sub>2</sub> (0.140g, 1.3mmol) was added to a 100mL round bottom flask equipped with a magnetic stir bar and refluxed in 20mL of n-butanol over a period of 20 days under inert atmosphere. After refluxing, the resulting solution was poured into 500mL of water resulting in the precipitation of a yellow-brown solid. The resulting precipitate was collected by filtration and washed with 20mL of deionized water to remove residual n-butanol. The crude product was then dried in vacuo and subsequently washed with slight amounts of dichloromethane to yield 1,3-bis(2-pyridylimino)-4,7-dihydroxyisoindole (0.350g, 17% yield) as a yellow solid. <sup>1</sup>H NMR (400 MHz, Chloroform-*d*) δ 13.36 (s, 1H), 8.58 (ddd, 2H), 7.76 (td, 2H), 7.36 (dt, 2H), 7.13 (ddd, 2H), 7.01 (s, 2H). <sup>13</sup>C NMR (101 MHz, CDCl<sub>3</sub>) δ 159.29, 154.87, 149.02, 147.98, 138.15, 122.47, 121.43, 120.40, 116.26.

### Complex 2.7

1,3-bis(2-pyridylimino)-4,7-dihydroxyisoindole (350mg, 1mmol) and anhydrous FeBr<sub>2</sub> (112mg, 0.5mmol) was dissolved in 9mL of anhydrous methanol in a 2-neck 100mL round bottom flask attached to a swivel frit apparatus. The resulting solution was brought to reflux and 1mL of trimethylamine was added to the reaction vessel, in which heating was continued for an additional 16 hours. After cooling the solution, the resulting suspension was filtered through the swivel frit apparatus, and the collected solid dried in vacuo resulting in a crude mixture containing iron complex **7** (260mg, 72% yield) as an opaque solid. Single crystals suitable for x-ray diffraction were grown by layering a concentrated DCM solution with pentane over a period of three days. MS (ESI HRMS):  $m/z$  calc. for [C<sub>36</sub>H<sub>25</sub>N<sub>10</sub>O<sub>4</sub>Fe]<sup>+</sup>: 717.1410. Found: 717.1413.

## Chapter 3 – Introduction to the Electrochemical Reduction of Carbon Dioxide

### 3.1 Background Information

Another alternative in mitigating the increasing concentrations of atmospheric carbon dioxide is its electrochemical reduction. When the supply of renewable energy exceeds demand, the excess energy can be stored in chemical bonds, converting carbon dioxide into fuels or value added chemicals.<sup>[100]</sup> This could enable a carbon-neutral cycle where applications such as aviation/shipping can still utilize hydrocarbon-based fuels without a net-increase in CO<sub>2</sub> emissions.<sup>[101]</sup>

The electrochemical reduction of CO<sub>2</sub> is an energetically and kinetically challenging process. The single electron reduction of the CO<sub>2</sub> molecule requires significant reorganizational energy to form an unstable radical anion, leading to a large thermodynamic barrier to reduction.<sup>[102]</sup> The use of proton-coupled multielectron reduction can circumvent this problem, but leads to a multitude of different potential products. **Table 3.1** summarizes a few of the possible reductive pathways with the corresponding potentials. Because some of the equations involve proton-coupled processes, the reduction of protons to dihydrogen also needs to be considered as a competitive process. Typically, hydrogen production is thermodynamically favored or comparable to the reduction of carbon dioxide and needs to be kinetically controlled or have a relatively high overpotential based on the electrodes/catalysts that are used. As seen in **Table 3.1**, the use of multiple proton-coupled electron transfers for the reduction of CO<sub>2</sub> is also favored over the two electron, two proton reduction pathways, however, it requires multiple bond breaking and bond forming elemental steps. This renders the electrochemical reduction of carbon dioxide to highly reduced carbon products such as methane and methanol extremely challenging to target



with a homogeneous single-site catalyst or heterogeneous systems.<sup>[102]</sup> Reducing carbon dioxide *via* a two electron, two proton process is much more feasible, leading to the majority of reported catalysts for the electrochemical reduction of CO<sub>2</sub> producing carbon monoxide or formic acid.<sup>[103]</sup> Carbon monoxide is a highly valuable synthon for well established, large scale industrial process such as the Fisher-Tropsch process for the production of fuels.

**Table 3-1** Standard Reduction Potentials in aqueous solutions for selected CO<sub>2</sub> reduction pathways (Referenced to SHE)

Reduction Process	E <sup>0</sup> (V)
$\text{CO}_2 + \text{e}^- \rightarrow \text{CO}_2^{\bullet -}$	-1.90
$2\text{CO}_2 + 2\text{e}^- \rightarrow \text{C}_2\text{O}_4^{2-}$	-0.59
$\text{CO}_2 + 2\text{H}^+ + 2\text{e}^- \rightarrow \text{HCOOH}$	-0.25
$\text{CO}_2 + \text{H}_2\text{O} + 2\text{e}^- \rightarrow \text{HCOO}^- + \text{OH}^-$	-1.08
$\text{CO}_2 + 2\text{H}^+ + 2\text{e}^- \rightarrow \text{CO} + \text{H}_2\text{O}$	-0.11
$\text{CO}_2 + \text{H}_2\text{O} + 2\text{e}^- \rightarrow \text{CO} + 2\text{OH}^-$	-0.93
$\text{CO}_2 + 4\text{H}^+ + 4\text{e}^- \rightarrow \text{CH}_2\text{O} + \text{H}_2\text{O}$	-0.07
$\text{CO}_2 + 6\text{H}^+ + 6\text{e}^- \rightarrow \text{CH}_3\text{OH} + \text{H}_2\text{O}$	+0.02
$\text{CO}_2 + 8\text{H}^+ + 8\text{e}^- \rightarrow \text{CH}_4 + 2\text{H}_2\text{O}$	+0.17

The field for electrochemical reduction of CO<sub>2</sub> started with copper and zinc metal cathodes in 1904.<sup>[104]</sup> However, heterogeneous catalysts can feature different faces, defects and surface sites for activation, leading to poor selectivity. The selectivity issues are difficult to address, as solid-state catalysts are challenging to modify the chemistry that occurs at the surface and is difficult to investigate.<sup>[105,106]</sup> A wide variety of electrodes have been tested for CO<sub>2</sub> reduction, with product selectivity falling under three general categories. In a bicarbonate buffer, late transition metals such as Sn, Pb, Tl, Hg and Cd

produce formate at potentials more negative than -1.5V vs. SHE. Precious metals, including Ag, Au and Pd lead to CO as the major carbon-containing product, at potentials more negative than -1.1V, while copper produces multiple different products, including CH<sub>4</sub>, CO, and formate.<sup>[107]</sup> It is important to note that the parasitic reduction to dihydrogen generally occurs in appreciable amounts (5-20%) and side reactions leading to other carbon-containing products are common. Although continued development has provided heterogeneous systems such as silver nanoparticles with high levels of activity and faradaic efficiency,<sup>[108,109]</sup> the remainder of this work will focus on the use of homogenous single-site catalysts.

### **3.2 Homogeneous Catalysis for the Electrochemical Reduction of CO<sub>2</sub>**

The field of homogeneous electrochemical reduction of CO<sub>2</sub> started in the 1970s with metal phthalocyanines and porphyrins.<sup>[110–112]</sup> A few other homogeneous catalysts emerged in the following decade including rhenium bipyridine,<sup>[113,114]</sup> iron porphyrins/clusters<sup>[115,116]</sup> and other complexes utilizing nitrogen-based macrocycles<sup>[117]</sup>. Advantages of homogeneous single-site catalysts include the high tunability and comparable ease of study, which has led to a diverse derivatization of the aforementioned catalysts and provided mechanistic insight into CO<sub>2</sub> reduction.

However, although the field of electrochemical reduction of CO<sub>2</sub> is well established, the use of different conditions during electrolysis and the relationship between overpotential and catalytic activity has hindered the comparison between reported catalysts. A recent benchmark in the field involves the use of a “Tafel plot” which provides the relationship between overpotential and turnover frequency with a specific catalyst. When overlaying different catalysts, the Tafel plot allows for a quick, visual comparison,

with the highest performers in the top left quadrant of the graph at a low overpotential and high turnover frequency. Selected catalysts are shown in **Figure 3.1** with their corresponding Tafel plot to show the relationship between overpotential and turnover frequency.<sup>[118]</sup> Other important metrics include turnover numbers relating to the stability of the catalyst and faradaic efficiency to identify the selectivity of carbon dioxide reduction over dihydrogen production.

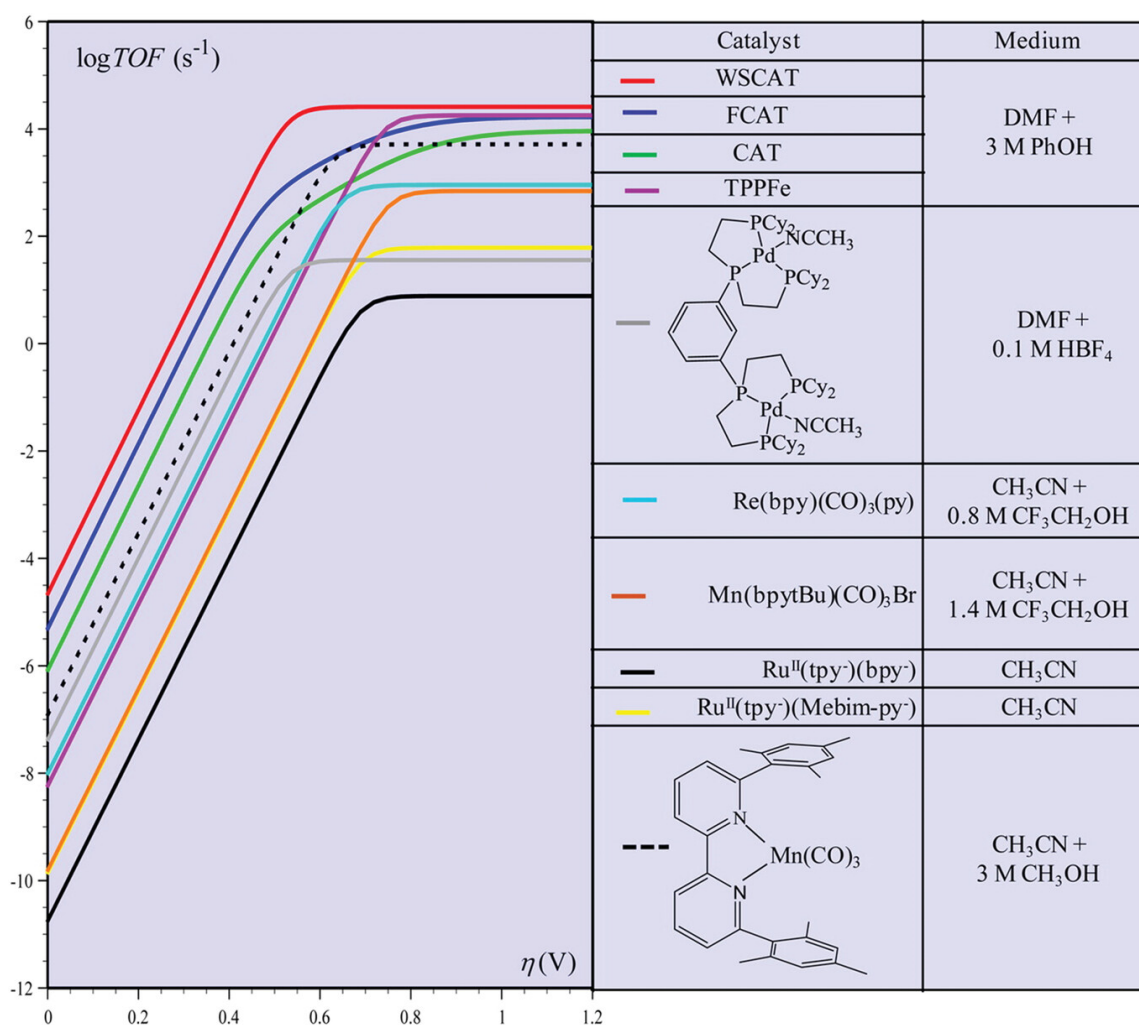


**Figure 3-1** Tafel plots of selected catalysts for the electrochemical reduction of CO<sub>2</sub> to CO. (Abbreviations: iron tetraphenylporphyrin (TPPFe), *o,o'*-phenolic-TPPFe (CAT), bis(*o,o'*-phenolic)bis(pentafluorophenyl)-TPPFe (FCAT), *p*-trimethylammonium-TPPFe (WSCAT). Reproduced with permission from reference 118.

### 3.3 Mechanistic Insight and Ligand Design Considerations

The proposed reduction pathways on molecular catalysts involve multiple electron transfers and chemical transformations in sequence, with the order of elemental steps under slight variation depending on the catalyst under study. Proton-coupled electron transfers (PCET) are also present under certain conditions, lowering the activation energy in catalytic cycles and increasing the rate of catalysis.<sup>[119–121]</sup> For the formation of CO, the reduced active species in solution undergoes nucleophilic attack onto the carbon dioxide molecule, leading to a charge transfer into its  $\pi^*$  orbital and  $\eta^1$ -binding through carbon. This effectively reduces the  $\text{CO}_2$  molecule upon coordination, leading to a bent geometry similar to the singly reduced radical anion.<sup>[103]</sup> Two subsequent protonation and reduction (or PCET) steps leads to C-O cleavage and the loss of water, followed by the dissociation of CO and regeneration of the active catalyst in solution. This protonation/reduction sequence largely depends on the catalyst that is being used and can

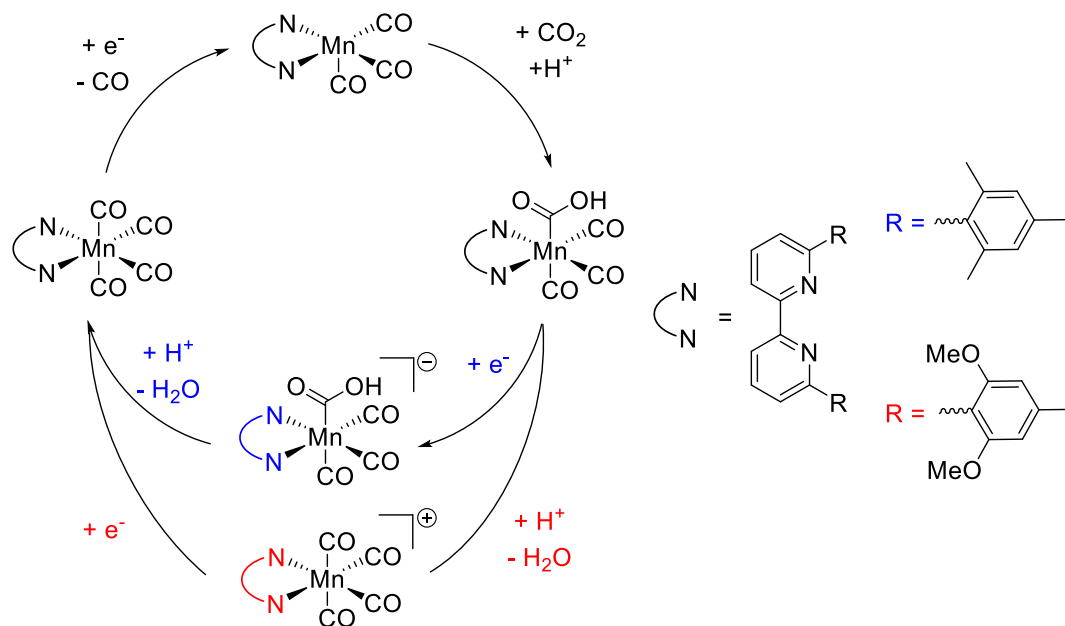


**Figure 3-2** Mechanism of  $\text{CO}_2$  reduction with selected manganese catalysts

also be further tuned with ligand modification (**Figure 3.2**).<sup>[122,123]</sup>

The use of Brønsted or Lewis acids to stabilize the metallocarboxylate and assist in cleaving one of the C-O bonds can lead to further rate enhancement; for example, varying levels of alkaline earth metals and have shown pseudo-first order kinetics in combination with iron porphyrins. Pseudo-second order kinetics were observed with the use of alkali metals and weak Brønsted acids with the aforementioned catalyst, leading to  $\text{CO}_3^{2-}/\text{CO}$  and  $\text{H}_2\text{O}/\text{CO}$  products respectively by a “push-pull” mechanism.<sup>[124,125]</sup> The use of weak Brønsted acids has continued to be utilized throughout the field for  $\text{CO}_2$  reduction across a variety of catalysts, although the use of stronger Brønsted acids has been hindered by the propensity for strong acids to assist dihydrogen production under reducing conditions. This has been circumvented through appropriate ligand design, where ligands incorporating phenolic groups, amines and amides in the secondary coordination sphere increases the “local proton concentration” around the activated  $\text{CO}_2$  molecule, without the presence of strong acids in solution. Initially shown on the iron-porphyrin system,<sup>[126–128]</sup> the use of high local-proton concentration has been tested across ligand platforms including bipyridine<sup>[129,130]</sup> and nitrogen-based macrocycles,<sup>[131,132]</sup> reducing the overpotential and increasing the turnover frequency compared to that of the parent systems.

Because multiple electrons are needed to reduce  $\text{CO}_2$  to value-added products, redox noninnocent frameworks are traditionally used in order to accommodate additional electron density and lead to anodic shifts in the reduction potential. Some of the parent frameworks have been modified with electron-withdrawing groups to shift the reduction to even more anodic potentials. One such example involved the replacement of meso-phenyl groups in an iron-tetraphenylporphyrin complex with 1, 2, 3 or 4 pentafluorophenyl groups,

respectively. Electrochemical analysis of the corresponding iron complexes showed a decrease in overpotential alongside an undesired decrease in catalytic activity with additional pentafluorophenyl groups.<sup>[133,134]</sup> The decreased rate and overpotential could be explained by additional electron density being delocalized across the porphyrin framework, leading to a less nucleophilic metal center and enabling a more anodic reduction potential. Surprisingly, when the meso-phenyl groups were substituted at the ortho-position with trimethylanilinium groups, the electron withdrawing nature of the ammonium group lowered the overpotential and led to an unprecedented *rise* in catalytic activity. The increase in catalytic activity is due to through-space coulombic interactions with the initial CO<sub>2</sub> adduct, leading to the most active molecular catalyst to date. A maximum turnover frequency (TOF<sub>max</sub>) of 10<sup>6</sup> s<sup>-1</sup> at an overpotential of 220mV was determined for the electrochemical reduction of CO<sub>2</sub> to CO, and no significant catalyst degradation was observed over 3.5 days of electrolysis.<sup>[135]</sup>

The highest turnover frequency in a manganese-based catalyst also stemmed from modification of a ligand framework, with incorporation of electron donating substituents in contrast to the use of secondary sphere effects. The secondary sphere effects of methoxy or phenoxy groups have led to increased rates and decreased overpotentials.<sup>[122,136,137]</sup> The highest reported TOF<sub>max</sub> for a manganese based catalyst (320,000 s<sup>-1</sup>) were achieved by replacing 2,2'-bipyridine for a bidentate N-heterocyclic carbene ligand in Mn(bpy)(CO)<sub>3</sub>Br.<sup>[138]</sup> The strongly donating carbene ligands imposing nucleophilic character on the manganese center are responsible for the increased activity, however, at the expense of a more cathodic reduction potential.<sup>[138]</sup>

Other modifications on group 7 bipyridine catalysts include the functionalization of the 6,6'-positions with bulky tert-butyl or mesityl groups.<sup>[139]</sup> Monitoring CO stretching frequencies by infrared spectroelectrochemistry (IR-SEC) has provided insight into dimerization of manganese and rhenium complexes after halide dissociation, which is prevented by the addition of bulky substituents on the bipyridine 6,6'-positions.<sup>[123]</sup> In addition to increasing the stability of the complex through ligand modification, the singly reduced manganese monomer reduces at more positive potentials than the corresponding dimer, leading to a reduction in overpotential.

### 3.4 Conclusion

The aforementioned examples are meant to highlight the importance of ligand design and emphasize that slight modifications can impart substantial rate improvements and shift the reduction of CO<sub>2</sub> to more anodic potentials. There has been significant advancement in ligand design for CO<sub>2</sub> reduction over the last few decades, including the use of local proton concentrations, electron-withdrawing groups, coulombic interactions, redox-noninnocent frameworks and steric protection. These design principles have led to higher turnover numbers and frequencies, greater stability, lower overpotentials and higher faradaic efficiencies for reported catalysts. High overpotentials and lack of selectivity still render large-scale conversion of CO<sub>2</sub> to fuels economically unfeasible at this time.<sup>[140]</sup> Most of the development in the field for electrocatalytic reduction of CO<sub>2</sub> has involved the functionalization and derivatization of previously known molecular electrocatalysts, with novel ligand designs less common. **Figure 3.3** shows some of the common ligand platforms that continue to be utilized in catalysts for the electrochemical reduction of CO<sub>2</sub>.

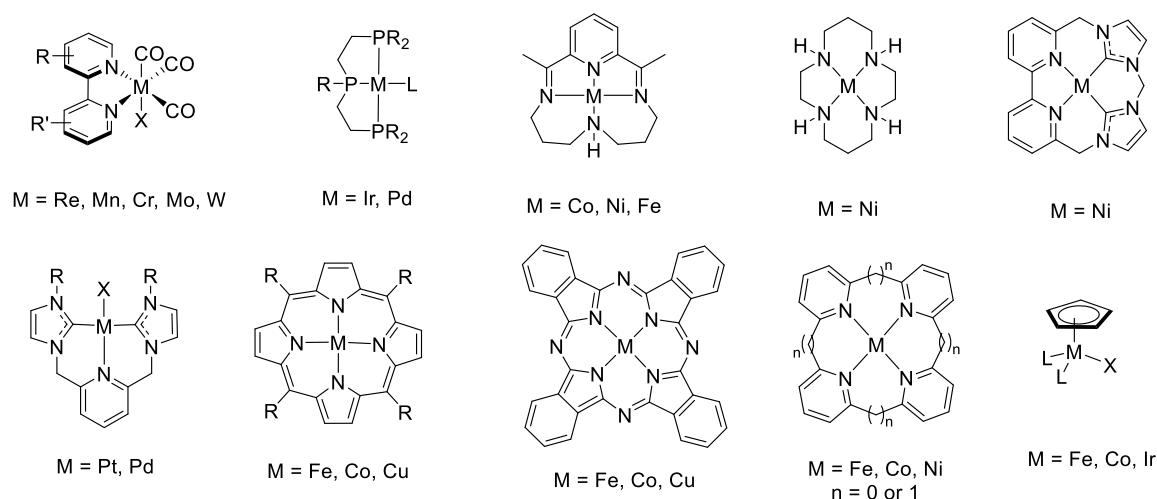


**Figure 3-3** Selected complexes with common ligand platforms electrocatalytic reduction of CO<sub>2</sub> [103,141–143]

The development of future catalysts needs to incorporate the design principles outlined by previous studies while targeting high affinity for CO<sub>2</sub> and stability across multiple oxidation states. Difficulties associated with the development of new catalysts stem from the harsh catalytic conditions under reducing potentials, the kinetic challenges to reduce the parasitic reduction of dihydrogen, maintaining high levels of activity towards CO<sub>2</sub>, and providing a low overpotential for reduction. The contents of original work presented in the following two chapters apply some of the aforementioned design principles in novel ligand platforms, with the aim of identifying new complexes active for CO<sub>2</sub> reduction. Selection criteria for new ligands focuses on the ability to be synthetically accessible in gram quantities and form complexes that are stable under reducing conditions. A redox-active framework and low overpotentials, as well as a high selectivity for CO<sub>2</sub> reduction over dihydrogen production are also desired. The synthesis and characterization redox non-innocent ligands and their complexes is discussed, in addition to mechanistic insights into decomposition pathways for nickel-based complexes.



## Chapter 4 – Ligand-Centered Electrochemical CO<sub>2</sub> Reduction with a Nickel

### bis(triazapentadienyl) Complex<sup>[144]</sup>

#### 4.1 Author Contributions

A portion of this chapter is reproduced from reference 144 with permission from the Royal Society of Chemistry, in which multiple authors from the Department of Chemistry contributed to the manuscript. Demyan Prokopchuk, Zachary Dubrawski, Joshua Heidebrecht, Janina Willkomm, Alexander Hyla and Braulio Puerta Lombardi contributed to the preparation of the initial draft, with further edits and proof reading from Chase Radford, Gregory Welch, Roland Roesler and Warren Piers. Zachary Dubrawski and Demyan Prokopchuk carried out the work presented in subsection 4.3, including cyclic voltammetry, controlled potential electrolysis (CPE), synthesis of Ni(TAPPy)<sub>2</sub> and characterization of the post-CPE isolated solids. All synthetic work and electrochemical analysis within subsections 4.4 to 4.6 was performed solely by Joshua Heidebrecht, with the exception of calculated frequencies for [Ni(TAPPy)(CO)<sub>2</sub>]<sup>-</sup> (Alexander Hyla) and CPE experiments performed in the presence of [Ni(TMC)]<sup>2+</sup> (Demyan Prokopchuk). For additional electrochemical analysis and synthetic characterization on Ni(TAPPy)<sub>2</sub>, the reader is directed to reference 144.

#### 4.2 Background Information

One of the first types of molecular catalysts for electrochemical CO<sub>2</sub> reduction was based on macrocycles of nickel and cobalt.<sup>[117]</sup> From the initial study, a nickel complex featuring a redox-inactive cyclam ligand was the most promising in terms of faradaic efficiency, product selectivity and a relatively low overpotential for the electrochemical reduction of CO<sub>2</sub> to carbon monoxide. However, even though seminal work by Eisenberg

utilized spectator ligands, the field for molecular electrochemical reduction of CO<sub>2</sub> has largely involved the use of redox-active ligands.<sup>[103,141–143,145]</sup> Several Mn,<sup>[146]</sup> Fe,<sup>[115,147]</sup> Ni,<sup>[148–152]</sup> and Cu<sup>[153,154]</sup> electrocatalysts incorporating such ligands have been reported, capable of reducing CO<sub>2</sub> to either C<sub>2</sub>O<sub>4</sub><sup>2-</sup> or CO in aprotic organic solvents. Nickel-based electrocatalysts that promote the conversion of CO<sub>2</sub> into CO<sub>3</sub><sup>2-</sup> or C<sub>2</sub>O<sub>4</sub><sup>2-</sup> are presented in **Fig. 4.1**.

Trimetallic diphosphine-bridged complexes (**A**) have been studied for electrocatalytic CO<sub>2</sub> reduction to produce CO/CO<sub>3</sub><sup>2-</sup>.<sup>[149,155]</sup> The similar potential ( $E_{pc}$  = 1.46 to 1.56 V vs. Fc<sup>+0</sup>, MeCN) to generate the electroactive species for this family of compounds is due to the metal-based LUMO, which has little dependence on the nature of capping ligand L.<sup>[156]</sup> The bimetallic isocyanide complex **B** is also a CO/CO<sub>3</sub><sup>2-</sup> electrocatalyst under aprotic conditions ( $E_{pc}$  = 1.0 V vs. Fc<sup>+0</sup>, MeCN).<sup>[151]</sup> According to DFT calculations, the LUMO of **B** is delocalized across the metal centers and isocyanide ligands. The complex Ni(bpy)Br<sub>2</sub> (**C**) is capable of producing CO/CO<sub>3</sub><sup>2-</sup> ( $E_{pc}$  = 2.08 V vs. Fc<sup>+0</sup>, N-methylpyrrolidone), with the active catalyst being the in situ formed Ni(bpy)(CO)<sub>2</sub>.<sup>[148]</sup> Finally, complexes **D**<sup>[152]</sup> and **E**<sup>[150]</sup> catalyse the electroreduction of CO<sub>2</sub> to C<sub>2</sub>O<sub>4</sub><sup>2-</sup>, with the latter being more active (TON up to 55 h<sup>-1</sup>, up to 98% Faradaic Efficiency (FE)). The redox potentials for singly reduced **D** ( $E_{1/2}$  = 2.53 V vs. Fc<sup>+0</sup>, DMF) and **E** ( $E_{1/2}$  = 2.26 to 2.62 V vs. Fc<sup>+0</sup>, DMF) are significantly more negative in comparison to the reduction potentials for **A** and **B**. For **D** and **E**, an outer-sphere electron transfer was proposed to generate transient CO<sub>2</sub> radicals that rapidly couple in solution to yield oxalate salts. Inspired by structural frameworks **D** and **E**, anionic nitrogen-rich ligands coordinated

to nickel were explored for the electrochemical reduction of CO<sub>2</sub>. The bidentate TAPPy ligand (TAPPy = 1,3,5-triazapentadienyl-2,4-bis(2-pyridyl)), as shown for Ni(TAPPy)<sub>2</sub> in **Fig. 4.1**, has a pentadiene core that is structurally comparable to compounds **D** and **E**. Only Cu(TAPPy)<sub>2</sub><sup>[157]</sup> and Pd(TAPPy)<sub>2</sub><sup>[158]</sup> derivatives have been reported to date, and the redox behavior of M(TAPPy)<sub>2</sub> complexes remains unknown.

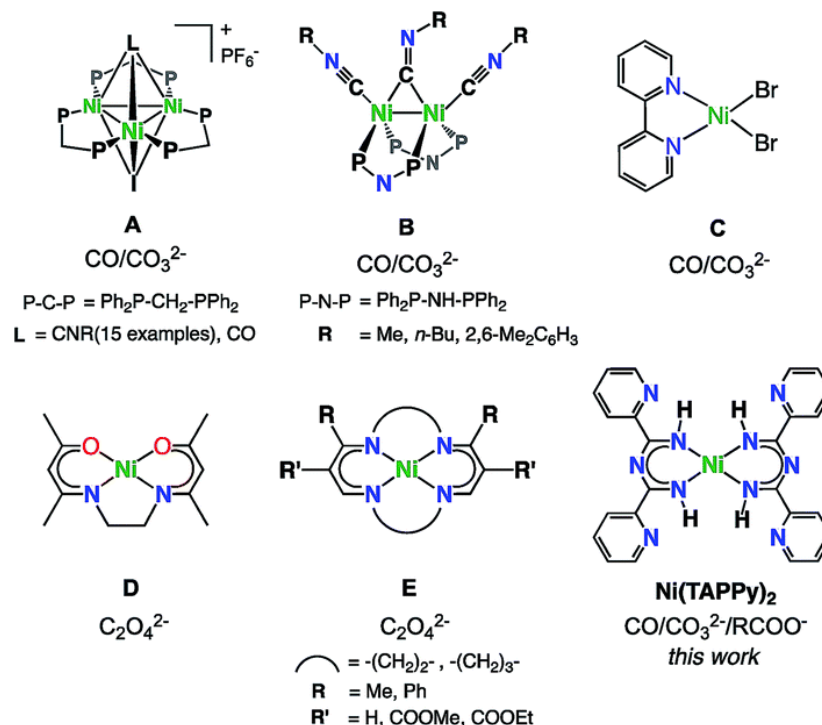
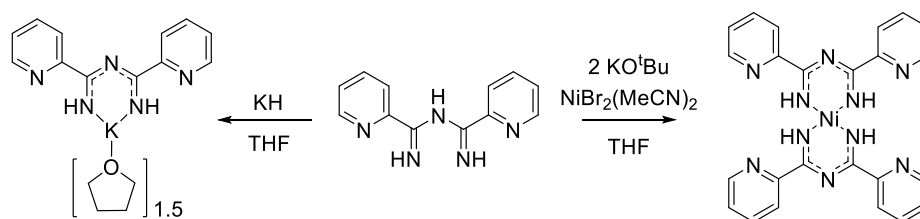


**Figure 4-1** Structural comparison of Ni(TAPPy)<sub>2</sub> with nickel complexes **A–E** capable of catalyzing the electrochemical reduction of CO<sub>2</sub>. Below each structure are the major products formed during electrochemical reduction.

### 4.3 Synthesis and Electrochemical Analysis of Ni(TAPPy)<sub>2</sub>

Ni(TAPPy)<sub>2</sub> was synthesized in 78% yield by deprotonating 2 equiv. HTAPPy in situ with a strong base, followed by addition of NiBr<sub>2</sub>(MeCN)<sub>2</sub> (**Scheme 4.1**). The salt KTAPPy·THF was also independently synthesized by reacting HTAPPy with strong bases, including KO<sup>t</sup>Bu, KHMDS or KH.



**Scheme 4-1** Synthesis of KTAPPy·THF and Ni(TAPPy)<sub>2</sub>.

The cyclic voltammogram (CV) of Ni(TAPPy)<sub>2</sub> under Ar is shown in **Fig. 4.2**. A reversible redox feature appears at  $E_{1/2} = -2.25$  V (all potentials referenced vs.  $\text{Fc}^{+/0}$ ), which corresponds to the generation of a Ni(II) ligand radical species. The linear dependence of

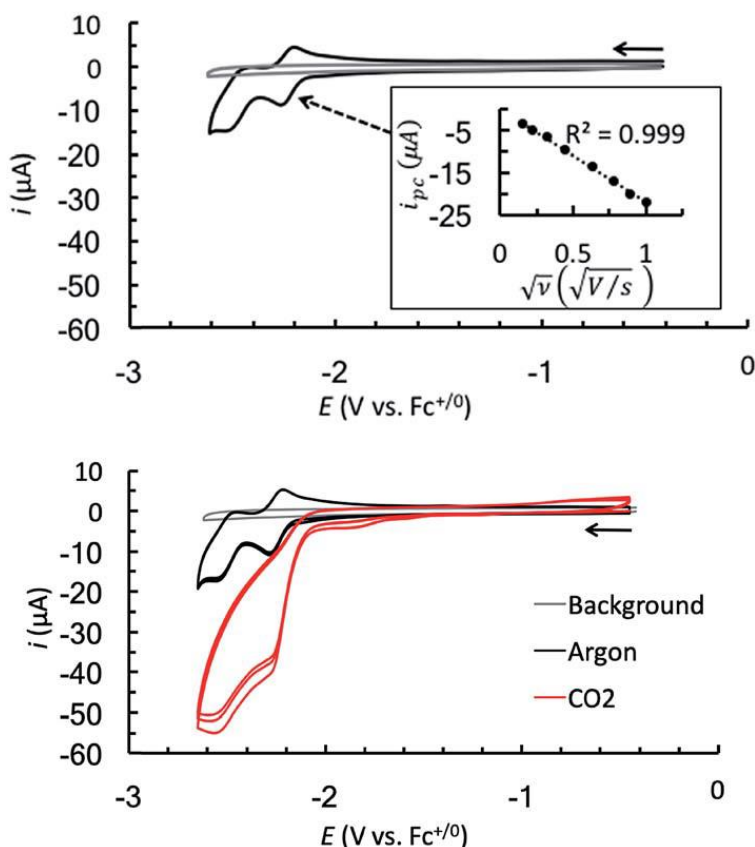


**Figure 4-2** Top: CV of Ni(TAPPy)<sub>2</sub> (0.50 mM) at 0.1 V s<sup>-1</sup> under Ar, with cathodic peak current ( $i_{pc}$ ) versus the square root of scan rate for the one-electron reduction of Ni(TAPPy)<sub>2</sub> under Ar (inset). Bottom: CVs of Ni(TAPPy)<sub>2</sub> (0.50 mM, three consecutive scans) at 0.1 V s<sup>-1</sup> under Ar (black) and CO<sub>2</sub> (red). Conditions: 0.1 M  $n\text{Bu}_4\text{NPF}_6$ , DMF, glassy carbon disk working electrode, Pt wire counter electrode, Ag/AgCl reference electrode. Background scans shown in grey.

the peak current ( $i_{pc}$ ) as a function of the square root of the scan rate for this reduction confirms that  $Ni(TAPPy)_2$  is a freely diffusing species in solution, with a calculated diffusion coefficient ( $D$ ) of  $5.3(4) \times 10^{-6} \text{ cm}^2 \text{ s}^{-1}$  (**Fig. 4.2**, inset). This first redox event is followed by an irreversible reduction at  $E_{pc} = -2.52 \text{ V}$ , which becomes quasi-reversible at faster scan rates.

The CVs of  $Ni(TAPPy)_2$  in anhydrous DMF under  $CO_2$  reveal an approximate 4-fold current enhancement, reaching a maximum at  $-2.50 \text{ V}$  with no significant current loss after multiple scans (**Fig. 4.2**, bottom), indicating  $CO_2$  reduction activity promoted by  $Ni(TAPPy)_2$ . In reported cases where anhydrous  $CO_2$  reduction results in  $CO_3^{2-}$  and/or  $C_2O_4^{2-}$  production, a single-compartment electrochemical cell containing a sacrificial Mg or Al anode was used to precipitate these salts during controlled potential electrolysis (CPE) experiments.<sup>[148,150,159]</sup> We conducted CPE experiments under  $CO_2$  with  $Ni(TAPPy)_2$  at  $-2.50 \text{ V}$  using a Mg rod counter electrode. Similar results are obtained with both Pt mesh and glassy carbon working electrodes: simultaneous decrease in current response and precipitation of an off-white solid over the course of 6 h. The major gaseous products during CPE with  $Ni(TAPPy)_2$  are CO and  $H_2$ .

At the end of CPE experiments with  $Ni(TAPPy)_2$ , the precipitate was isolated and analyzed by attenuated total reflectance (ATR)-IR spectroscopy, allowing the comparison of the solid products with authentic samples of common  $CO_2$  reduction products such as  $MgCO_3$ ,  $Mg(HCOO)_2$ , and  $MgC_2O_4$ . Unfortunately, the observed infrared stretches from  $1700\text{--}1300 \text{ cm}^{-1}$  in the post-CPE sample were mostly broad and ill-defined, making product distribution assessment unclear. The post-CPE sample could also contain multiple carboxylate ( $RCOO^-$ ) and carbamate ( $R_2NCOO^-$ ) ligand degradation fragments,

contributing even further to the poorly resolved IR spectrum. Acidification of the post-CPE solids with excess  $\text{H}_3\text{PO}_4(\text{aq})$  resulted in immediate effervescence, indicating the release of  $\text{CO}_2$  from the electrolysis products. Gas chromatography (GC) analysis of the headspace confirms that  $\text{CO}_2$  is released upon acidification. The acidified solutions yield no detectable amounts of oxalic acid ( $\text{C}_2\text{O}_4\text{H}_2$ ) by  $^{13}\text{C}\{^1\text{H}\}$  NMR spectroscopy, suggesting that  $\text{C}_2\text{O}_4^{2-}$  is either absent or only present in trace quantities.

The CPE data is presented in **Table 4.1**. The gaseous headspace of sealed electrolysis vessels was analyzed by GC at the end of each run, after which the precipitate was isolated and acidified in a sealed reaction vessel. Electrolysis at -2.50 V in the presence of  $\text{Ni}(\text{TAPPy})_2$  (5.0 mmol) generates  $\text{H}_2$  ( $3.58 \pm 1.31$  mmol) and one equiv. of CO ( $5.00 \pm 0.02$  mmol) relative to Ni. A significantly larger amount of  $\text{RCOO}^- / \text{CO}_3^{2-}$  is produced ( $79 \pm 13$  mmol, 16 equiv.) upon post CPE acidification, quantified by measuring the amount  $\text{CO}_2$  released by GC from the isolated precipitate (entry 1).

**Table 4-1** Controlled potential electrolysis (CPE) data<sup>a</sup>

Reagent	Amount ( $\mu\text{mol}$ )	Charge passed (C)	$\mu\text{mol H}_2$	$\mu\text{mol CO}$	$\mu\text{mol RCOO}^-$ / $\text{CO}_3^{2-}$ (as $\text{CO}_2$ )	Faradaic Efficiency (%)
$\text{Ni}(\text{TAPPy})_2$	5.0	$7.6 \pm 0.3$	$3.58 \pm 1.31$	$5.00 \pm 0.02$	$79 \pm 13$	$23 \pm 2$
HTAPPy	5.0	$7.4 \pm 0.6$	$9.28 \pm 2.02$	$0.56 \pm 0.12$	$70 \pm 15$	$27 \pm 3$
KTAPPy•THF	5.0	$2.07 \pm 0.08$	$10.09 \pm 1.61$	$0.23 \pm 0.10$	$35 \pm 8$	$95 \pm 10$

#### 4.4 Infrared Spectroelectrochemistry (IR-SEC)

To determine the fate of Ni during CPE experiments, IR-SEC experiments were performed. In particular, it was of interest to determine whether CO was being sequestered to produce  $\text{Ni}(\text{CO})_m\text{L}_n$  complexes, since this type of decomposition behavior has been

recently observed for Ni-based electrocatalysts.<sup>[148,160–162]</sup> By applying an increasingly negative reduction potential (-2.10 to -2.45 V), new features gradually intensified at 1976, 1963, 1901, and 1870  $\text{cm}^{-1}$ , which was ascribed to Ni–CO stretches from the stepwise decomposition of  $\text{Ni}(\text{TAPPy})_2$  (**Fig. 4.3**, top). To strengthen this claim, IR-SEC electrolysis was repeated at -2.45 V with  $^{13}\text{CO}_2$ . All peaks shifted by 41–49  $\text{cm}^{-1}$ , consistent with the

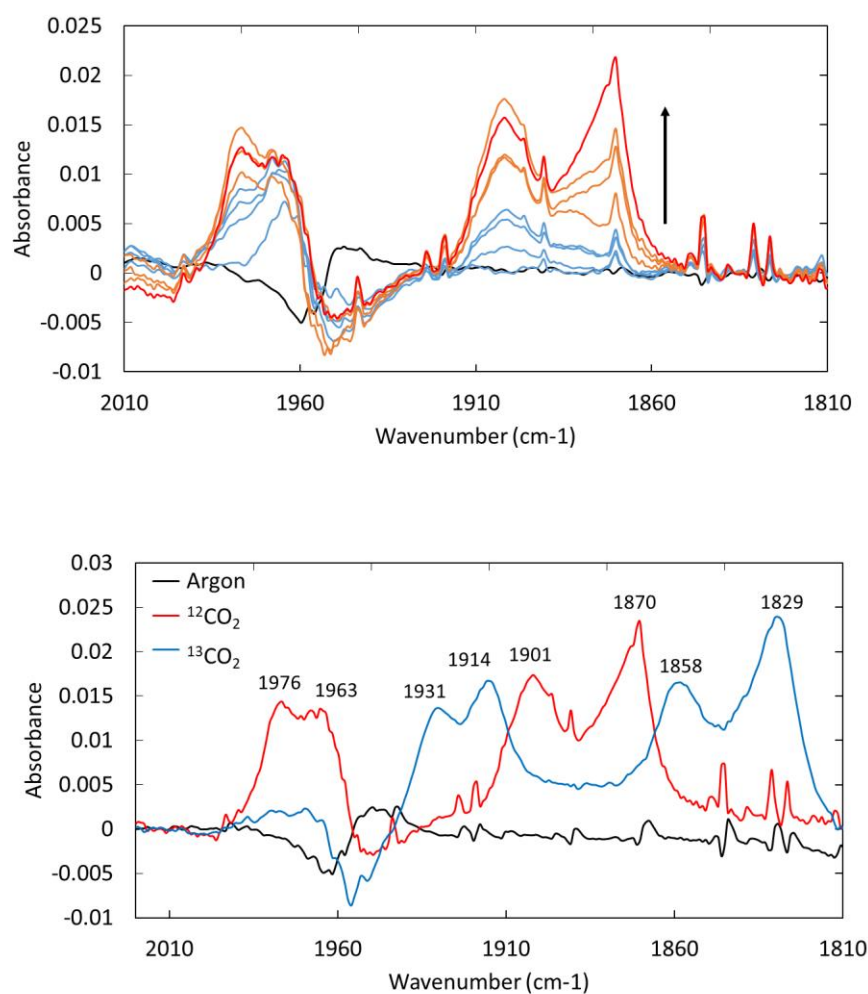


**Figure 4-3** IR-SEC spectra of  $\text{Ni}(\text{TAPPy})_2$  (0.5 mM). Top: Electrolysis from -2.10 to -2.45 V in 0.05 V increments under  $\text{CO}_2$ . Bottom: Electrolysis of  $\text{Ni}(\text{TAPPy})_2$  at -2.45 V under  $^{12}\text{CO}_2$  (red) and  $^{13}\text{CO}_2$  (blue). Conditions: 0.2 M  $n\text{Bu}_4\text{NPF}_6$ , DMF.

expected isotopic shift from the reduced mass calculation ( $43\text{ cm}^{-1}$ ) for a simple harmonic oscillator model (**Fig. 4.3**, bottom).

The vibrational frequencies in the resulting spectra match those reported for  $\text{Ni(CO)}_2\text{L}_2$  complexes, where L is a nitrogen donor.<sup>[163–166]</sup> For example,  $\text{Ni(CO)}_2\text{bpy}$  features an asymmetric/symmetric stretch at  $1860$  and  $1950\text{ cm}^{-1}$  and  $\text{Ni(CO)}_2(\text{py})_2$  has similar stretches with frequencies at  $1903$  and  $1981\text{ cm}^{-1}$ . Vibrational frequencies at  $1897$  and  $1953\text{ cm}^{-1}$ , calculated for zero-valent nickel compound  $[\text{Ni(TAPPy)(CO)}_2]^-$  that could be one of the compounds that is forming at the electrode surface, match well the experimentally observed absorptions.

Due to the expected formation of  $\text{Ni(CO)}_m\text{L}_n$  under reducing conditions, it was postulated that the addition of a CO scavenger would circumvent the catalyst poisoning, leading to increased turnover numbers. The use of  $[\text{Ni(TMC)}]^{2+}$  (TMC = 1,4,8,11-tetramethyl-1,4,8,11-tetraazacyclotetradecane) has been described in the literature. It is known to be inactive towards  $\text{CO}_2$  reduction and only be involved in CO sequestration, leading to increased activity and stability of the parent  $[\text{Ni(cyclam)}]^{2+}$  system towards catalytic electrochemical reduction of  $\text{CO}_2$ .<sup>[161,167]</sup> As a control, spectroelectrochemistry was performed where  $[\text{Ni(TMC)}]^{2+}$  was reduced in the presence of carbon monoxide, leading to nickel-carbonyl containing compounds that originated from  $[\text{Ni(TMC)}]^{2+}$ . Features around  $1950$  and  $1978\text{ cm}^{-1}$  steadily increased in the IR spectra at  $-2.45\text{V}$  vs.  $\text{Fc/Fc}^+$ , without features between  $1800\text{--}1900\text{ cm}^{-1}$  that were apparent when  $\text{Ni(TAPPy)}_2$  was reduced in the presence of  $\text{CO}_2$  (**Figure 4.4**). The addition of a 5-fold excess of  $[\text{Ni(TMC)}]^{2+}$  in the presence of  $\text{Ni(TAPPy)}_2$  at catalytic conditions still appeared to result in decomposition of the parent catalyst, based on the presence of features around  $1870\text{ cm}^{-1}$ .



<sup>1</sup> In the IR spectrum. Controlled potential electrolysis confirmed the inability of  $[\text{Ni}(\text{TMC})]^{2+}$  to mitigate catalyst decomposition, as there was no statistical difference for product formation compared to electrolysis with  $\text{Ni}(\text{TAPPy})_2$  on its own.

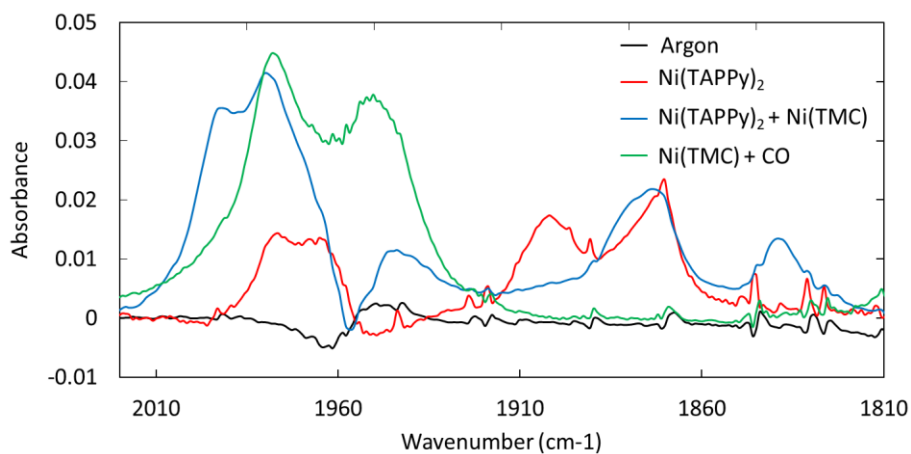
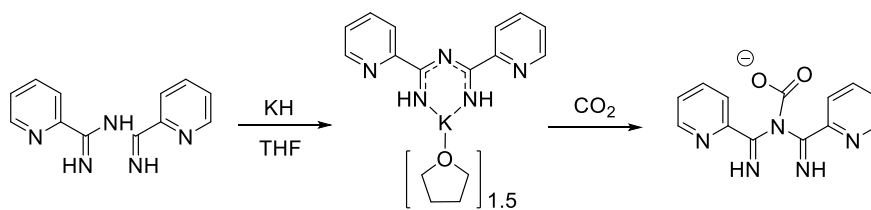


**Figure 4-4** IR-SEC spectra of  $\text{Ni}(\text{TAPPy})_2$  (0.5 mM) at -2.45 V with (blue) and without (red) the addition of 2.5 mM  $[\text{Ni}(\text{TMC})]^{2+}$  under  $\text{CO}_2$ . The green trace corresponds to the IR-SEC spectra of  $[\text{Ni}(\text{TMC})]^{2+}$  at -2.45 V in a  $\text{CO}$  saturated solution. Conditions: 0.2 M  $n\text{Bu}_4\text{NPF}_6$ , DMF.

#### 4.5 Ligand Modification and Reaction with $\text{CO}_2$

Another possibility for the discrepancy between the presence of  $\text{CO}$  in the headspace and the amount of carbonate-containing precipitate, was the potential reaction of the ligand with carbon dioxide with the formation of carbonate-containing products. Although carbamate formation is difficult under standard conditions, these can be accessible through electrochemical synthesis assisted with tetrabutylammonium.<sup>[168–173]</sup> One avenue that was envisioned was the decomposition of the catalyst, followed by reaction of the dissociated ligand with carbon dioxide under reducing conditions (**Scheme 4.2**). To test this hypothesis,  $\text{KTAPPy}$  was prepared, isolated and then exposed to carbon dioxide in solution.



**Scheme 4-2** Potential reactivity of dissociated ligand with carbon dioxide to form carbonate-containing products.

The reaction between KTAPPy and CO<sub>2</sub> was performed under inert atmosphere utilizing Schlenk techniques, however, the resonances in the <sup>1</sup>H and <sup>13</sup>C NMR of the resulting solution closely matched that of HTAPPy and no new products were observed. The initial reaction proceeded quickly and a small amount of precipitate formed after adding CO<sub>2</sub> into the headspace of the gas-tight NMR tube. The precipitate was isolated and characterized by infrared spectroscopy, leading to a spectrum similar to that of the parent HTAPPy, with no identifiable features corresponding to carbonate-containing compounds. Different solvents, including DMSO-d<sub>6</sub> and THF-d<sub>8</sub>, were used for the same reaction in an attempt to identify the reactivity and dissolve the precipitate that was formed in acetonitrile, although in all cases the analysis pointed towards HTAPPy formation from the reaction with CO<sub>2</sub>. Due to the stability of KTAPPy in DMSO, it is expected that small amounts of adventitious water should not be detrimental, and that the reaction was due to the presence of CO<sub>2</sub>. In addition, the carbon dioxide utilized was of high purity, the solvents were dried over molecular sieves or sodium/benzophenone before distillation so it was difficult to rationalize how protonation occurred. Representative spectra are shown in **Figure 4.5** on the conversion of KTAPPy to HTAPPy in THF-d<sub>8</sub>, where the NH resonances integrate for a total of two before the addition of CO<sub>2</sub>, and integrate to three after the addition.

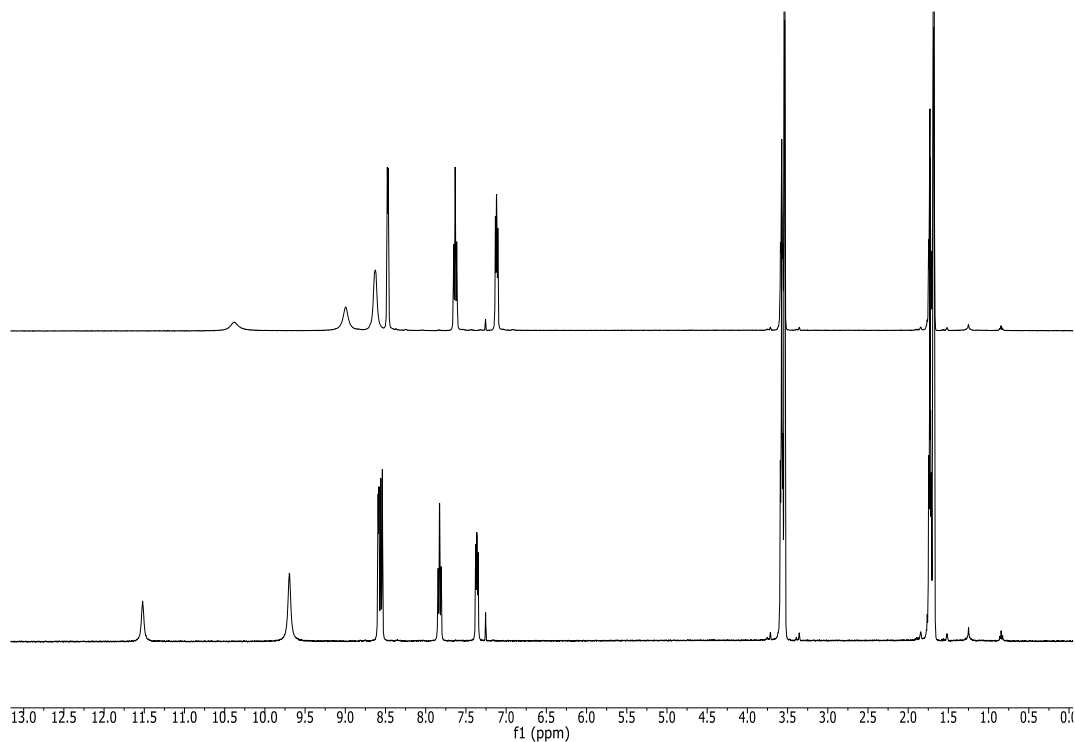
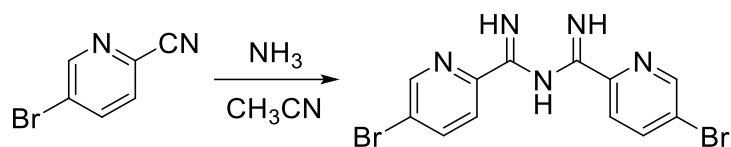


**Figure 4-5**  $^1\text{H}$  NMR spectra for KTAPPy in  $\text{THF-d}^8$  (top) and the reaction mixture between KTAPPy and  $\text{CO}_2$  (bottom).

No concrete conclusions could be drawn from the reaction of  $\text{CO}_2$  with KTAPPy, however it is expected that the discrepancy between the observed CO in the headspace of the vessel with controlled potential electrolysis could be rationalized by the formation of carbonyl-containing nickel compounds in addition to possible reactivity of the dissociated ligand with  $\text{CO}_2$ , causing additional carbonate-containing precipitate under CPE.

Parallel to the work on  $\text{Ni}(\text{TAPPy})_2$ , ligand modification was targeted in order to lower the overpotential and provide avenues for further functionalization towards secondary sphere effects. The targeted modification of the proligand incorporated a bromide on each pyridine group that could be used in subsequent coupling reactions or impart slight variations on the electronic properties of the the parent  $\text{Ni}(\text{TAPPy})_2$ . The synthetic procedure was similar to that employed for HTAPPy,<sup>[174]</sup> where 5-bromo-2-

pyridinecarbonitrile was heated under a headspace of ammonia in acetonitrile (**Scheme 4.3**). Single crystals were grown by slow evaporation of a concentrated solution of TAPPy-Br in acetonitrile and the identity of the compound was confirmed by X-Ray crystallography. Hydrogen bonding is present between the imine protons and the pyridyl nitrogens, facilitating a planar framework favorable to  $\pi$  delocalization, similar to that of free HTAPPy and  $\text{Ni}(\text{TAPPy})_2$  (**Figure 4.6**).<sup>[144,175]</sup> The resonances corresponding to the imine protons in the  $^1\text{H}$  NMR spectrum are significantly deshielded ( $\delta$  9.51,  $\text{CD}_3\text{CN}$ ), indicating that the hydrogen bonding is maintained in solution.



**Scheme 4-3** Synthesis of TAPPy-Br

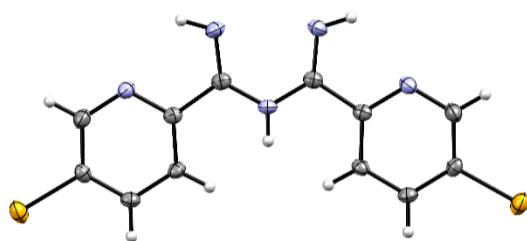


**Figure 4-6** Solid-state structure of TAPPy-Br with 50% probability ellipsoids.

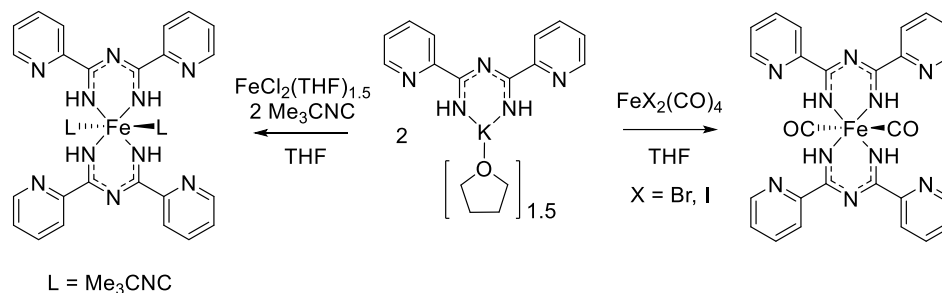
In summary, the synthesis of new nickel complexes containing the bidentate TAPPy ligand (TAPPy = 1,3,5-triazapentadienyl-2,4-bis(2-pyridyl)) has been accomplished. The neutral complex  $\text{Ni}(\text{TAPPy})_2$  can be reduced by one electron, with the resulting anion being best described as a redox non-innocent  $\text{Ni}(\text{II})$  complex with a radical delocalized almost exclusively onto the ligand framework. Under Ar,  $\text{Ni}(\text{TAPPy})_2$  can be electrochemically reduced by up to two electrons in anhydrous DMF, and current

enhancement is observed when the complex is exposed to CO<sub>2</sub>. The observed current enhancement is not due to the electrocatalytic reduction of CO<sub>2</sub>; instead, the complex reduces CO<sub>2</sub> into carbonyl-containing nickel complexes and insoluble carboxylated ligand byproducts. Although ligands often serve as electron reservoirs during electrocatalysis, the exclusive ligand-based redox activity of Ni(TAPPy)<sub>2</sub> suggests that the localization of the LUMO/SOMO exclusively on the ligand is generally unfavorable for electrocatalytic CO<sub>2</sub> reduction.

#### 4.6 Iron-based TAPPy complexes

The corresponding iron-TAPPy complex was also pursued as a potential candidate for CO<sub>2</sub> reduction, as iron based CO<sub>2</sub> electrocatalysts are much less likely to decompose into carbonyl containing compounds. The structure of two different iron coordination complexes with TAPPy had been previously published, however, the chemistry of iron complexes with the TAPPy ligand remains unknown.<sup>[175]</sup> Initial work targeted an Fe<sup>II</sup>(TAPPy)<sub>2</sub>L<sub>2</sub> framework, in order to provide an open coordination site after L dissociation for nucleophilic attack towards CO<sub>2</sub> under catalytic conditions. This desired framework was based on the stability and activity of the iron porphyrin systems, which are expected to undergo halide dissociation upon reduction and generate a planar iron complex as the active catalyst in solution.<sup>[119,124,125,127]</sup> Because the iron(II) complex was expected to be susceptible to oxidation, the targeted non-innocent ligands, L, were capable of accepting electron density through back donation from the metal. This would also enable an initial reduction at a lower overpotential to generate a formally Fe(0) active catalyst. Previously reported iron piano-stool electrocatalysts have utilized carbonyl ligands that dissociate prior to CO<sub>2</sub> activation, and the so Fe<sup>II</sup>(TAPPy)<sub>2</sub>(CO)<sub>2</sub> framework was

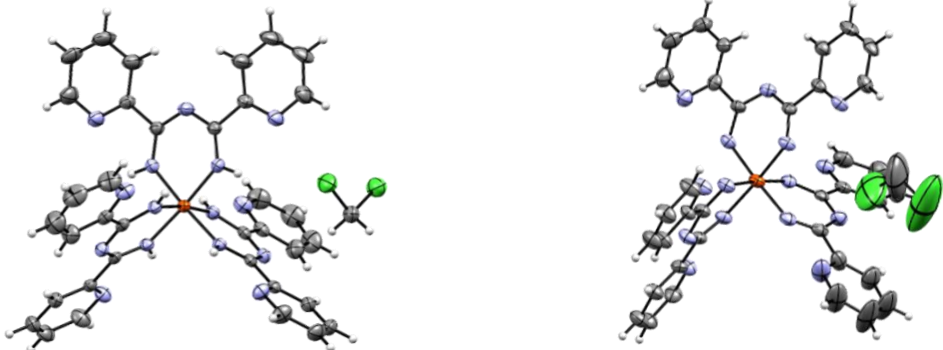
targeted.<sup>[176–178]</sup>  $\text{Fe}(\text{CO})_4\text{Br}_2$  and  $\text{Fe}(\text{CO})_4\text{I}_2$  were prepared following literature procedures<sup>[179,180]</sup> in order to circumvent the need for a carbon monoxide atmosphere during complexation, and freshly prepared KTAPPy was added to the corresponding  $\text{Fe}^{\text{II}}$  source for the salt metathesis reaction (**Scheme 4.4**).



**Scheme 4-4** Attempted synthesis of  $\text{Fe}^{\text{II}}(\text{TAPPy})_2\text{L}_2$

Large scale reactions were handled under air and moisture free conditions utilizing Schlenk techniques with a swivel-frit apparatus, and small scale vial reactions were conducted in an argon atmosphere glovebox with freshly sublimed or commercial iron sources. Single crystals suitable for X-Ray crystallography were only obtained when the crystals were grown by layering concentrated solutions of the complex in DCM with pentane. This succeeded both inside and outside the glovebox, resulting in the precipitation of an orange/red solid. However, even when crystallization attempts were conducted in a glove box, the resultant solid state structure always revealed an octahedral homoleptic  $\text{Fe}(\text{TAPPy})_3$  coordination environment, indicative of an iron(III) metal center. Different starting materials were utilized in order to try and obtain the target  $\text{Fe}^{\text{II}}(\text{TAPPy})_2\text{L}_2$  including  $\text{FeBr}_2$ ,  $\text{Fe}_2\text{Cl}_4(\text{THF})_3$ ,  $\text{Fe}(\text{OAc})_2$ , and  $\text{Fe}(\text{HMDS})_2$  with isocyanates as capping ligands in addition to the carbonyl compounds. In all instances the  $\text{Fe}^{\text{III}}(\text{TAPPy})_3$  complex was obtained upon warming the reaction solutions and recrystallizing from a DCM/pentane

mixture. It is worth noting that the recrystallization was low yielding, and uncharacterized black precipitate was always observed and filtered off. When anhydrous  $\text{FeCl}_3$  was used in lieu of an iron(II) source, the solid state structure featured a lower symmetry space group and a slightly different unit cell, although all of the structural parameters are within error and are indicative of the same complex (**Figure 4.7**).<sup>[175]</sup>



Unit Cell Dimensions	Literature Value	Monoclinic C	Triclinic
Length a (Å)	20.3755(7)	20.4049(5)	10.4512(6)
Length b (Å)	17.1148(5)	17.1474(4)	12.6572(9)
Length c (Å)	11.5256(4)	11.5359(3)	16.9668(14)
Angle alpha (°)	90	90	75.369(5)
Angle beta (°)	112.336(2)	112.2950(10)	82.844(5)
Angle gamma (°)	90	90	66.394(3)

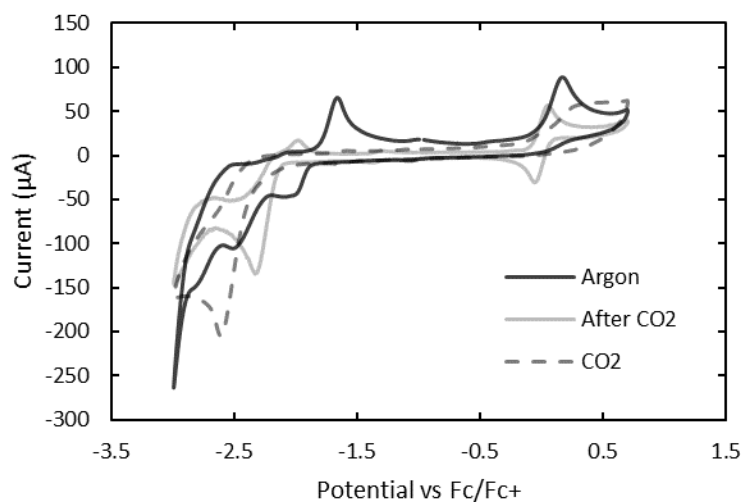
  

Selected Bond Lengths	Literature Value	Monoclinic C	Triclinic
N-Fe (Å)	1.921(2) – 1.927(2)	1.925(2)-1.930(2)	1.915(3) – 1.945(3)
N1-C1 (Å)	1.302(3)	1.305(3)	1.298(6)
C1-N3 (Å)	1.342(3)	1.342(3)	1.355(6)

**Figure 4-7** Solid state structures of  $\text{Fe}(\text{TAPPy})_3$  from reactions using an iron(III) source (left, Monoclinic C) and an iron (II) source (right, Triclinic) shown with 50% probability ellipsoids.<sup>[175]</sup>

When the  $\text{Fe}^{\text{II}}(\text{TAPPy})_2\text{L}_2$  complex, ( $\text{L} = \text{'BuNC}$ ), was synthesized at  $-78\text{ }^\circ\text{C}$  and maintained under  $0\text{ }^\circ\text{C}$  while volatiles were removed under vacuum, a dark green solid was obtained, in contrast to the orange/red product isolated after crystallization from a DCM/pentane solution. This crude product was NMR silent and did not afford single

crystals upon multiple attempts in a glovebox freezer. A preliminary voltammogram obtained under argon (**Figure 4.8.**) should be interpreted with caution due to a lack of clear characterization. Three irreversible reduction waves appear to be present, which could be related to the formal  $\text{Fe}^{\text{III}}/\text{Fe}^{\text{II}}$ ,  $\text{Fe}^{\text{II}}/\text{Fe}^{\text{I}}$ , and  $\text{Fe}^{\text{I}}/\text{Fe}^0$  redox couples. When the solution was exposed to carbon dioxide, the electrochemical behavior changed dramatically and was supplemented with a color change of the solution to colorless. The resulting voltammogram lost multiple redox features under a  $\text{CO}_2$  atmosphere, and these did not return after placing the solution under an argon atmosphere post  $\text{CO}_2$  exposure. The redox couple at 0V in the grey trace is due to a ferrocene internal standard and is not relevant to the complex. The resulting voltammogram is relatively free of other features, and relates closely with that of HTAPPy (**Figure 4.9**).



**Figure 4-8** Cyclic voltammogram of potential  $\text{Fe}(\text{TAPPy})_2(\text{CO})_2$  (1.0 mM) at  $0.1 \text{ V s}^{-1}$  under Ar (black),  $\text{CO}_2$  (Dashed line) and Ar after exposure to  $\text{CO}_2$  (grey) . Conditions: 0.1 M  $^n\text{Bu}_4\text{NPF}_6$ , DMF, glassy carbon disk working electrode, Pt wire counter electrode, Ag/AgCl reference electrode.



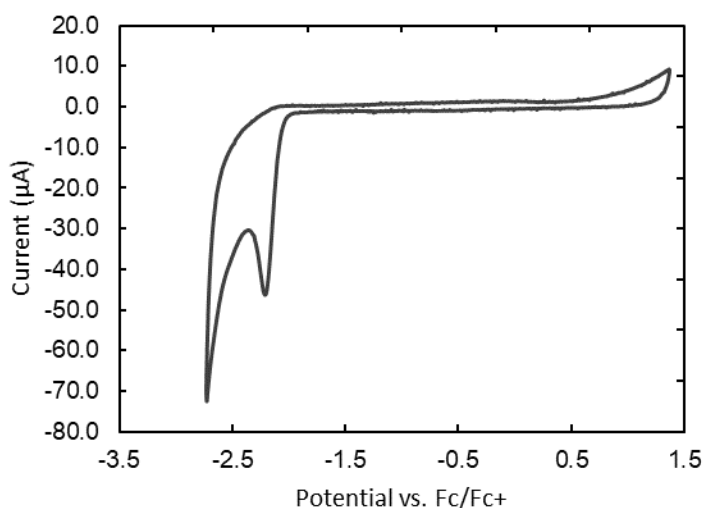
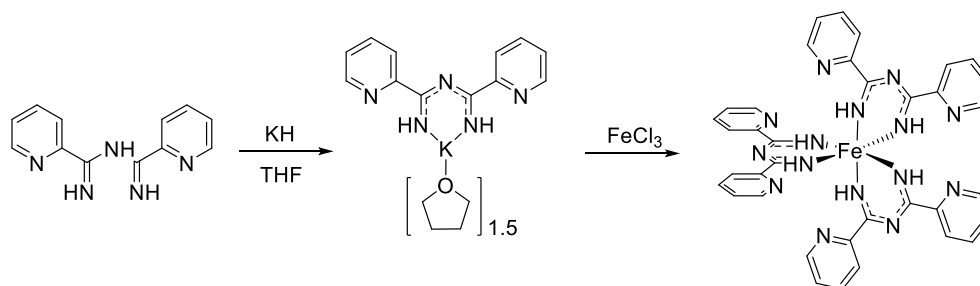


**Figure 4-9** Cyclic voltammogram of HTAPPy (1.0 mM) at 0.1 V s<sup>-1</sup> under Ar. Conditions: 0.1 M <sup>n</sup>Bu<sub>4</sub>NPF<sub>6</sub>, DMF, glassy carbon disk working electrode, Pt wire counter electrode, Ag/AgCl reference electrode.

Due to the difficulty in isolating the corresponding iron(II) complex and its potential irreversible reaction with CO<sub>2</sub>, the homoleptic Fe(TAPPy)<sub>3</sub> was synthesized from FeCl<sub>3</sub> and three equivalents of freshly prepared KTAPPy (**Scheme 4.5**).



**Scheme 4-5** Synthesis of Fe(TAPPy)<sub>3</sub>

The iron complex was purified by crystallization, through layering pentane on a concentrated solution of Fe(TAPPy)<sub>3</sub> in DCM. The magnetic moment of the complex is 2.4 μ<sub>B</sub>, in agreement with a low spin iron(III) complex with one unpaired electron.<sup>[181,182]</sup> Its cyclic voltammogram (**Figure 4.10**) did not show any current enhancement under an

atmosphere of CO<sub>2</sub>. Subtle reduction waves were observed, with the main electrochemical feature being an irreversible oxidation around 0.5V vs. Fc/Fc<sup>+</sup>. Because of the poor catalytic activity of Ni(TAPPy)<sub>2</sub> and a negative initial screen for Fe(TAPPy)<sub>3</sub> under CO<sub>2</sub>, optimization of the reaction conditions was not pursued.

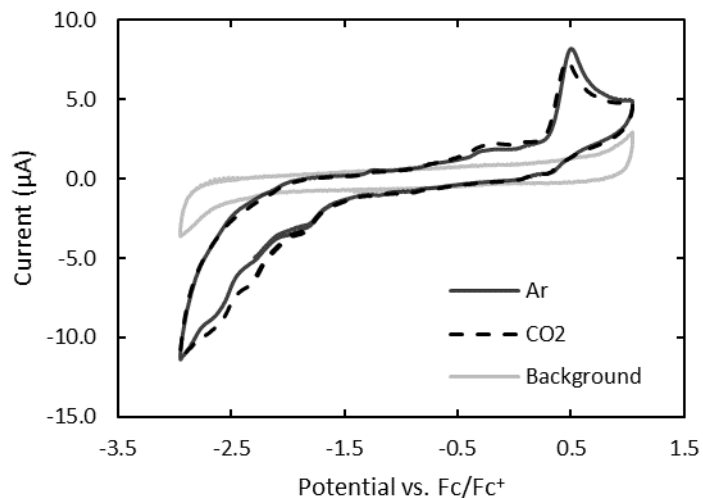


**Figure 4-10** Cyclic voltammogram of Fe(TAPPy)<sub>3</sub> (1.0 mM) at 0.1 V s<sup>-1</sup> under Ar (black) and CO<sub>2</sub> (Dashed line). Conditions: 0.1 M <sup>n</sup>Bu<sub>4</sub>NPF<sub>6</sub>, DMF, glassy carbon disk working electrode, Pt wire counter electrode, Ag/AgCl reference electrode. Background scan shown in grey.

Overall, the pursuit of an iron-based CO<sub>2</sub> electrocatalyst as an alternative to Ni(TAPPy)<sub>2</sub> was unsuccessful. Initial work targeted the synthesis of an Fe(TAPPy)<sub>2</sub>L<sub>2</sub> complex with  $\pi$ -acidic L type ligands. The Fe(TAPPy)<sub>2</sub>L<sub>2</sub> complex showed a propensity for the formation of a homoleptic Fe(TAPPy)<sub>3</sub> complex upon crystallization in DCM, as well as electrochemical instability under an atmosphere of carbon dioxide. The homoleptic Fe(TAPPy)<sub>3</sub> complex was then isolated and tested for catalytic activity. A negative screen was obtained under aprotic conditions, and optimization was not undertaken.

## 4.7 Experimental

Spectroelectrochemistry experiments were conducted using a LabOmak IR-SEC cell fitted with CaF<sub>2</sub> windows, platinum working/counter electrodes and a Ag wire pseudoreference electrode that was referenced to an external sample of Fc<sup>+0</sup> (0 V). The optical path length of the cell is 0.2 mm. The cell was filled with DMF solutions (ca. 0.1 mL) containing 0.2 M <sup>n</sup>Bu<sub>4</sub>NPF<sub>6</sub>, and analyte. The solutions were sparged with Ar in a scintillation vial for ten minutes prior to use, and experiments under CO<sub>2</sub> were then sparged for 10 seconds with CO<sub>2</sub> before injection into the IR cell. Blank DMF solutions with 0.2 M <sup>n</sup>Bu<sub>4</sub>NPF<sub>6</sub> were used to obtain baseline corrected spectra at each voltage step.

**KTAPPy·THF.** To a 50mL round-bottom flask, HTAPPy (0.502g, 0.002 mol) and a PTFE-coated stir bar were added. The flask was connected to a swivel-frit apparatus and placed under vacuum. Anhydrous THF (35mL) was vacuum transferred into the flask and the vessel was placed under argon. After all solids were dissolved, the solution was cooled to -78 °C and KH was added in one portion (0.170 g, 0.004 mol). The reaction mixture was stirred cold for 30 min, then slowly warmed up to room temperature. After stirring for an additional 1 h, the mixture was filtered and the volatiles were removed under high vacuum. The filtrate was triturated with pentane (15 mL), isolated on a medium-pore glass frit, and dried under high vacuum to yield KTAPPy·THF as a white solid (0.761 g). KTAPPy·THF gradually loses THF under vacuum or after prolonged periods of time under argon. Crystals suitable for X-ray diffraction were grown from a saturated THF solution of KTAPPy·THF in a glove box freezer at -40 °C overnight. <sup>1</sup>H NMR (500 MHz; CD<sub>3</sub>CN, 25 °C): δ 8.38–8.71 (4H, m, 2Ar-H), 7.56–7.95 (2H, m, Ar-H), 7.27 (2H, ddd, d, <sup>3</sup>J<sub>HH</sub> = 7.4 Hz, <sup>3</sup>J<sub>HH</sub> = 4.7 Hz, <sup>4</sup>J<sub>HH</sub> = 1.4 Hz, Ar-H), 3.64 (2H, m, THF), 1.80 (2H, m, THF). The ligand N–H

resonances could not be located.  $^{13}\text{C}\{^1\text{H}\}$  NMR (101 MHz;  $\text{CD}_3\text{CN}$ , 25 °C):  $\delta$  26.28 (THF), 68.32 (THF), 118.3 (Ar-C), 123.0 (Ar-C<sub>quat</sub>), 123.8 (Ar-C), 137.3 (Ar-C), 149.0 (Ar-C), 169.4 (NCNH). Anal. calcd for  $\text{C}_{16}\text{H}_{18}\text{N}_5\text{OK}$ : C, 57.29; H, 5.41; N, 20.88. Found: C, 56.00; H, 5.41; N, 20.42.

**Ni(TAPPy)<sub>2</sub>**. In an argon-filled glove box, a 25 mL schlenk flask equipped with a threaded PTFE cap was charged with a PTFE coated stir bar, **HTAPPy** (200 mg, 0.888 mmol), and KO<sup>t</sup>Bu (100 mg, 0.888 mmol). The solids were dissolved in 8 mL THF and stirred vigorously for 5 minutes, turning pale yellow-brown and generating K(TAPPy) *in situ*. Freshly prepared NiBr<sub>2</sub>(MeCN)<sub>2</sub> (133 mg, 0.44 mmol) was then added to the solution in one portion, followed by an additional 2 mL THF. The solution was sealed, removed from the glove box, and vigorously stirred at 60 °C for 6 h. The resultant orange suspension was cooled to room temperature and worked up under air. The mixture was diluted with THF (250 mL), yielding an opaque orange solution which was filtered through a pad of Celite. The clear orange filtrate was dried under reduced pressure, suspended in 100 mL pentane, and isolated on a medium-pore glass frit. The air and moisture stable product was dried under high vacuum for several hours to yield bright orange **Ni(TAPPy)<sub>2</sub>** (177 mg, 78%), which is sparingly soluble in THF,  $\text{CH}_2\text{Cl}_2$ ,  $\text{CHCl}_3$ , DMF, DMSO and insoluble in MeCN. Single crystals suitable for X-ray diffraction were grown by slow evaporation of  $\text{CH}_2\text{Cl}_2$  from a saturated solution of **Ni(TAPPy)<sub>2</sub>**. Anal. calcd for  $\text{C}_{24}\text{H}_{20}\text{N}_{10}\text{Ni}$ : C, 56.84; H, 3.97; N, 27.62. Found: C, 56.82; H, 4.38; N, 26.14.  $^1\text{H}$  NMR (500 MHz;  $\text{CDCl}_3$ ; 25 °C):  $\delta$  8.70 (2H, m, CHAr), 8.61 (2H, d,  $^3J_{\text{HH}} = 7.8$  Hz, CHAr), 7.84 (2H, m, CHAr), 7.78 (2H, br s, NH), 7.40 (2H, m, CHAr).  $^{13}\text{C}\{^1\text{H}\}$  NMR (126 MHz;  $\text{CDCl}_3$ , 25 °C): 160.89 (C<sub>quat</sub>), 152.00 (C<sub>quat</sub>), 148.64 (CHAr), 137.15 (CHAr), 124.74 (CHAr), 121.50 (CHAr). MS (ESI HRMS):

$m/z$  calc. for  $[C_{24}H_{21}N_{10}Ni]^+$ : 507.1304. Found: 507.1294. IR (KBr,  $cm^{-1}$ ): 3278 (w), 3243 (m), 1550 (m), 1433 (s).

**KTAPPy** +  $CO_2$ . 20mg of freshly prepared **KTAPPy**·THF was placed into a gas-tight NMR tube with a PTFE-coated screw cap in an argon filled glovebox. Anhydrous THF- $d_8$  was added to the sample and sealed. The  $^1H$  and  $^{13}C$  NMR spectra were taken under the initial argon atmosphere to ensure sample integrity. After the spectra were obtained, the solution was degassed by freeze-pump-thaw cycling on a Schlenk line. The solution was then warmed to room temperature before addition of an atmosphere of anhydrous  $CO_2$  *via* Schlenk techniques.  $^1H$  NMR (400 MHz, THF- $d_8$ )  $\delta$  11.60 (s, 1H), 9.78 (s, 2H), 8.65 (dd, 4H), 7.91 (td, 2H), 7.53 – 7.38 (m, 2H).  $^{13}C$  NMR (101 MHz, THF- $d_8$ )  $\delta$  164.72, 152.58, 148.40, 136.70, 124.88 ( $CO_2$ ), 124.77, 121.67.

**TAPPy-Br**. To a 100 mL thick-walled round-bottom flask equipped with a PTFE-coated screw cap was added a magnetic stir bar, 5-bromo-2-pyridinecarbonitrile (2.503 g, 13.7mmol) and 25 mL of acetonitrile. The suspension was sparged with ammonia for 10 minutes, then sealed under a headspace of ammonia gas and heated to 110 °C for 72 hours. After the reaction was complete, the reaction vessel remained sealed and was cooled to -20 °C to precipitate **TAPPy-Br** as a colorless solid. The suspension was filtered on a medium-pore glass frit, washed with 5 mL of pentane and dried in air to afford **TAPPy-Br** (0.520 g, 1.4mmol, 20% yield) as a colorless solid. Single crystals suitable for X-ray diffraction were grown by slow evaporation from a saturated acetonitrile solution of **TAPPy-Br**.  $^1H$  NMR (400 MHz,  $CD_3CN$ )  $\delta$  11.31 (s, 1H), 9.51 (s, 2H), 8.76 (d, 2H), 8.49 (d, 2H), 8.12 (dd, Hz, 2H).  $^{13}C$  NMR (101 MHz,  $CD_3CN$ )  $\delta$  164.32, 150.57, 149.80, 140.08, 123.53, 122.71.

**Fe(TAPPy)<sub>2</sub>(CO)<sub>2</sub>** A 100 mL two-neck round bottom flask was charged with a magnetic stir bar and freshly prepared KTAPPy·THF (100mg, 0.334mmol). The flask was attached to a swivel-frit apparatus and placed under vacuum before transferring 20 mL of anhydrous THF. The solution was placed under argon and cooled to -78 °C, then Fe(CO)<sub>4</sub>I<sub>2</sub> (70mg, 166mmol) was added in one portion through the side arm under a heavy flow of argon. The solution was stirred at -78 °C for 1 hour before warming to room temperature, then stirred at room temperature overnight before filtration through the swivel frit apparatus and evaporation of the filtrate to dryness under reduced pressure. Pentane was condensed onto the resulting solid and the suspension was sonicated before filtering back through the swivel frit to afford **Fe(TAPPy)<sub>2</sub>(CO)<sub>2</sub>** as an opaque solid.

**Fe(TAPPy)<sub>3</sub>**. A 100 mL two-neck round bottom flask was charged with a magnetic stir bar and HTAPPy (414mg, 1.8mmol). The flask was attached to a swivel-frit apparatus and placed under vacuum before transferring 20 mL of anhydrous THF. The solution was placed under argon and cooled to -78 °C, then KHMDS (367mg, 1.8mmol) was added in one portion through the side arm under a heavy flow of argon. The solution was stirred at -78 °C for 1 hour before warming to room temperature, then stirred for an additional hour before the addition of anhydrous FeCl<sub>3</sub> (88 mg, 0.55mmol) in one portion through the side arm under a heavy flow of argon. The reaction mixture was stirred at room temperature overnight, then filtered through a glass frit under inert atmosphere. The filtrate was evaporated to dryness under reduced pressure affording an opaque solid. Pentane was condensed onto the resulting solid and the suspension was sonicated before filtering back through a medium pore glass frit to afford **Fe(TAPPy)<sub>3</sub>** as an opaque solid. Single crystals suitable for X-ray diffraction were grown by layering pentane on a concentrated solution

of **Fe(TAPPy)<sub>3</sub>** in DCM. Large scale recrystallizations proceeded under similar conditions utilizing scintillation vials to afford **Fe(TAPPy)<sub>3</sub>(CH<sub>2</sub>Cl<sub>2</sub>)** as a red, crystalline solid. MS (ESI HRMS): *m/z* calc. for [C<sub>36</sub>H<sub>31</sub>N<sub>15</sub>Fe]<sup>+</sup>: 729.2231. Found: 729.2232. Magnetic moment: 2.4 μ<sub>B</sub>.

## Chapter 5 – Bis(N-heterocyclic carbene) macrocycles and porphyrinids

### 5.1 Background Information

A major class of homogeneous single-site catalysts for the electrochemical reduction of CO<sub>2</sub> is based on porphyrin scaffolds. Initially discovered in 1977, the identified iron and cobalt porphyrin catalysts had relatively low productivity and selectivity but have been substantially improved in the last few decades.<sup>[110,111]</sup> Major breakthroughs included the use of Lewis and Bronsted acids,<sup>[124,125]</sup> incorporating electron withdrawing groups<sup>[133,134]</sup> and exploiting secondary sphere effects through the use of local proton-concentration<sup>[126–128]</sup> or coulombic interactions.<sup>[135]</sup> The stability of the resulting complexes is impressive, with examples reaching turnover numbers of  $\sim 10^6$  with no visible sign of degradation<sup>[126]</sup> or negligible degradation over 3.5 days of electrolysis.<sup>[135]</sup> In addition to iron-based homogenous systems, porphyrin complexes based on cobalt,<sup>[183–185]</sup> copper<sup>[186]</sup> and zinc<sup>[187]</sup> have been used in heterogenous CO<sub>2</sub> reduction, as molecular catalysts supported on carbon-based electrodes. However, the activity of the produced catalysts still needs to be increased in order to meet industrial requirements.<sup>[188,189]</sup>

The use of carbenes as strong sigma donors in ligand frameworks is prevalent for group 7 and 10 molecular catalysts, increasing the electron density at the metal center for nucleophilic attack onto the CO<sub>2</sub> molecule. The use of bidentate,<sup>[138,190]</sup> tridentate<sup>[191–193]</sup> and tetradentate<sup>[194–196]</sup> ligands incorporating carbenes have been used for electrochemical CO<sub>2</sub> reduction, with selected examples shown in **Figure 5.1**. The use of a bidentate biscarbene in complex **A** as a bipyridine derivative led to the highest reported activity on a manganese based catalyst with a TOF<sub>max</sub> of  $3.2 \times 10^5 \text{ s}^{-1}$  due to increased electron density at the metal.<sup>[138]</sup> The corresponding palladium pincer complex **D** provided a redox-active



framework in comparison to phosphine based pincers, reducing dimerization after reduction, albeit with relatively low FE for CO<sub>2</sub> reduction (28%).<sup>[193,197]</sup> A follow-up study on group 10 CNC complexes for CO<sub>2</sub> reduction screened different derivatives of the framework **B** and concluded that the precious metals (Pt and Pd) were better suited for the tridentate ligand with FE up to 47%, while Ni remained under 5%.<sup>[198]</sup> However, tetradentate systems are more common with nickel, and have been used in both electrochemical and photoredox catalysis for CO<sub>2</sub> reduction. Complex **C** is one example that has been used in photoredox catalysis, with the use of N-heterocyclic carbenes and isoquinoline donors to achieve TONs up to 98,000 and a TOF of 3.9 s<sup>-1</sup>, with no detectable dihydrogen formation.<sup>[195]</sup>

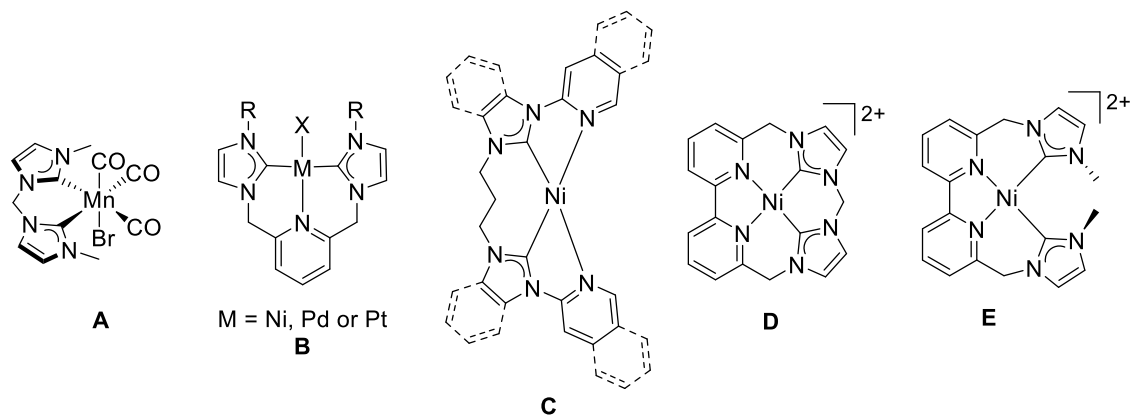


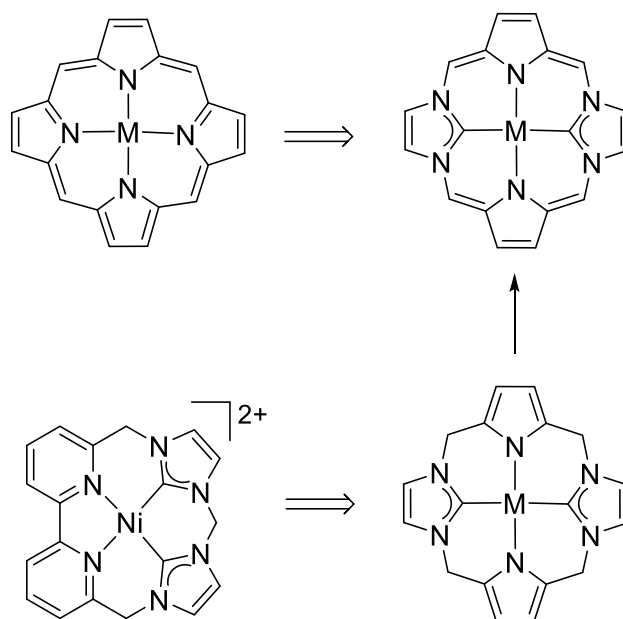
**Figure 5-1** Selected carbene-based catalysts for the electrochemical reduction of CO<sub>2</sub>

Another design consideration is the choice of either an open chain or macrocyclic ligand framework. The electrochemical analysis of **D** and **E** as molecular catalysts for CO<sub>2</sub> reduction enabled a comparison between the rigidity of the complex and selectivity towards reducing CO<sub>2</sub> over dihydrogen production. Complex **D** produced carbon monoxide with 87% faradaic efficiency, compared to **E** that had 5% FE towards CO production and 93% of the remaining FE associated with proton reduction. Both complexes showed no sign of

degradation, with the use of carbenes and redox active ligands able to prevent  $\text{Ni(CO)}_4$  formation.<sup>[196]</sup> This result is supported by the wide range of macrocyclic ligands used for  $\text{CO}_2$  reduction, with untethered open chain systems less common with group 8-10 metal centers.<sup>[103,143]</sup>

## 5.2 Unconjugated Macrocyclic Biscarbene ligands

Two separate ligands were envisioned with the aforementioned properties in mind. Tetradentate, macrocyclic, redox active ligands suitable to iron, cobalt and nickel were favored for metal sustainability purposes. Two ligand frameworks were targeted, both showing several similarities with known complexes having recognized catalytic proficiency in the electroreduction of carbon dioxide (**Scheme 4.1**). The two targets only differ by saturation/unsaturation of the methylene groups and utilize the same precursor for synthesis.

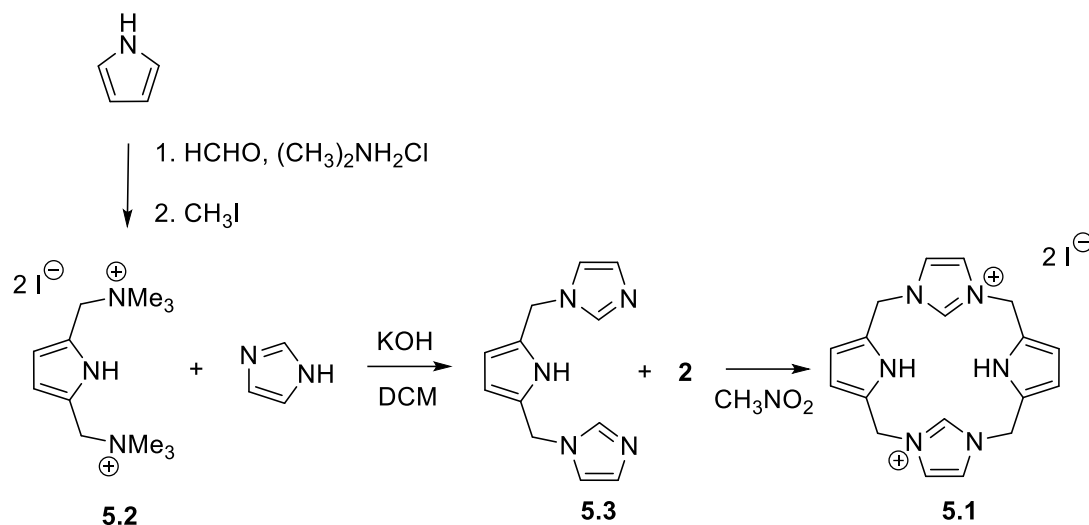


**Scheme 5-1** Proposed catalyst platforms (right) based on known catalysts incorporating porphyrin and pyridine-based macrocycles (left)

In 2002, the Youngs group published the corresponding carbene proligand **5.1**, which was synthesized from readily available starting materials *via* a straightforward pathway.<sup>[199]</sup> No metal coordination complexes have been reported, although analogs having pyridine donors instead of pyrrole are established.<sup>[200–203]</sup>

Initial work targeted coordination complexes with proligand **5.1**, where the compound was synthesized *via* literature reported procedures (**Scheme 5.2**).<sup>[199,204]</sup> The 2,5-substitution of pyrrole proceeds readily with formaldehyde and dimethylammonium chloride and the colorless, liquid product can be purified by distillation. However, the following alkylation with methyl iodide to form the ammonium salt **5.2** always resulted in an impure compound. Multiple attempts at purification or alterations of reaction conditions did not afford the ammonium salt with higher purity, so the reagent was used in further reactions as a crude mixture. As a consequence, subsequent reactions had a reduced yield, although working in gram quantities and purifying the end products enabled progress. The alkylation of imidazole affords a neutral intermediate **5.3**, followed by proligand **5.1** in 26% yield. The <sup>1</sup>H NMR spectrum of intermediate **5.3** shows two separate resonances for the chemically inequivalent positions on the imidazole backbone, as expected for a time averaged C<sub>2v</sub> symmetry. After macrocycle formation, there is only one resonance in the <sup>1</sup>H NMR spectrum for the imidazole backbone, consistent with a symmetry change to D<sub>2h</sub>. After the initial synthesis, the reactions were scaled up affording 50 grams of the crude ammonium salt and up to 1g of proligand.

The solubility of **5.1** was rather low, with DMSO remaining one of the few suitable solvents. Nickel, iron, cobalt and palladium acetates/halides with an additional base were used for complexation, all resulting in the formation of insoluble precipitates.

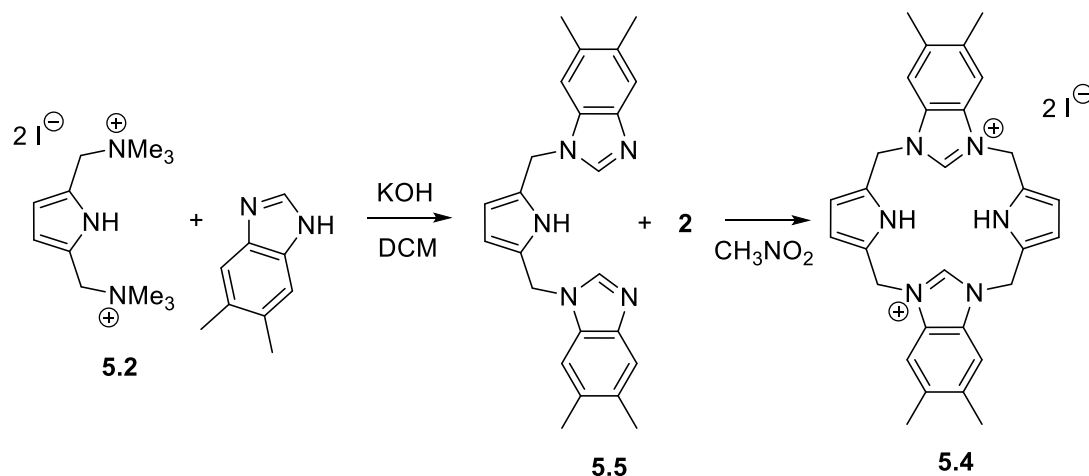


**Scheme 5-2** Synthetic pathway for proligand **5.1**

Only relatively weak bases were used, including carbonates, acetates and triethylamine, due to limited solvent options. ESI-MS and MALDI-TOF were used to provide preliminary results on the insoluble solids, however, the results were inconclusive.

The use of an alkylated imidazole was identified as a synthetically accessible derivative promising better solubility and the use of 4,5-dimethylimidazole was initially targeted. Dimethylimidazole was synthesized from glyoxal, formaldehyde and ammonium sulfate. The synthesis was low yielding, but extraction with ethyl acetate and a final wash with slight amounts of diethyl ether afforded 4,5-dimethylimidazole in high purity. Attempted alkylation with intermediate **5.2** was problematic under different conditions, leading to an oil that was difficult to purify and expected to contain multiple products based on NMR analysis. Dimethylbenzimidazole was also used as an alternative, leading to the expected products in relatively high yields (**Scheme 5.3**). The resultant NMR spectra of the neutral intermediate **5.5** and the dimethylbenzimidazole macrocycle **5.4** were similar to those of the parent system, with a reduction from 4 to 3 aromatic resonances as expected

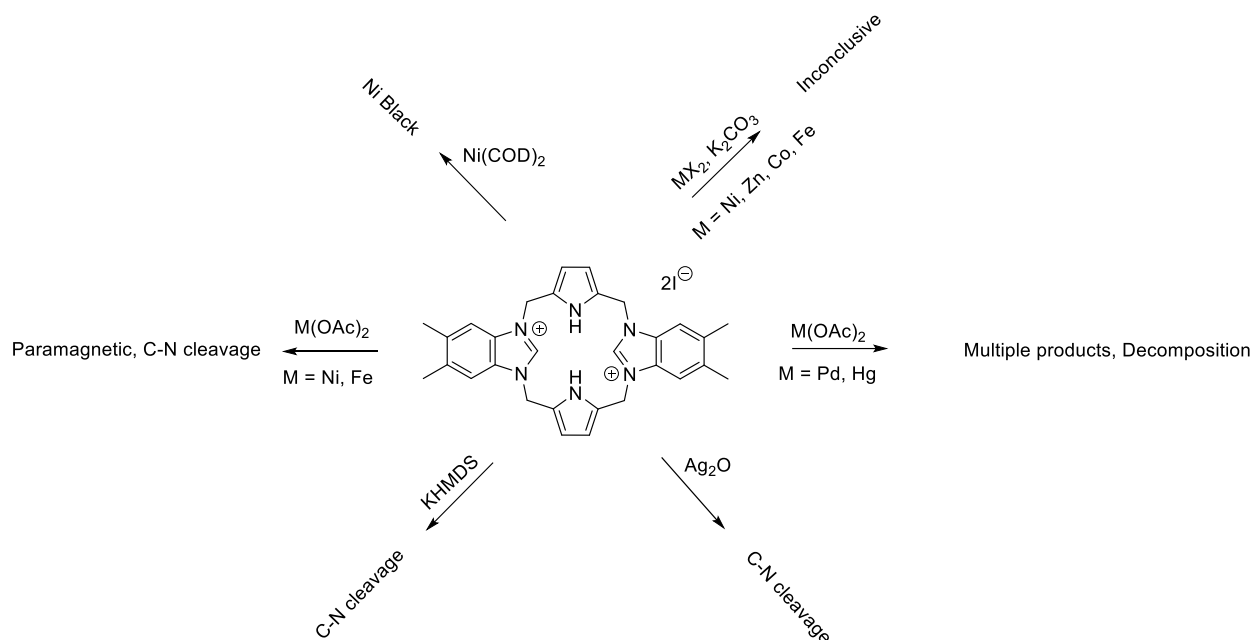
for a symmetry change from  $C_{2v}$  to a  $D_{2h}$  point group. In addition, the solubility of the dimethylbenzimidazole analog was slightly better in organic solvents such as THF and acetonitrile, enabling a wider selection of bases and metal reagents for complexation.



**Scheme 5-3** Synthetic pathway for proligand **5.4**

Various methods for complexation were fruitlessly pursued (**Scheme 5.4**), leading to the formation of insoluble precipitates or the cleavage of the C-N  $\alpha$ -pyrrole bond. C-N cleavage at methylene groups on 2,5-substituted pyrroles has been described in literature, with a simple pincer analog either providing no reaction, decomposing, or cleaving the C-N bond in the presence of weak bases such as  $Ag_2O$ .<sup>[205]</sup> With the addition of  $Ag_2O$  in DMSO or a strong base such as KHMDS in THF with proligand **5.4**, four aromatic resonances were observed in the spectrum of the resultant mixture, matching the  $^1H$  NMR spectrum for the neutral pincer **5.5**, as expected for C-N cleavage. In addition, attempted complexation with zinc using either acetates, triethylamine or carbonates as a base again resulted in a  $^1H$  NMR spectra that matched the open chain, neutral intermediate **5.5**. Resonances corresponding to the pyrrole fragment were not observed in the respective spectra. This was postulated to be due to pyrrole polymerization as the reaction always

produced insoluble precipitates.<sup>[206]</sup> In addition, when paramagnetic metals were for used for complexation, the only product identifiable by high-resolution ESI-MS was a coordination complex of the metal with the neutral intermediate **5.5**.



**Scheme 5-4** Selected complexation attempts with proligand **5.4**

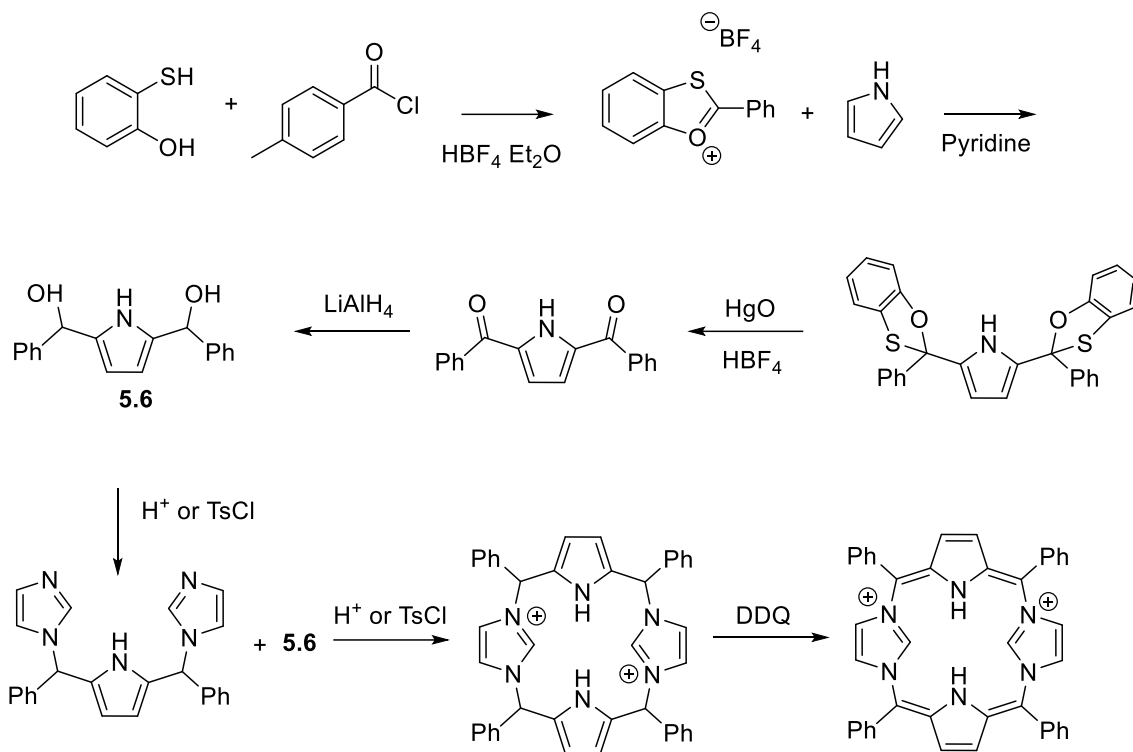
### 5.3 Unsaturated Carbene-porphyrinoids

Although the non-conjugated macrocycle was prone to decomposition through C-N cleavage, the unsaturation in the conjugated derivative should increase the relative bond order and lead to greater stability. Porphyrin derivatives can be unsaturated with dihydrogen acceptors, such as 2,3-dichloro-5,6-dicyano-1,4-benzoquinone (DDQ) and chloroanil, so a similar procedure was followed with compound **5.4**.<sup>[207,208]</sup> Initial attempts were unsuccessful and led to decomposition, so anion exchange with NH<sub>4</sub>PF<sub>6</sub> for increased solubility and to avoid any side reactivity with halides was conducted. The corresponding

PF<sub>6</sub> salt was purified and used for subsequent reactions with dihydrogen acceptors but maintained the same decomposition as the diiodide salt.

While dihydrogen acceptors were pursued, the use of hydrogen atom abstractors was also attempted by Zachary Dubrawski without success. One possibility for the observed decomposition of **5.4** with DDQ was the instability of the resulting meso positions, where porphyrins have been susceptible to oxidation/cleavage without appropriate stabilization.<sup>[209,210]</sup> The incorporation of phenyl groups in the meso-positions was seen as an alternative to stabilize the macrocycle and could potentially alleviate issues with C-N cleavage. The synthetic scheme towards the meso-substituted ligand is shown in **Scheme 5.5**, where the tolyl derivative of a benzoxathiolium was used instead of the phenyl for a NMR handle during the synthesis.<sup>[207,208,211–214]</sup> To avoid porphyrin formation and the 1,4-substitution of pyrrole with benzaldehyde, a protecting strategy was used. The use of a benzoxathiolium salt selectively substituted pyrrole at the 2 and 5 positions, which could be converted to diacylpyrrole via oxidation with hydrogen peroxide or mercuric oxide. The following reduction of the diacylpyrrole was performed with either NaBH<sub>4</sub> or freshly purified LiAlH<sub>4</sub>, leading to the secondary alcohol **5.6**. The <sup>1</sup>H NMR spectra showed this to be the expected mixture of two diastereomers, due to the presence of two newly formed stereocenters, with additional impurities. This was difficult to purify and according to literature reports crude **5.6** is commonly used in subsequent reactions without previous purification. The acid catalyzed condensation reaction with imidazole, or the use of toluenesulfonyl chloride to produce a better leaving group appeared to result in decomposition to a variety of different compounds by <sup>1</sup>H NMR. A few different reaction

conditions were attempted, although progress was hindered by the inability to convert compound **5.6** to the imidazole functionalized product.



**Scheme 5-5** Proposed synthetic pathway for a meso-substituted carbene porphyrinoid.

With continued difficulties in synthesis, and decomposition during complexation of the previous proligands, the project had moved away from the initial selection criteria. The targeted complexes were meant to be easily synthesized in gram quantities, stable under reducing conditions, provide a redox active framework to reduce overpotentials and have a high affinity for  $\text{CO}_2$  reduction over dihydrogen production. The initial proligands **5.1** and **5.4** were easily synthesized in large quantities, but did not lead to isolable metal complexes under a variety of reaction conditions employing different metals. Upon moving towards a meso-substituted analog, difficulties in synthesis and low yielding synthetic steps continued to reduce the applicability of the system towards large-scale implementation.



Although the use of carbenes as neutral nitrogen donor alternatives is reported to lead to increased activity of catalysts for electrochemical CO<sub>2</sub> reduction, the instability and difficulty in synthesis of the aforementioned compounds reduced the attractiveness of pursuing the project further. Efforts towards catalyst development transitioned towards other ligand designs in lieu of pursuing the macrocycles any further. Some of these other ligand designs and preliminary data on alternative catalysts are discussed in chapter 7.

## **5.4 Experimental**

### **2,5-Bis(dimethylaminomethyl)pyrrole**

Dimethylamine hydrochloride (30.023g, 368mmol) was dissolved in 37 wt% aqueous formaldehyde (30 mL, 403mmol) in a 250mL round bottom flask equipped with a magnetic stir bar. The solution was cooled with an ice bath before the addition of pyrrole (12.4mL, 179mmol) under vigorous stirring. The aqueous solution was brought to room temperature over a period of 30 minutes and stirred for an additional twelve hours before neutralization with a 20% NaOH solution to a pH of 6-8. The product was extracted with diethylether (3 x 30mL) and separated from the aqueous fraction before removal of volatiles with a rotary evaporator. The resulting crude oil was distilled at 80 °C and 7 millitorr affording 2,5-Bis(dimethylaminomethyl)pyrrole (19.673g, 61% yield) as a colorless liquid. <sup>1</sup>H NMR (400 MHz, CDCl<sub>3</sub>) δ 5.92 (d, 2H), 3.39 (s, 4H), 2.22 (s, 12H).

### **Compound 5.2**

Freshly distilled 2,5-Bis(dimethylaminomethyl)pyrrole (19.673g, 109mmol) was dissolved in 200mL of THF in a 500mL two-neck round bottom flask equipped with a magnetic stir bar. The solution was cooled with an ice bath before the dropwise addition of methyl iodide (20.27mL, 326mmol) with vigorous stirring. After addition, the reaction was warmed to

room temperature and stirred for an additional four hours, resulting in the precipitation of a white solid. 100mL of acetone was then added to the suspension, and stirred for an additional 30 minutes before collecting the precipitate *via* vacuum filtration on glass frit. The white precipitate was then suspended in 200mL of fresh acetone and stirred overnight before collecting again on a glass frit. The solid was dried in air, affording 2,5-Bis[(trimethylammonio)methyl]pyrrole diiodide **5.2** (44.896g, 89% yield) as a white solid. The crude material contained what was believed to be a side product that could not be removed through recrystallization, the use of dry solvents and inert atmosphere during the reaction or with additional equivalents of methyl iodide, so it was decided to use as a crude material in further reactions. <sup>1</sup>H NMR (400 MHz, D<sub>2</sub>O) δ 6.60 (s, 1H), 4.51 (s, 2H), 3.08 (s, 18H).

### Compound 5.3

Compound **5.2** (3.573g, 7.68mmol), imidazole (2.133g, 31mmol) and KOH (1.750g, 31mmol) was suspended in 50mL of DCM in a 150mL round bottom flask equipped with a magnetic stir bar. The reaction was stirred overnight at room temperature before removing volatiles on a rotary evaporator. The resulting solid was suspended in 50mL of water and filtered to afford a crude off-white solid. The precipitate was further washed with an additional 10mL of water and slight amounts of acetone before drying in air to obtain 2,5-Bis[(imidazole-1-yl)methyl]pyrrole (**5.3**) (1.454g, 83% yield). <sup>1</sup>H NMR (400 MHz, DMSO) δ 11.10 (s, 2H), 7.61 (s, 4H), 7.10 (s, 4H), 6.86 (s, 2H), 5.98 (d, 4H), 5.05 (s, 8H).

### Proligand 5.1

Compound **5.3** (0.475g, 2.1mmol) and compound **5.2** (0.972g, 2.1mmol) were dissolved in 20mL of nitromethane in a 100mL round bottom flask equipped with a magnetic stir bar.

The resulting suspension was stirred at 55 °C overnight, at which point the solution became homogeneous. The Solution was then cooled to room temperature, precipitating proligand **5.1** as an off-white solid. The solid was collected by filtration, washed with slight amounts of acetone and air dried, affording compound **5.1** (0.316g, 26% yield). <sup>1</sup>H NMR (400 MHz, DMSO) δ 11.20 (s, 2H), 8.57 (s, 2H), 7.84 (s, 4H), 6.26 (d, 4H), 5.34 (s, 8H).

### **Compound 5.5**

A similar synthetic pathway as (**5.3**) was followed, utilizing compound **5.2** (10.045g, 21.6mmol), dimethylbenzimidazole (9.428g, 64.5mmol) and KOH (3.618g, 64.5mmol) in 100mL of DCM. The resulting solid after removing volatiles was washed with water and dried overnight in air to afford compound **5.5** (5.057g, 61% yield) as an off-white solid. <sup>1</sup>H NMR (400 MHz, DMSO-*d*<sub>6</sub>) δ 11.12 (s, 1H), 8.02 (s, 2H), 7.34 (d, 4H), 6.02 (s, 2H), 5.25 (s, 4H), 2.27 (d, 12H).

### **Compound 5.4**

A similar synthetic pathway as proligand **5.1** was followed, utilizing compound **5.5** (0.750g, 1.9mmol), compound **5.2** (0.910g, 1.9mmol) and refluxed in acetonitrile in place of nitromethane to afford compound **5.4** (0.990g, 69% yield) as an off-white solid. <sup>1</sup>H NMR (400 MHz, DMSO) δ 11.12 (s, 2H), 9.05 (s, 2H), 8.07 (s, 4H), 6.36 (d, 4H), 5.61 (s, 8H), 2.44 (s, 12H).

### **4,5-Dimethylimidazole**

Glyoxal (5.36mL, 117mmol), 37 wt% aqueous formaldehyde (5mL, 67mmol) and ammonium sulfate (16.280g, 123mmol) was dissolved in 30mL of water and stirred overnight at room temperature in a 150mL round bottom flask equipped with a magnetic stir bar. The pH of the resulting solution was increased by the addition of 25g of 20%

aqueous NaOH, then 4,5-dimethylimidazole was extracted with 3x150mL portions of EtOAc. The organic fractions were collected, dried over anhydrous MgSO<sub>4</sub>, and evaporated to afford a crude red solid. The solid was sonicated with slight amounts of diethylether and filtered to afford 4,5-dimethylimidazole (4.071g, 63% yield) as a pale pink solid. <sup>1</sup>H NMR (400 MHz, CDCl<sub>3</sub>) δ 7.43 (s, 1H), 2.18 (s, 6H).

### **Benzoxathiolium salt**

Anhydrous and degassed p-toluoyl chloride (10mL, 76mmol) was dissolved in tetrafluoroboric acid diethyl ether complex (12.5mL, 92mmol) in a swivel-frit apparatus under an atmosphere of argon. A separate solution of degassed o-mercaptophenol (7.5mL, 75mmol) in tetrafluoroboric acid diethyl ether complex (12.5mL, 92mmol) was added dropwise at 0°C to the solution containing p-toluoyl chloride over a period of 30 minutes. The solution was then stirred at 35 °C for three hours before the addition of 25mL of anhydrous diethylether. The addition resulted in the precipitation of a yellow solid that was filtered under inert atmosphere using Schlenk techniques and dried under reduced pressure to afford the benzoxathiolium salt (19.473g, 83%) as a yellow solid. <sup>1</sup>H NMR (400 MHz, Acetonitrile-*d*<sub>3</sub>) δ 8.43 – 8.31 (m, 3H), 8.26 (dt, 1H), 8.02 (ddd, 1H), 7.90 (ddd, 1H), 7.72 – 7.64 (m, 2H), 2.61 (s, 3H).

### **2,5-bis(benzoxathiolium)pyrrole**

The benzoxathiolium salt (19.473g, 62mmol) was placed into a 2-neck 150mL round bottom flask charged with a magnetic stir bar in an argon filled glovebox. 20mL of anhydrous acetonitrile was added to the reaction vessel along with pyrrole (1.82 mL, 26mmol) and pyridine (5.13mL, 64mmol). The resulting suspension was stirred at room temperature for two hours before collecting the precipitate *via* filtration on a glass frit. The

precipitate was washed with water to remove pyridinium tetrafluoroborate and recrystallized from hot methanol to afford 2,5-bis(benzoxathiolium)pyrrole (6.349g, 47% yield).  $^1\text{H}$  NMR (400 MHz, Chloroform-*d*)  $\delta$  9.07 (s, 1H), 7.59 – 7.49 (m, 4H), 7.23 – 6.98 (m, 9H), 7.01 – 6.84 (m, 4H), 5.84 (dd, 2H), 2.36 (s, 6H).

### **2,5-diacylpyrrole**

2,5-bis(benzoxathiolium)pyrrole (6.004g, 11.5mmol) was dissolved in 60mL of glacial acetic acid and 6mL of 30% hydrogen peroxide in a 150mL round bottom flask equipped with a magnetic stir bar and reflux condenser. The solution was heated to 110 °C with stirring for 30 minutes before cooling to room temperature. After the solution had cooled, 120mL of water and 240mL of chloroform were added to the reaction mixture and the organic layer separated was from the aqueous fraction. The aqueous layer was extracted with an additional four 120mL chloroform fractions. The combined organic fractions were washed with 60mL of 5% NaOH solution followed by 120mL of deionized water and then dried over  $\text{MgSO}_4$ . Volatiles were then removed with a rotary evaporator to afford 2,5-diacylpyrrole (2.896g, 83% yield) as an off-white solid.  $^1\text{H}$  NMR (400 MHz,  $\text{CDCl}_3$ )  $\delta$  10.29 (s, 1H), 7.88 (d, 4H), 7.36 (d, 4H), 6.92 (d, 2H), 2.48 (s, 6H).

### **Compound 5.6**

2,5-diacylpyrrole (260mg, 0.86mmol) was dissolved in 5mL of anhydrous THF in a 50mL round bottom flask equipped with a magnetic stir bar and transferred *via* syringe dropwise to a suspension of  $\text{LiAlH}_4$  (650mg, 17mmol) in 10mL of anhydrous THF at 0°C. The resulting solution was stirred at 0 °C for three hours before the addition of 10mL water and 50mL DCM. The suspension was filtered through a glass frit and the organic fraction collected, washed with water and dried with anhydrous  $\text{MgSO}_4$  before removing volatiles

with a rotary evaporator. The resulting solid was sonicated in pentane and filtered on a glass frit affording compound **5.6** (120mg, 45% yield) as an off-white solid.

## Chapter 6 – Conclusions and final thoughts

The first two chapters of this thesis document the development of all-iron redox pair for redox flow battery applications, utilizing chelating nitrogen-based ligands to tune the  $\text{Fe}^{2/3+}$  redox couple within the solvent window of water. A potential difference of 0.92 V was obtained with commercially available  $[\text{Fe}(\text{bpy})_3]^{2+}$  and iron complex **2.2**. The organic envelopes were shown to provide stable iron complexes over 6 months in aqueous solutions and should help reduce crossover contamination through the membrane, which was deleterious in the only other reported RFB  $\text{Fe}^{2+}/\text{Fe}^{2+}$  redox pair. Although the included work is only a proof of concept, it reveals the potential for soluble iron-based redox flow batteries as a promising avenue towards energy storage when geographical or geological limitations prohibit the use of pumped hydro or compressed air. The use of appropriate ligands has led to a reasonable open-circuit voltage and the ability to alleviate parasitic dihydrogen production or iron hydroxide precipitation that is prevalent within current all-iron mixed RFBs. Future developments may lead to increased potential differences, solubility and identify cycling ability in order to determine the commercial applicability of all-soluble, all-iron RFBs.

An iron-based single-component active species was also developed based on computational work that predicts 9,10-anthraquinone frameworks as the most suitable organic-based candidates for the anolyte of an RFB. Although the use of quinone-based ligands resulted in poor electrochemical behavior (**2.4**) or difficulty in purification (**2.7**), the iron coordination complex featuring an anthraquinone-substituted terpyridine **2.6** shows promising redox activity as a single complex for anolyte and catholyte solutions. An increased open-circuit voltage is obtained through the use of an organic electrolyte at 1.86V

and complex **2.6** maintains electrochemical reversibility across multiple scan rates. A single component system based on iron further reduces issues associated with crossover contamination and can lower costs ascribed to membranes and expensive metal sources. Based on the extensive modification of anthroquinones towards increased solubility and tuning of the reduction potential, the incorporation of functional groups in complex **2.6** might provide appropriate water solubility and pH control to ensure that the reduction potential of the ligand falls within the potential window of water.

The second portion of this thesis is dedicated to the development of ligands for the electrochemical reduction of CO<sub>2</sub> catalyzed by first-row transition metals. A redox-active 1,3,5-triazapentadienyl-2,4-bis(2-pyridyl) ligand (TAPPy) employed as a nickel complex was shown to exclusively host a radical anion within the ligand framework upon reduction, and produce CO under reducing conditions. Mechanistic insight into the decomposition of the aforementioned complex was obtained by the use of spectroelectrochemistry, ATR-IR analysis of the isolated post-CPE precipitate, as well as NMR analysis. This revealed decomposition of the complex during electrolysis to nickel carbonyl containing compounds, and potential carbamate formation. Iron coordination complexes with the same TAPPy ligand reproducibly led to a homoleptic Fe(TAPPy)<sub>3</sub> complex that was electrochemically inactive towards CO<sub>2</sub> reduction.

In order to develop catalysts with increased activity, bis(carbene) macrocycles and porphyrinoids were targeted, with the aim of increasing the electron density at the metal center in comparison to literature reported N<sub>4</sub>-macrocycles and porphyrins. Increased solubility of the parent system **5.1** was achieved with the use of dimethylbenzimidazole, although the labile  $\alpha$ -pyrrole C-N bond in ligand **5.4** continuously cleaved upon the



addition of base or complexation attempts. Unsaturation towards the corresponding carbene-porphyrinoid led to decomposition of the ligand framework and additional synthetic attempts at a phenyl-substituted analog for increased stability were low yielding and problematic. Due to harsh conditions during the electrocatalytic reduction of CO<sub>2</sub>, ligands with greater stability and facile synthesis are needed, leading to the criteria for new catalyst designs to be revisited.

Selection criteria for new ligands should involve a facile synthesis and provide a system that is stable under reducing conditions. This criteria in combination with the modification of known catalysts can provide a better understanding of ideal ligand properties and contribute to future catalyst designs. The ubiquitous use of 2,2'-bipyridine in ligand frameworks towards electrocatalytic CO<sub>2</sub> reduction prompted the synthesis of a tetradentate framework with a 2,2'-bipyridine central donor and flanking phosphine chalcogenides. The corresponding phosphine oxide **7.2** forms monometallic and dinuclear complexes with Fe/Ni and Re respectively. Based on recent literature, dinuclear rhenium complexes have a potential for a bimetallic cooperative activation of CO<sub>2</sub>, leading to increased rates in comparison to the monometallic systems. Additional characterization and electrochemical analysis is needed to determine the applicability of the dinuclear rhenium complex **7.6**, with additional ligand scaffolds proposed based on the free phosphine **7.2** as pentadentate N5 ligands.

## Chapter 7 – Future Directions

### 7.1 Background Information

The development of fundamentally new ligand platforms for the electrocatalytic reduction of carbon dioxide proved more challenging than expected within the timeframe of a masters degree. As a consequence, improving on known systems appeared to be a suitable starting point in order to gain expertise in the field and provide a better understanding of ideal ligand properties, contributing to future catalyst designs. One of the most common building blocks in ligand design for CO<sub>2</sub> reduction has been 2,2'-bipyridine. The bipyridine subunit is one of the most famous chelating ligands in coordination chemistry, forming complexes with a variety of metals as a redox active ligand that is stable upon reduction.<sup>[215]</sup> 2,2'-bipyridine is a strong sigma donor,  $\pi$ -acidic and traditionally redox-non innocent throughout proposed catalytic cycles. The use of 2,2'-bipyridine in homogeneous CO<sub>2</sub> reduction spans across multiple different metals including chromium, iron, cobalt, nickel, molybdenum, ruthenium, palladium, tungsten, osmium and iridium. The majority of work reporting electrocatalytic reduction of carbon dioxide catalyzed by manganese and rhenium complexes is based on bipyridine.<sup>[103,143]</sup>

In addition to terpyridine, many other ligands in CO<sub>2</sub> reduction have been based off a 2,2'-bipyridine platform, such as quaterpyridines<sup>[216–218]</sup>, bipyricorrle<sup>[219]</sup>, imino bipyridyl<sup>[220]</sup> phosphine-substituted bipyridines,<sup>[221]</sup> and bipyridyl-N-heterocyclic carbene donors (**Figure 7.1**).<sup>[196]</sup> The 2,2'-bipyridine subunit remains intact in each example and commonly hosts additional electron density throughout the  $\pi$  framework upon reduction of the corresponding complexes. For example, ligand-based reductions occur on bipyricorrle

complex **B** at -1.75V vs. Fc/Fc<sup>+</sup>, complex **C** at -1.08V vs. NHE and compound **D** at -1.3V vs. SHE, with the majority of the electron density located on the bipyridine subunit.

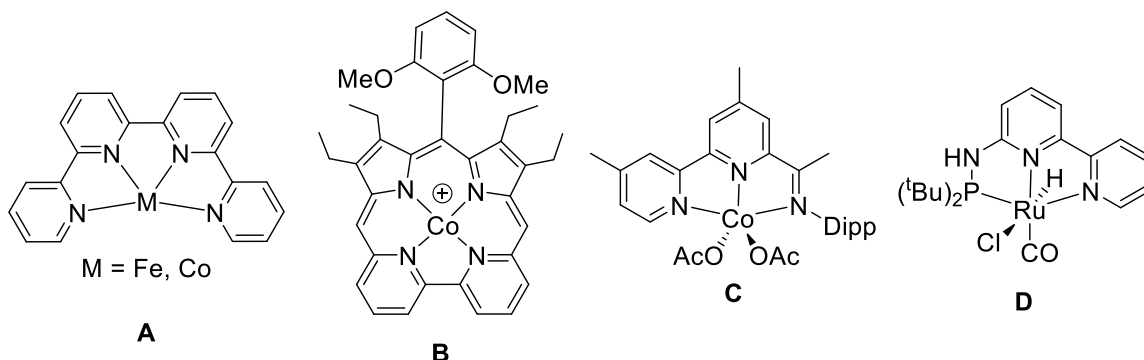
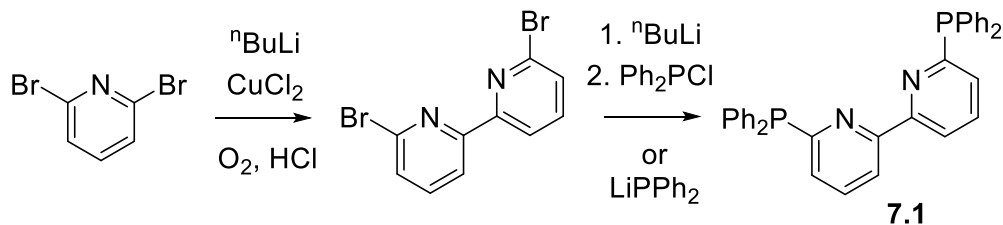


**Figure 7-1** Selected catalysts for electrochemical CO<sub>2</sub> reduction based on 2,2'-bipyridine ligand frameworks.

## 7.2 Bipyridine-Based Phosphine Chalcogenides with Iron and Nickel

Maintaining similar selection criteria as previous examples, ligands based on a bipyridine core that are easily synthesized in gram quantities, redox-active and stable under reducing conditions were targeted with the aim of identifying complexes with high activity and selectivity towards CO<sub>2</sub> reduction. With these criteria, a 6,6'-disubstituted 2,2'-bipyridine was identified as a potential framework suitable for CO<sub>2</sub> reduction on different complexes. A facile synthesis and versatility towards donor modification allows for the generation of several potential ligands, all based on a 2,2'-bipyridine central donor. The initial targets included a phosphine oxide and phosphine sulfide, with future works

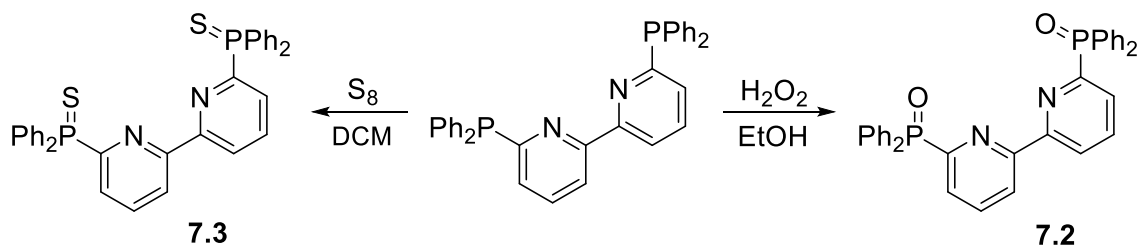


**Scheme 7-1** Synthesis of free phosphine **7.1**

incorporating iminophosphoranes, all stemming from phosphine **7.1** (**Scheme 7.1**).

6,6'-dibromo-2,2'-bipyridine was synthesized from 2,6-dibromopyridine via oxidative cross-coupling, in the presence of half an equivalent of copper(II) chloride and molecular oxygen. The free phosphine **7.1** can then be synthesized by either the addition of freshly prepared lithium diphenyl phosphide or lithium halogen exchange with  $^n\text{BuLi}$  and subsequent addition of chlorodiphenylphosphine. The use of lithium diphenyl phosphide led to cleaner reactivity, so this method was used in subsequent ligand synthesis.

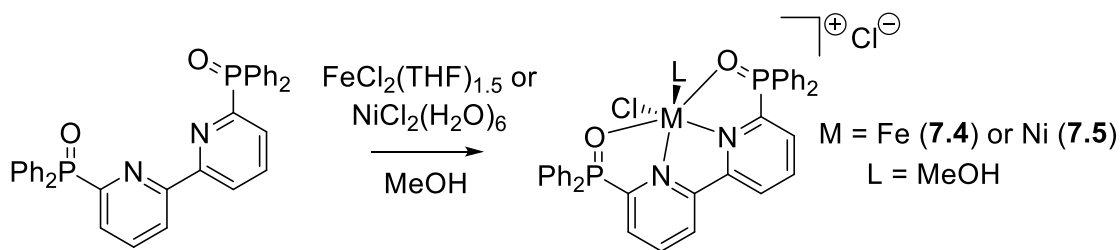
The free phosphine **7.1** can be oxidized with hydrogen peroxide or elemental sulfur to obtain the corresponding phosphine oxide **7.2** or phosphine sulfide **7.3** (**Scheme 7.2**). The oxidation is confirmed by  $^{31}\text{P}$  NMR, with the free phosphine **7.1** producing a resonance at -2.96 ppm, compound **7.2** at 20.062 ppm and compound **7.3** at 38.78 ppm.



**Scheme 7-2** Synthesis of oxidized phosphines **7.2** and **7.3**

Metalation proceeds readily with the phosphine oxide, leading to an immediate color change with the addition of  $\text{FeCl}_2(\text{THF})_{1.5}$  in methanol (**Scheme 7.3**). Single crystals of the iron complex **7.4** were grown by layering a concentrated solution of **7.4** in methanol on benzene, which were used to confirm the solid state structure by X-Ray crystallography. The iron complex exists as a cation in the solid state, with only one chloride bound covalently and the remaining coordination site occupied by the solvated methanol (**Figure 7.1**). The pseudo-octahedral structure appears slightly strained in the equatorial plane, with

an O-Fe-O bond angle of  $128.18(7)^{\circ}$  in comparison to an untethered bipyridyl-N-heterocyclic carbene donor used in CO<sub>2</sub> reduction with all donor-metal-donor bond angles between 88.9 and  $94.7^{\circ}$ <sup>[196]</sup>



**Scheme 7-3** Synthesis of coordination complexes **7.4** and **7.5**.

The corresponding nickel complex was also synthesized by stirring  $\text{NiCl}_2(\text{H}_2\text{O})_6$  and ligand **7.3** in methanol overnight. Slow evaporation of a concentrated solution of **7.5** in methanol produced single crystals suitable for X-Ray diffraction, which revealed a cationic pseudo-octahedral structure remarkably similar to that of complex **7.4** (**Figure 7.2**). Electrochemical analysis of both **7.4** and **7.5** in acetonitrile showed increased resistance over successive scans, with visible decomposition on the glassy carbon electrode

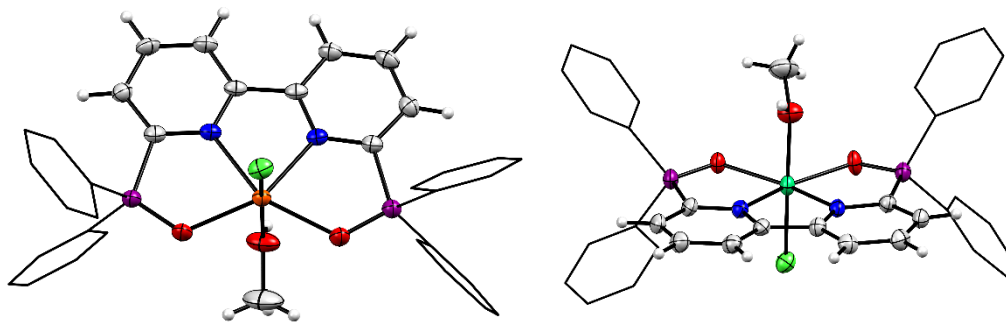


**Figure 7-2** Solid state structures of complex **7.4** (left) and **7.5** (right) drawn at 50% probability ellipsoids and wireframe.

and no observable current enhancement under an atmosphere of carbon dioxide. With the evident decomposition upon reduction, we decided not to pursue complexes **7.4** and **7.5** under different conditions for optimization towards CO<sub>2</sub> reduction.

### 7.3 Bimetallic Rhenium Complexes

Although the iron and nickel complexes were ineffective as catalysts, the extensive literature of group 7 bipyridine complexes in CO<sub>2</sub> reduction encouraged us to react ligand **7.2** with freshly prepared Re(CO)<sub>5</sub>Br, with the aim of obtaining the monometallic Re(**2**)(CO)Br. The reaction of **7.2** with Re(CO)<sub>5</sub>Br proceeds readily at 100 °C in toluene, producing a relatively insoluble yellow crystalline product after heating overnight. Analysis of the crystalline material by X-Ray crystallography revealed a homobimetallic complex with ligand **7.2**, where the bipyridine subunit is twisted out of plane to accommodate two equivalents of Re(CO)<sub>3</sub>Br (**Figure 7.3**). The synthesis of the binuclear complex was scaled up using two equivalents of Re(CO)<sub>5</sub>Br and purified to afford complex **7.6** as a diamagnetic yellow solid in relatively low yields after purification (15%). The <sup>31</sup>P NMR spectrum featuring a single phosphine resonance at 60.07 ppm and the <sup>1</sup>H and spectrum matched the identified structure. It is noteworthy that during the initial

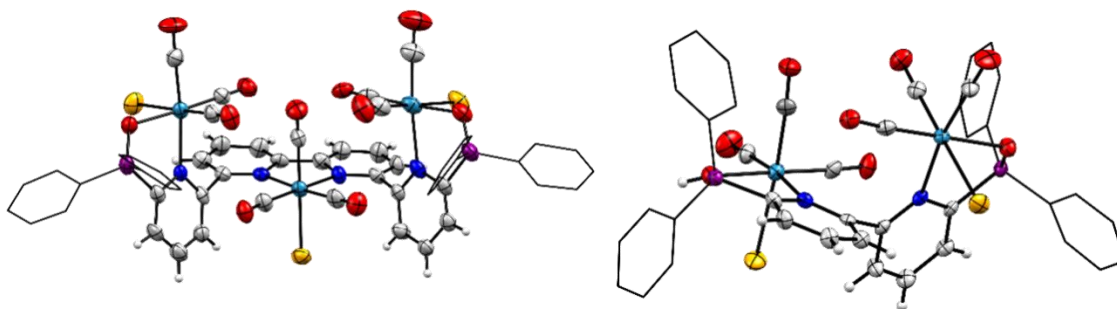


**Figure 7-3** Solid state structures of homotrimetallic rhenium complex (left) and complex **7.6** (right) drawn at 50% probability ellipsoids and wireframe.

characterization, a homotrimetallic impurity was identified by X-Ray crystallography (**Figure 7.3**). It is believed to be due to a quaterpyridine-based impurity present in the ligand.

Although the binuclear rhenium complex was unexpected, cooperative bimetallic rhenium complexes have been shown in literature to be more active than the monometallic analogs.<sup>[222–225]</sup> A modified mechanism in which cooperative activation of CO<sub>2</sub> between the two metal centers leads to an increase in the activity of the complex could be promising for further reducing the overpotential and increasing TOF. In addition, the use of dinuclear ruthenium complexes with a central bipyridine framework has also provided active catalysts for CO<sub>2</sub> reduction.<sup>[226]</sup>

Prior to scaling up the reaction and additional recrystallization/purification, preliminary electrochemical analysis of complex **7.6** was obtained in dry DMF. Two reversible reduction waves were observed under an argon atmosphere. The first redox event was subtle at -1.75V vs. Fc/Fc<sup>+</sup> and was further reduced to baseline upon successive scans (2-3 scans at 100mVs<sup>-1</sup>). While the first redox couple decreased in intensity, a separate reversible reduction event appeared at -2.25V and was stable over continued sweeps. When the solution was mixed or left to freely diffuse over a couple minutes, the process repeated itself and returned to a voltammogram that featured a single redox couple at -1.75V. In contrast to the first reduction, the second reduction wave showed substantial current enhancement under an atmosphere of CO<sub>2</sub>, in which no proton sources were added. The reduction potentials obtained at -1.75V and -2.25V are consistent with the first and second reduction waves of Re(bpy)CO<sub>3</sub>Cl, which appear at -1.74V and -2.13V respectively (Fc/Fc<sup>+</sup> = 0.4V vs. SCE),<sup>[227]</sup> where the initial reduction leads to a rhenium-rhenium dimer

formation.<sup>[139]</sup> Interestingly, after additional purification, only the first redox event remained in the resulting voltammogram and did not show any current enhancement upon addition of carbon dioxide. Additional work needs to be pursued in order to identify if the homobimetallic complex **7.6** undergoes a chemical transformation under reducing conditions such as dimerization that could lead to an active catalyst. Unfortunately, conditions have not been optimized at this point in time and no concrete conclusions can be drawn. Another alternative is to synthesize the quaterpyridine ligand that was observed in the homotrimetallic rhenium complex (*vide supra*) and identify if the trinuclear complex was the active component in the initial screen of complex **7.6**.

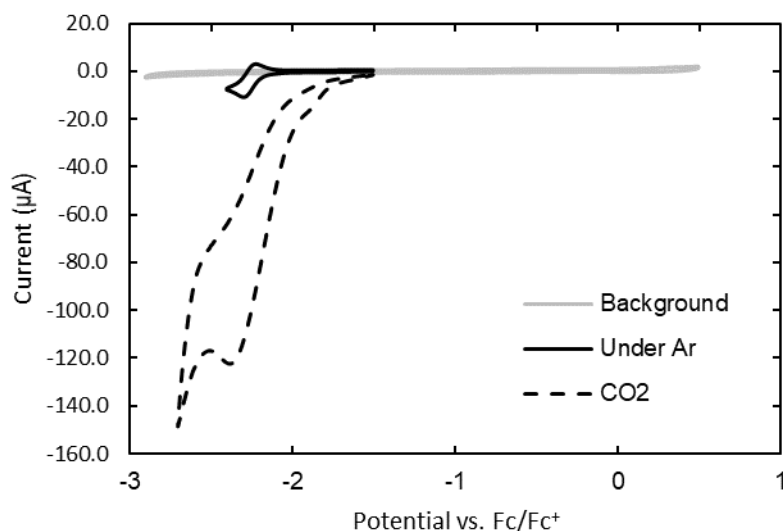


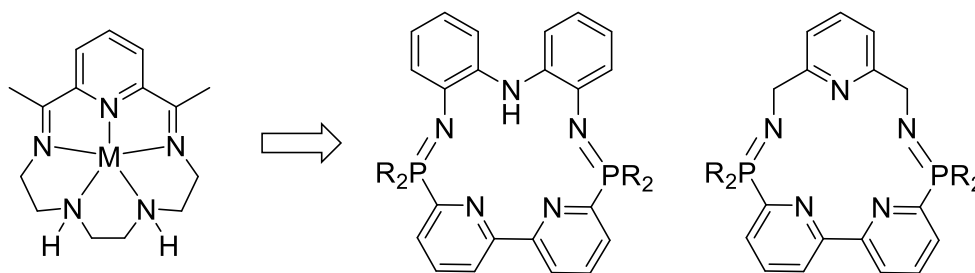
**Figure 7-4** Cyclic voltammogram of complex **7.6** (1.0 mM) at 0.1 V s<sup>-1</sup> under Ar (black) and CO<sub>2</sub> (Dashed line) with the background scans shown in grey. Conditions: 0.1 M <sup>n</sup>Bu<sub>4</sub>NPF<sub>6</sub>, DMF, glassy carbon disk working electrode, Pt wire counter electrode, Ag/AgCl reference electrode and internally referenced to ferrocene.

Surprisingly, when all complexation attempts were replicated with the phosphine sulfide **7.3**, no coordination to the metal center was observed. The phosphine sulfide is traditionally a stronger Lewis base, so it was expected that it would form similar complexes



as the phosphine oxide **7.2**.<sup>[228,229]</sup> One rationale for the observed behavior is that geometrical constraints due to an increased phosphine sulfide bond distance inhibited coordination: the P=E bond distance in Ph<sub>3</sub>P=E is 1.484(1) Å for O and 1.950(3) Å for S.<sup>[230]</sup>

In addition to further investigation into the electrochemical activity of complex **7.6**, other ligand platforms based on the parent phosphine **7.1** can be pursued. The use of iminophosphoranes instead of phosphine chalcogenides can enable a pentadentate, macrocyclic nitrogen based ligand similar to that of reported cobalt and iron complexes that are active for CO<sub>2</sub> reduction.<sup>[231]</sup> Potential ligand designs are shown alongside the literature reported complex in **Scheme 7.4**, where the resulting ligands could be synthesized from either the free phosphine **7.1** and a bisazide or the use of a free diamine and R<sub>3</sub>PX<sub>2</sub> where X = Cl or Br.



**Scheme 7-4** Potential proligands and ligands based on a pentadentate N5 complex used for electrochemical CO<sub>2</sub> reduction<sup>[231]</sup>

## 7.4 Experimental

### 6,6'-dibromo-2,2'-bipyridine

2,6-dibromopyridine (5.00g, 21.1mmol) was charged into a 150mL 2-neck round bottom flask equipped with a magnetic stir bar and placed under an argon atmosphere *via* Schlenk techniques. 20mL of anhydrous diethyl ether was transferred into the reaction vessel and

the resulting suspension was cooled to -78 °C before the dropwise addition of 1.6M <sup>n</sup>BuLi (14.5mL, 23.2mmol). The suspension was stirred at -78 °C until a homogeneous solution was obtained, upon which anhydrous CuCl<sub>2</sub> (1.419g, 10.5 mmol) was added in one portion through the side arm under a heavy flow of argon. The resulting suspension was stirred at -78°C under an argon atmosphere for an additional hour before opening to atmospheric conditions and bubbling air through the solution. The air was bubbled through the solution upon warming to room temperature and for an additional hour before the addition of 6M HCl (16.3mL). After the addition of HCl, the suspension was stirred for 10 minutes followed by filtration on a glass frit. The precipitate was subsequently washed with 0.5M HCl, followed by water and slight amounts of acetone to afford 6,6'-dibromo-2,2'-bipyridine (1.855g, 56% yield) as an off-white solid. <sup>1</sup>H NMR (400 MHz, Chloroform-*d*) δ 8.40 (dd, 2H), 7.69 (t, 2H), 7.53 (dd, 2H).

### **Compound 7.1**

6,6'-dibromo-2,2'-bipyridine (500mg, 1.59 mmol) was charged into a 100mL round bottom flask equipped with a magnetic stir bar and attached to a swivel-frit apparatus. 20mL of anhydrous THF was then transferred into the reaction flask and cooled to -78 °C before the dropwise addition of 1.6M <sup>n</sup>BuLi (2.1mL, 3.36mmol). The reaction was stirred at -78 °C for an additional hour before the dropwise addition of PPh<sub>2</sub>Cl (0.615mL, 3.3 mmol), in which the solution was stirred at -78 °C for 1 hour before warming to room temperature. The reaction was stirred at room temperature overnight before filtration through the swivel frit apparatus and evaporation of the filtrate to dryness under reduced pressure. Pentane was condensed onto the resulting solid and the suspension was sonicated

before filtering back through the swivel frit to afford compound **7.1** (820mg, 98% yield) as an off-white solid.

Compound **7.1** could also be synthesized *via* a different method, as described herein. A 2-neck round bottom flask equipped with a magnetic stir bar was charged with lithium metal (200mg, 28.8 mmol) and connected to a swivel frit apparatus. 20mL of anhydrous THF was transferred into the reaction vessel before the dropwise addition of PPh<sub>2</sub>Cl (1.77mL, 9.6 mmol) under vigorous stirring. The reaction was stirred at room temperature overnight before filtration through the swivel frit apparatus and evaporation of the filtrate to dryness under reduced pressure. Pentane was condensed onto the resulting solid and the suspension was sonicated before filtering back through the swivel frit to afford LiPPh<sub>2</sub>(THF) (2.580g, 99% yield) as a bright yellow solid. The reagent was stored in the glovebox freezer before use in the subsequent reaction. 6,6'-dibromo-2,2'-bipyridine (500mg, 1.6mmol) and LiPPh<sub>2</sub>(THF) (951mg, 3.5 mmol) were added to separate 100mL 2-neck round bottom flasks equipped with magnetic stir bars and dissolved in 10mL of anhydrous THF, where the LiPPh<sub>2</sub> solution was attached to a swivel frit apparatus. The 6,6'-dibromo-2,2'-bipyridine solution was then added dropwise to the LiPPh<sub>2</sub> solution at room temperature and subsequently heated to 60 °C for 1.5 hours. Afterwards, volatiles were removed under reduced pressure followed by the addition of 20mL of anhydrous DCM. The resulting suspension was filtered through the swivel frit apparatus and the filtrate evaporated to dryness under reduced pressure. Pentane was condensed onto the resulting solid and the suspension was sonicated before filtering back through the swivel frit to afford compound **7.1** (638mg, 76% yield) as an off-white solid. <sup>1</sup>H NMR (400 MHz, CD<sub>2</sub>Cl<sub>2</sub>) δ 8.18 (d, 2H), 7.66 (td, 2H), 7.50 – 7.36 (m, 20H), 7.17 (dt, 2H). <sup>31</sup>P NMR (162 MHz, CD<sub>2</sub>Cl<sub>2</sub>) δ -2.96.

### Compound 7.2

Compound **7.1** (415mg, 0.79 mmol) was placed in a 150mL round bottom flask equipped with a magnetic stir bar and reflux condenser. The solid was dissolved in 40mL of absolute ethanol followed by the addition of 30% H<sub>2</sub>O<sub>2</sub> solution (0.41mL, 3.6 mmol) in one portion. The solution was refluxed for 30 minutes before cooling to room temperature and the addition of 100mL of water. The resulting suspension was filtered on a glass frit to afford compound **7.2** (370mg, 84% yield) as a white solid. <sup>1</sup>H NMR (400 MHz, CD<sub>2</sub>Cl<sub>2</sub>) δ 8.39-8.36 (m, 2H), 8.33-8.29 (m, 2H), 8.05-8.00 (m, 2H), 7.97-7.92 (m, 8H), 7.60-7.48 (m, 12H). <sup>31</sup>P NMR (162 MHz, CD<sub>2</sub>Cl<sub>2</sub>) δ 19.66.

### Compound 7.3

Compound **7.1** (250mg, 0.47 mmol) and elemental sulfur (100mg, 3.1 mmol) were placed in a 100mL round bottom flask equipped with a magnetic stir bar within an argon filled glovebox. 20mL of anhydrous DCM was condensed into the reaction flask and the resulting solution was stirred at room temperature for one hour. Excess sulfur was filtered off and the filtrate was evaporated to dryness on a rotary evaporator affording compound **7.3** (150mg, 54% yield) as an off white solid. <sup>1</sup>H NMR (400 MHz, CD<sub>2</sub>Cl<sub>2</sub>) δ 8.56 (ddd, 2H), 8.21 (ddd, 2H), 8.03 – 7.89 (m, 10H), 7.60 – 7.43 (m, 12H). <sup>31</sup>P NMR (162 MHz, CD<sub>2</sub>Cl<sub>2</sub>) δ 38.79.

### Complexes 7.4 and 7.5

Compound **7.2** (50mg, 0.9mmol) and FeCl<sub>2</sub>(THF)<sub>1.5</sub> (21mg, 0.9mmol) were added to a 50mL round bottom flask equipped with a magnetic stir bar and reflux condenser. The solids were dissolved in 15mL of methanol and refluxed overnight before removing volatiles with a rotary evaporator. The resulting red solid was washed with slight amounts

of water and acetone to afford complex **7.4** as a dark red solid. For the nickel complex **7.5**,  $\text{NiCl}_2(\text{H}_2\text{O})_6$  was used in place of  $\text{FeCl}_2(\text{THF})_{1.5}$ .

### **Complex 7.6**

Phosphine oxide **7.2** (230mg, 0.645 mmol) and sublimed  $\text{Re}(\text{CO})_5\text{Br}$  (524mg, 1.29 mmol) were added to a 100mL round bottom flask equipped with a magnetic stir bar in an argon filled glovebox. 20mL of anhydrous toluene was distilled into the reaction flask and the resulting solution heated at 100 °C overnight. The resulting yellow suspension was cooled with an ice bath prior to filtration and washed multiple times with fresh acetonitrile to afford complex **7.6** (120mg, 15% yield) as a yellow solid.  $^1\text{H}$  NMR (400 MHz,  $\text{CD}_2\text{Cl}_2$ )  $\delta$  8.76 (dt, 2H), 8.22 (td, 2H), 8.00 (ddd, 2H), 7.93 – 7.60 (m, 20H).  $^{31}\text{P}$  NMR (162 MHz,  $\text{CD}_2\text{Cl}_2$ )  $\delta$  60.07.

## References

- [1] R. J. Millar, J. S. Fuglestedt, P. Friedlingstein, J. Rogelj, M. J. Grubb, H. D. Matthews, R. B. Skeie, P. M. Forster, D. J. Frame, M. R. Allen, *Nat. Geosci.* **2017**, *10*, 741.
- [2] S. Peng, J. Huang, J. E. Sheehy, R. C. Laza, R. M. Visperas, X. Zhong, G. S. Centeno, G. S. Khush, K. G. Cassman, *Proc. Natl. Acad. Sci. U. S. A.* **2004**, *101*, 9971–9975.
- [3] M. A. Bender, T. R. Knutson, R. E. Tuleya, J. J. Sirutis, G. A. Vecchi, S. T. Garner, I. M. Held, *Science* **2010**, *327*, 454–458.
- [4] A. Cazenave, *Science* **2006**, *314*, 1250–1252.
- [5] A. J. Cavallo, *J. Sol. Energy Eng.* **2001**, *123*, 387–389.
- [6] B. W. Brook, A. Alonso, D. A. Meneley, J. Misak, T. Bles, J. B. van Erp, *Sustain. Mater. Technol.* **2014**, *1–2*, 8–16.
- [7] A. Z. Weber, M. M. Mench, J. P. Meyers, P. N. Ross, J. T. Gostick, Q. Liu, *J. Appl. Electrochem.* **2011**, *41*, 1137.
- [8] G. Kear, A. A. Shah, F. C. Walsh, *Int. J. Energy Res.* **2012**, *36*, 1105–1120.
- [9] **2019**.
- [10] H. Ibrahim, A. Ilinca, J. Perron, *Renew. Sustain. Energy Rev.* **2008**, *12*, 1221–1250.
- [11] W. Chen, Y. Jin, J. Zhao, N. Liu, Y. Cui, *Proc. Natl. Acad. Sci.* **2018**, *115*, 11694–11699.
- [12] R. F. Service, *Science* **2019**, *365*, 108–108.
- [13] B. Dunn, H. Kamath, J.-M. Tarascon, *Science* **2011**, *334*, 928–935.
- [14] B. Li, J. Liu, *Natl. Sci. Rev.* **2017**, *4*, 91–105.
- [15] J. Winsberg, T. Hagemann, T. Janoschka, M. D. Hager, U. S. Schubert, *Angew. Chem. Int. Ed.* **2017**, *56*, 686–711.
- [16] L. H. Thaller, *Redox Flow Cell Energy Storage Systems*, **1979**.
- [17] L. H. Thaller, August 26, 1974 - August 30, 1974, **1974**.
- [18] M. Skyllas-Kazacos, M. Rychcik, R. G. Robins, A. G. Fane, M. A. Green, *J. Electrochem. Soc.* **1986**, *133*, 1057–1058.
- [19] M. Skyllas-Kazacos, F. Grossmith, *J. Electrochem. Soc.* **1987**, *134*, 2950–2953.
- [20] M. Skyllas-Kazacos, M. Rychick, R. Robins, *All-Vanadium Redox Battery*, **1988**, US4786567A.
- [21] R. J. Remick, P. G. P. Ang, **1984**.
- [22] F. C. Walsh, *Pure Appl. Chem.* **2001**, *73*, 1819–1837.
- [23] P. K. Leung, C. Ponce-de-León, C. T. J. Low, A. A. Shah, F. C. Walsh, *J. Power Sources* **2011**, *196*, 5174–5185.
- [24] J. Cheng, L. Zhang, Y.-S. Yang, Y.-H. Wen, G.-P. Cao, X.-D. Wang, *Electrochem. Commun.* **2007**, *9*, 2639–2642.
- [25] M. H. Chakrabarti, R. A. W. Dryfe, E. P. L. Roberts, *Electrochimica Acta* **2007**, *52*, 2189–2195.
- [26] M. H. Chakrabarti, E. P. L. Roberts, C. Bae, M. Saleem, *Energy Convers. Manag.* **2011**, *52*, 2501–2508.
- [27] T. Yamamura, Y. Shiokawa, H. Yamana, H. Moriyama, *Electrochimica Acta* **2002**, *48*, 43–50.

- [28] F.-Q. Xue, Y.-L. Wang, W.-H. Wang, X.-D. Wang, *Electrochimica Acta* **2008**, *53*, 6636–6642.
- [29] L. Sanz, D. Lloyd, E. Magdalena, J. Palma, K. Kontturi, *J. Power Sources* **2014**, *268*, 121–128.
- [30] A. K. Manohar, K. M. Kim, E. Plichta, M. Hendrickson, S. Rawlings, S. R. Narayanan, *J. Electrochem. Soc.* **2016**, *163*, A5118–A5125.
- [31] K. Gong, F. Xu, J. B. Grunewald, X. Ma, Y. Zhao, S. Gu, Y. Yan, *ACS Energy Lett.* **2016**, *1*, 89–93.
- [32] D. Pletcher, R. Wills, *Phys. Chem. Chem. Phys.* **2004**, *6*, 1779–1785.
- [33] R. F. Savinell, C. C. Liu, R. T. Galasco, S. H. Chiang, J. F. Coetzee, *J. Electrochem. Soc.* **1979**, *126*, 357–360.
- [34] J. Pan, Y. Sun, J. Cheng, Y. Wen, Y. Yang, P. Wan, *Electrochem. Commun.* **2008**, *10*, 1226–1229.
- [35] Y. Yang, G. Zheng, Y. Cui, *Energy Environ. Sci.* **2013**, *6*, 1552–1558.
- [36] Y. Zhao, H. R. Byon, *Adv. Energy Mater.* **2013**, *3*, 1630–1635.
- [37] S. Creager, in *Handb. Electrochem.* (Ed.: C.G. Zoski), Elsevier, Amsterdam, **2007**, pp. 57–72.
- [38] N. Elgrishi, K. J. Rountree, B. D. McCarthy, E. S. Rountree, T. T. Eisenhart, J. L. Dempsey, *J. Chem. Educ.* **2018**, *95*, 197–206.
- [39] M. Skyllas-Kazacos, L. Cao, M. Kazacos, N. Kausar, A. Mousa, *ChemSusChem* **2016**, *9*, 1521–1543.
- [40] Y. K. Zeng, T. S. Zhao, L. An, X. L. Zhou, L. Wei, *J. Power Sources* **2015**, *300*, 438–443.
- [41] L. Li, S. Kim, W. Wang, M. Vijayakumar, Z. Nie, B. Chen, J. Zhang, G. Xia, J. Hu, G. Graff, J. Liu, Z. Yang, *Adv. Energy Mater.* **2011**, *1*, 394–400.
- [42] V. Viswanathan, A. Crawford, D. Stephenson, S. Kim, W. Wang, B. Li, G. Coffey, E. Thomsen, G. Graff, P. Balducci, M. Kintner-Meyer, V. Sprenkle, *J. Power Sources* **2014**, *247*, 1040–1051.
- [43] Y. Xu, Y. Wen, J. Cheng, G. Cao, Y. Yang, *Electrochem. Commun.* **2009**, *11*, 1422–1424.
- [44] Z. Li, S. Li, S. Liu, K. Huang, D. Fang, F. Wang, S. Peng, *Electrochem. Solid-State Lett.* **2011**, *14*, A171–A173.
- [45] Y. Zhao, S. Si, C. Liao, *J. Power Sources* **2013**, *241*, 449–453.
- [46] K. Takechi, Y. Kato, Y. Hase, *Adv. Mater.* **2015**, *27*, 2501–2506.
- [47] B. Huskinson, M. P. Marshak, C. Suh, S. Er, M. R. Gerhardt, C. J. Galvin, X. Chen, A. Aspuru-Guzik, R. G. Gordon, M. J. Aziz, *Nature* **2014**, *505*, 195–198.
- [48] X. Wei, W. Xu, M. Vijayakumar, L. Cosimbescu, T. Liu, V. Sprenkle, W. Wang, *Adv. Mater.* **2014**, *26*, 7649–7653.
- [49] S. H. Oh, C.-W. Lee, D. H. Chun, J.-D. Jeon, J. Shim, K. H. Shin, J. H. Yang, *J. Mater. Chem. A* **2014**, *2*, 19994–19998.
- [50] Y. Xu, Y.-H. Wen, J. Cheng, G.-P. Cao, Y.-S. Yang, *Electrochimica Acta* **2010**, *55*, 715–720.
- [51] J. Huang, L. Cheng, R. S. Assary, P. Wang, Z. Xue, A. K. Burrell, L. A. Curtiss, L. Zhang, *Adv. Energy Mater.* **2015**, *5*, 1401782.

- [52] X. Wei, W. Xu, J. Huang, L. Zhang, E. Walter, C. Lawrence, M. Vijayakumar, W. A. Henderson, T. Liu, L. Cosimbescu, B. Li, V. Sprenkle, W. Wang, *Angew. Chem.* **2015**, *127*, 8808–8811.
- [53] Y. H. Wen, H. M. Zhang, P. Qian, H. T. Zhou, P. Zhao, B. L. Yi, Y. S. Yang, *J. Electrochem. Soc.* **2006**, *153*, A929–A934.
- [54] Y. Matsuda, K. Tanaka, M. Okada, Y. Takasu, M. Morita, T. Matsumura-Inoue, *J. Appl. Electrochem.* **1988**, *18*, 909–914.
- [55] M. Morita, Y. Tanaka, K. Tanaka, Y. Matsuda, T. Matsumura-Inoue, *Bull. Chem. Soc. Jpn.* **1988**, *61*, 2711–2714.
- [56] P. J. Cappillino, H. D. Pratt, N. S. Hudak, N. C. Tomson, T. M. Anderson, M. R. Anstey, *Adv. Energy Mater.* **2014**, *4*, 1300566.
- [57] J. Mun, M.-J. Lee, J.-W. Park, D.-J. Oh, D.-Y. Lee, S.-G. Doo, *Electrochem. Solid-State Lett.* **2012**, *15*, A80–A82.
- [58] P. J. Cabrera, X. Yang, J. A. Suttill, K. L. Hawthorne, R. E. M. Brooner, M. S. Sanford, L. T. Thompson, *J. Phys. Chem. C* **2015**, *119*, 15882–15889.
- [59] G. M. Duarte, J. D. Braun, P. K. Giesbrecht, D. E. Herbert, *Dalton Trans.* **2017**, *46*, 16439–16445.
- [60] L. E. VanGelder, A. M. Kosswattaarachchi, P. L. Forrestel, T. R. Cook, E. M. Matson, *Chem. Sci.* **2018**, *9*, 1692–1699.
- [61] H. Kim, T. Yoon, J. Jang, J. Mun, H. Park, J. H. Ryu, S. M. Oh, *J. Power Sources* **2015**, *283*, 300–304.
- [62] Q. Liu, A. E. S. Sleightholme, A. A. Shinkle, Y. Li, L. T. Thompson, *Electrochem. Commun.* **2009**, *11*, 2312–2315.
- [63] P. Leung, J. Palma, E. Garcia-Quismondo, L. Sanz, M. R. Mohamed, M. Anderson, *J. Power Sources* **2016**, *310*, 1–11.
- [64] P. Peljo, D. Lloyd, N. Doan, M. Majaneva, K. Kontturi, *Phys. Chem. Chem. Phys.* **2014**, *16*, 2831–2835.
- [65] M. C. Tucker, A. Phillips, A. Z. Weber, *ChemSusChem* **2015**, *8*, 3996–4004.
- [66] L. W. Hruska, R. F. Savinell, *J. Electrochem. Soc.* **1981**, *128*, 18–25.
- [67] L. Wei, M. C. Wu, T. S. Zhao, Y. K. Zeng, Y. X. Ren, *Appl. Energy* **2018**, *215*, 98–105.
- [68] A. Hazza, D. Pletcher, R. Wills, *Phys. Chem. Chem. Phys.* **2004**, *6*, 1773–1778.
- [69] Q. Liu, A. A. Shinkle, Y. Li, C. W. Monroe, L. T. Thompson, A. E. S. Sleightholme, *Electrochem. Commun.* **2010**, *12*, 1634–1637.
- [70] K. L. Hawthorne, J. S. Wainright, R. F. Savinell, *J. Power Sources* **2014**, *269*, 216–224.
- [71] S. Selverston, E. Nagelli, J. S. Wainright, R. F. Savinell, *J. Electrochem. Soc.* **2019**, *166*, A1725–A1731.
- [72] K. L. Hawthorne, J. S. Wainright, R. F. Savinell, *J. Electrochem. Soc.* **2014**, *161*, A1662–A1671.
- [73] P. Schröder, D. Obendorf, T. Bechtold, *ChemElectroChem* **2019**, *6*, 3311–3318.
- [74] A. Dinesh, S. Olivera, K. Venkatesh, M. S. Santosh, M. G. Priya, Inamuddin, A. M. Asiri, H. B. Muralidhara, *Environ. Chem. Lett.* **2018**, *16*, 683–694.
- [75] P. B. Tsitovich, A. M. Kosswattaarachchi, M. R. Crawley, T. Y. Tittiris, T. R. Cook, J. R. Morrow, *Chem. – Eur. J.* **2017**, *23*, 15327–15331.



- [76] A. Lê, D. Floner, T. Roisnel, O. Cador, L. Chancelier, F. Geneste, *Electrochimica Acta* **2019**, 301, 472–477.
- [77] W. Wang, Z. Nie, B. Chen, F. Chen, Q. Luo, X. Wei, G.-G. Xia, M. Skyllas-Kazacos, L. Li, Z. Yang, *Adv. Energy Mater.* **2012**, 2, 487–493.
- [78] M. Lopez-Atalaya, G. Codina, J. R. Perez, J. L. Vazquez, A. Aldaz, *J. Power Sources* **1992**, 39, 147–154.
- [79] T. Ma, Z. Pan, L. Miao, C. Chen, M. Han, Z. Shang, J. Chen, *Angew. Chem. Int. Ed.* **2018**, 57, 3158–3162.
- [80] R. A. Potash, J. R. McKone, S. Conte, H. D. Abruña, *J. Electrochem. Soc.* **2016**, 163, A338–A344.
- [81] J. Winsberg, C. Stolze, S. Muench, F. Liedl, M. D. Hager, U. S. Schubert, *ACS Energy Lett.* **2016**, 1, 976–980.
- [82] W. Duan, R. S. Vemuri, J. D. Milshtein, S. Laramie, R. D. Dmello, J. Huang, L. Zhang, D. Hu, M. Vijayakumar, W. Wang, J. Liu, R. M. Darling, L. Thompson, K. Smith, J. S. Moore, F. R. Brushett, X. Wei, *J. Mater. Chem. A* **2016**, 4, 5448–5456.
- [83] C. S. Sevov, S. L. Fisher, L. T. Thompson, M. S. Sanford, *J. Am. Chem. Soc.* **2016**, 138, 15378–15384.
- [84] P. J. Cabrera, X. Yang, J. A. Suttill, R. E. M. Brooner, L. T. Thompson, M. S. Sanford, *Inorg. Chem.* **2015**, 54, 10214–10223.
- [85] J. Mun, D.-J. Oh, M. S. Park, O. Kwon, H.-T. Kim, S. Jeong, Y. G. Kim, M.-J. Lee, *J. Electrochem. Soc.* **2018**, 165, A215–A219.
- [86] E. C. Constable, in *Adv. Inorg. Chem.* (Ed.: A.G. Sykes), Academic Press, **1989**, pp. 1–63.
- [87] D. M. Cabral, P. C. Howlett, D. R. MacFarlane, *Electrochimica Acta* **2016**, 220, 347–353.
- [88] A. Kraft, A. Reichert, *Tetrahedron* **1999**, 55, 3923–3930.
- [89] J. Heidebrecht, C. Gendy, B. S. Gelfand, R. Roesler, *Polyhedron* **2018**, 143, 138–143.
- [90] H. Ferreira, M. M. Conradie, K. G. von Eschwege, J. Conradie, *Polyhedron* **2017**, 122, 147–154.
- [91] Y.-Y. Kou, G.-J. Xu, W. Gu, J.-L. Tian, S.-P. Yan, *J. Coord. Chem.* **2008**, 61, 3147–3157.
- [92] Y. Lei, C. Shi, F. C. Anson, *Inorg. Chem.* **1996**, 35, 3044–3049.
- [93] Q. Wu, M. Maskus, F. Pariente, F. Tobalina, V. M. Fernández, E. Lorenzo, H. D. Abruña, *Anal. Chem.* **1996**, 68, 3688–3696.
- [94] C. A. Goss, H. D. Abruna, *Inorg. Chem.* **1985**, 24, 4263–4267.
- [95] S. Er, C. Suh, M. P. Marshak, A. Aspuru-Guzik, *Chem. Sci.* **2015**, 6, 885–893.
- [96] L. Zeng, Y. Chen, H. Huang, J. Wang, D. Zhao, L. Ji, H. Chao, *Chem. – Eur. J.* **2015**, 21, 15308–15319.
- [97] A. Arrigo, F. Nastasi, G. La Ganga, F. Puntoriero, G. Zappalà, A. Licciardello, M. Cavazzini, S. Quici, S. Campagna, *Chem. Phys. Lett.* **2017**, 683, 96–104.
- [98] K. Hanson, N. Patel, M. T. Whited, P. I. Djurovich, M. E. Thompson, *Org. Lett.* **2011**, 13, 1598–1601.
- [99] É. Balogh-Hergovich, G. Speier, M. Réglér, M. Giorgi, E. Kuzmann, A. Vértes, *Inorg. Chem. Commun.* **2005**, 8, 457–459.

- [100] D. U. Nielsen, X.-M. Hu, K. Daasbjerg, T. Skrydstrup, *Nat. Catal.* **2018**, *1*, 244–254.
- [101] G. Centi, S. Perathoner, *Catal. Today* **2009**, *148*, 191–205.
- [102] E. E. Benson, C. P. Kubiak, A. J. Sathrum, J. M. Smieja, *Chem. Soc. Rev.* **2009**, *38*, 89–99.
- [103] R. Francke, B. Schille, M. Roemelt, *Chem. Rev.* **2018**, *118*, 4631–4701.
- [104] A. Coehn, S. Jahn, *Berichte Dtsch. Chem. Ges.* **1904**, *37*, 2836–2842.
- [105] R. H. Crabtree, *Chem. Rev.* **2012**, *112*, 1536–1554.
- [106] J. A. Widegren, R. G. Finke, *J. Mol. Catal. Chem.* **2003**, *198*, 317–341.
- [107] Y. Hori, in *Mod. Asp. Electrochem.* (Eds.: C.G. Vayenas, R.E. White, M.E. Gamboa-Aldeco), Springer New York, New York, NY, **2008**, pp. 89–189.
- [108] C. Kim, H. S. Jeon, T. Eom, M. S. Jee, H. Kim, C. M. Friend, B. K. Min, Y. J. Hwang, *J. Am. Chem. Soc.* **2015**, *137*, 13844–13850.
- [109] W. Zhang, Y. Hu, L. Ma, G. Zhu, Y. Wang, X. Xue, R. Chen, S. Yang, Z. Jin, *Adv. Sci.* **2018**, *5*, 1700275.
- [110] K. Takahashi, K. Hiratsuka, H. Sasaki, S. Toshima, *Chem. Lett.* **1979**, *8*, 305–308.
- [111] K. Hiratsuka, K. Takahashi, H. Sasaki, S. Toshima, *Chem. Lett.* **1977**, *6*, 1137–1140.
- [112] S. Meshitsuka, M. Ichikawa, K. Tamaru, *J. Chem. Soc. Chem. Commun.* **1974**, *0*, 158–159.
- [113] J. Hawecker, J.-M. Lehn, R. Ziessel, *J. Chem. Soc. Chem. Commun.* **1984**, *0*, 328–330.
- [114] B. P. Sullivan, C. M. Bolinger, D. Conrad, W. J. Vining, T. J. Meyer, *J. Chem. Soc. Chem. Commun.* **1985**, *0*, 1414–1416.
- [115] M. Hammouche, D. Lexa, J. M. Savéant, M. Momenteau, *J. Electroanal. Chem. Interfacial Electrochem.* **1988**, *249*, 347–351.
- [116] M. Tezuka, T. Yajima, A. Tsuchiya, Y. Matsumoto, Y. Uchida, M. Hidai, *J. Am. Chem. Soc.* **1982**, *104*, 6834–6836.
- [117] B. J. Fisher, R. Eisenberg, *J. Am. Chem. Soc.* **1980**, *102*, 7361–7363.
- [118] K. Elouarzaki, V. Kannan, V. Jose, H. S. Sabharwal, J.-M. Lee, *Adv. Energy Mater.* **2019**, *9*, 1900090.
- [119] C. Costentin, S. Drouet, G. Passard, M. Robert, J.-M. Savéant, *J. Am. Chem. Soc.* **2013**, *135*, 9023–9031.
- [120] S. Roy, B. Sharma, J. Pécaut, P. Simon, M. Fontecave, P. D. Tran, E. Derat, V. Artero, *J. Am. Chem. Soc.* **2017**, *139*, 3685–3696.
- [121] J. Song, E. L. Klein, F. Neese, S. Ye, *Inorg. Chem.* **2014**, *53*, 7500–7507.
- [122] K. T. Ngo, M. McKinnon, B. Mahanti, R. Narayanan, D. C. Grills, M. Z. Ertem, J. Rochford, *J. Am. Chem. Soc.* **2017**, *139*, 2604–2618.
- [123] M. D. Sampson, A. D. Nguyen, K. A. Grice, C. E. Moore, A. L. Rheingold, C. P. Kubiak, *J. Am. Chem. Soc.* **2014**, *136*, 5460–5471.
- [124] I. Bhugun, D. Lexa, J.-M. Savéant, *J. Phys. Chem.* **1996**, *100*, 19981–19985.
- [125] I. Bhugun, D. Lexa, J.-M. Savéant, *J. Am. Chem. Soc.* **1996**, *118*, 1769–1776.
- [126] C. Costentin, S. Drouet, M. Robert, J.-M. Savéant, *Science* **2012**, *338*, 90–94.
- [127] C. Costentin, G. Passard, M. Robert, J.-M. Savéant, *J. Am. Chem. Soc.* **2014**, *136*, 11821–11829.

- [128] E. M. Nichols, J. S. Derrick, S. K. Nistanaki, P. T. Smith, C. J. Chang, *Chem. Sci.* **2018**, 9, 2952–2960.
- [129] J. Agarwal, T. W. Shaw, H. F. Schaefer, A. B. Bocarsly, *Inorg. Chem.* **2015**, 54, 5285–5294.
- [130] A. Nicole Hellman, R. Haiges, S. C Marinescu, *Dalton Trans.* **2019**, DOI 10.1039/C9DT02689D.
- [131] D. C. Lacy, C. C. L. McCrory, J. C. Peters, *Inorg. Chem.* **2014**, 53, 4980–4988.
- [132] A. Chapovetsky, M. Welborn, J. M. Luna, R. Haiges, T. F. Miller, S. C. Marinescu, *ACS Cent. Sci.* **2018**, 4, 397–404.
- [133] C. Costentin, G. Passard, M. Robert, J.-M. Savéant, *Proc. Natl. Acad. Sci. U. S. A.* **2014**, 111, 14990–14994.
- [134] I. Azcarate, C. Costentin, M. Robert, J.-M. Savéant, *J. Phys. Chem. C* **2016**, 120, 28951–28960.
- [135] I. Azcarate, C. Costentin, M. Robert, J.-M. Savéant, *J. Am. Chem. Soc.* **2016**, 138, 16639–16644.
- [136] F. Franco, C. Cometto, F. F. Vallana, F. Sordello, E. Priola, C. Minero, C. Nervi, R. Gobetto, *Chem. Commun.* **2014**, 50, 14670–14673.
- [137] F. Franco, C. Cometto, L. Nencini, C. Barolo, F. Sordello, C. Minero, J. Fiedler, M. Robert, R. Gobetto, C. Nervi, *Chem. – Eur. J.* **2017**, 23, 4782–4793.
- [138] F. Franco, M. F. Pinto, B. Royo, J. Lloret-Fillol, *Angew. Chem. Int. Ed.* **2018**, 57, 4603–4606.
- [139] J. M. Smieja, C. P. Kubiak, *Inorg. Chem.* **2010**, 49, 9283–9289.
- [140] A. Álvarez, A. Bansode, A. Urakawa, A. V. Bavykina, T. A. Wezendonk, M. Makkee, J. Gascon, F. Kapteijn, *Chem. Rev.* **2017**, 117, 9804–9838.
- [141] J. Qiao, Y. Liu, F. Hong, J. Zhang, *Chem Soc Rev* **2014**, 43, 631–675.
- [142] D.-M. Feng, Y.-P. Zhu, P. Chen, T.-Y. Ma, *Catalysts* **2017**, 7, 373.
- [143] C. Jiang, A. W. Nichols, C. W. Machan, *Dalton Trans.* **2019**, DOI 10.1039/C9DT00491B.
- [144] Z. Dubrawski, J. Heidebrecht, B. M. P. Lombardi, A. S. Hyla, J. Willkomm, C. L. Radford, J.-B. Lin, G. C. Welch, S. Ponnurangam, R. Roesler, D. E. Prokopchuck, W. E. Piers, *Sustain. Energy Fuels* **2019**, 3, 1172–1181.
- [145] C. Costentin, J.-M. Savéant, *Nat. Rev. Chem.* **2017**, 1, 0087.
- [146] G. K. Rao, W. Pell, I. Korobkov, D. Richeson, *Chem. Commun.* **2016**, 52, 8010–8013.
- [147] M. Hammouche, D. Lexa, M. Momenteau, J. M. Saveant, *J. Am. Chem. Soc.* **1991**, 113, 8455–8466.
- [148] L. Garnier, Y. Rollin, J. Périchon, *J. Organomet. Chem.* **1989**, 367, 347–358.
- [149] K. S. Ratliff, R. E. Lentz, C. P. Kubiak, *Organometallics* **1992**, 11, 1986–1988.
- [150] M. Rudolph, S. Dautz, E.-G. Jäger, *J. Am. Chem. Soc.* **2000**, 122, 10821–10830.
- [151] E. Simón-Manso, C. P. Kubiak, *Organometallics* **2005**, 24, 96–102.
- [152] M. Y. Udugala-Ganeheneg, N. M. Dissanayake, Y. Liu, A. M. Bond, J. Zhang, *Transit. Met. Chem.* **2014**, 39, 819–830.
- [153] R. J. Haines, R. E. Wittrig, C. P. Kubiak, *Inorg. Chem.* **1994**, 33, 4723–4728.
- [154] R. Angamuthu, P. Byers, M. Lutz, A. L. Spek, E. Bouwman, *Science* **2010**, 327, 313–315.

- [155] R. E. Wittrig, G. M. Ferrence, J. Washington, C. P. Kubiak, *Inorganica Chim. Acta* **1998**, 270, 111–117.
- [156] D. A. Morgenstern, G. M. Ferrence, J. Washington, J. I. Henderson, L. Rosenhein, J. D. Heise, P. E. Fanwick, C. P. Kubiak, *J. Am. Chem. Soc.* **1996**, 118, 2198–2207.
- [157] T. Kajiware, A. Kamiyama, T. Ito, *Chem. Commun.* **2002**, 1256–1257.
- [158] M. N. Kopylovich, J. Lasri, M. F. C. Guedes da Silva, A. J. L. Pombeiro, *Dalton Trans* **2009**, 3074–3084.
- [159] M. D. Sampson, C. P. Kubiak, *J. Am. Chem. Soc.* **2016**, 138, 1386–1393.
- [160] C. W. Machan, M. D. Sampson, S. A. Chabolla, T. Dang, C. P. Kubiak, *Organometallics* **2014**, 33, 4550–4559.
- [161] J. D. Froehlich, C. P. Kubiak, *J. Am. Chem. Soc.* **2015**, 137, 3565–3573.
- [162] L. E. Lieske, A. L. Rheingold, C. W. Machan, *Sustain. Energy Fuels* **2018**, 2, 1269–1277.
- [163] H. Haas, R. K. Sheline, *J. Chem. Phys.* **1967**, 47, 2996–3021.
- [164] M. Fusè, I. Rimoldi, E. Cesarotti, S. Rampino, V. Barone, *Phys. Chem. Chem. Phys.* **2017**, 19, 9028–9038.
- [165] P. C. Servaas, D. J. Stufkens, A. Oskam, *Inorg. Chem.* **1989**, 28, 1774–1780.
- [166] M. Oçafrain, M. Devaud, J. Y. Nédelec, M. Troupel, *J. Organomet. Chem.* **1998**, 560, 103–107.
- [167] J. D. Froehlich, C. P. Kubiak, *Inorg. Chem.* **2012**, 51, 3932–3934.
- [168] R. N. Salvatore, S. I. Shin, A. S. Nagle, K. W. Jung, *J. Org. Chem.* **2001**, 66, 1035–1037.
- [169] P. Adams, F. A. Baron, *Chem. Rev.* **1965**, 65, 567–602.
- [170] M. Feroci, M. A. Casadei, M. Orsini, L. Palombi, A. Inesi, *J. Org. Chem.* **2003**, 68, 1548–1551.
- [171] R. N. Salvatore, V. L. Flanders, D. Ha, K. W. Jung, *Org. Lett.* **2000**, 2, 2797–2800.
- [172] M. Feroci, A. Inesi, L. Rossi, *Tetrahedron Lett.* **2000**, 41, 963–966.
- [173] S. O. N. Lill, U. Köhn, E. Anders, *Eur. J. Org. Chem.* **2004**, 2004, 2868–2880.
- [174] A. A. Leitch, I. Korobkov, A. Assoud, J. L. Brusso, *Chem. Commun.* **2014**, 50, 4934–4936.
- [175] R. Castañeda, A. Hollingshead, B. Gabidullin, J. L. Brusso, *Cryst. Growth Des.* **2017**, 17, 6572–6578.
- [176] A. Rosas-Hernández, H. Junge, M. Beller, M. Roemelt, R. Francke, *Catal. Sci. Technol.* **2017**, 7, 459–465.
- [177] E. Oberem, A. F. Roesel, A. Rosas-Hernández, T. Kull, S. Fischer, A. Spannenberg, H. Junge, M. Beller, R. Ludwig, M. Roemelt, R. Francke, *Organometallics* **2019**, 38, 1236–1247.
- [178] D. Benito-Garagorri, I. Lagoja, L. F. Veiros, K. A. Kirchner, *Dalton Trans.* **2011**, 40, 4778–4792.
- [179] P. J. Turrell, J. A. Wright, J. N. T. Peck, V. S. Oganessian, C. J. Pickett, *Angew. Chem. Int. Ed.* **2010**, 49, 7508–7511.
- [180] W. Hieber, G. Bader, *Berichte Dtsch. Chem. Ges. B Ser.* **1928**, 61, 1717–1722.
- [181] G. A. Bain, J. F. Berry, *J. Chem. Educ.* **2008**, 85, 532.
- [182] E. K. Barefield, D. H. Busch, S. M. Nelson, *Q. Rev. Chem. Soc.* **1968**, 22, 457–498.

- [183] X.-M. Hu, M. H. Rønne, S. U. Pedersen, T. Skrydstrup, K. Daasbjerg, *Angew. Chem. Int. Ed.* **2017**, *56*, 6468–6472.
- [184] J. Shen, R. Kortlever, R. Kas, Y. Y. Birdja, O. Diaz-Morales, Y. Kwon, I. Ledezma-Yanez, K. J. P. Schouten, G. Mul, M. T. M. Koper, *Nat. Commun.* **2015**, *6*, 8177.
- [185] D. Behar, T. Dhanasekaran, P. Neta, C. M. Hosten, D. Ejeh, P. Hambright, E. Fujita, *J. Phys. Chem. A* **1998**, *102*, 2870–2877.
- [186] Z. Weng, J. Jiang, Y. Wu, Z. Wu, X. Guo, K. L. Materna, W. Liu, V. S. Batista, G. W. Brudvig, H. Wang, *J. Am. Chem. Soc.* **2016**, *138*, 8076–8079.
- [187] Y. Wu, J. Jiang, Z. Weng, M. Wang, D. L. J. Broere, Y. Zhong, G. W. Brudvig, Z. Feng, H. Wang, *ACS Cent. Sci.* **2017**, *3*, 847–852.
- [188] M. Jouny, W. Luc, F. Jiao, *Ind. Eng. Chem. Res.* **2018**, *57*, 2165–2177.
- [189] X. Li, P. Anderson, H.-R. M. Jhong, M. Paster, J. F. Stubbins, P. J. A. Kenis, *Energy Fuels* **2016**, *30*, 5980–5989.
- [190] J. Agarwal, T. W. Shaw, C. J. Stanton, G. F. Majetich, A. B. Bocarsly, H. F. Schaefer, *Angew. Chem. Int. Ed.* **2014**, *53*, 5152–5155.
- [191] J. D. Cope, N. P. Liyanage, P. J. Kelley, J. A. Denny, E. J. Valente, C. E. Webster, J. H. Delcamp, T. K. Hollis, *Chem. Commun.* **2017**, *53*, 9442–9445.
- [192] M. Sheng, N. Jiang, S. Gustafson, B. You, D. H. Ess, Y. Sun, *Dalton Trans.* **2015**, *44*, 16247–16250.
- [193] J. A. Therrien, M. O. Wolf, B. O. Patrick, *Inorg. Chem.* **2014**, *53*, 12962–12972.
- [194] V. S. Thoi, C. J. Chang, *Chem. Commun.* **2011**, *47*, 6578–6580.
- [195] V. S. Thoi, N. Kornienko, C. G. Margarit, P. Yang, C. J. Chang, *J. Am. Chem. Soc.* **2013**, *135*, 14413–14424.
- [196] X. Su, K. M. McCardle, J. A. Panetier, J. W. Jurss, *Chem. Commun.* **2018**, *54*, 3351–3354.
- [197] J. A. Therrien, M. O. Wolf, *Inorg. Chem.* **2017**, *56*, 1161–1172.
- [198] J. A. Therrien, M. O. Wolf, B. O. Patrick, *Dalton Trans.* **2018**, *47*, 1827–1840.
- [199] R. S. Simons, J. C. Garrison, W. G. Kofron, C. A. Tessier, W. J. Youngs, *Tetrahedron Lett.* **2002**, *43*, 3423–3425.
- [200] J. C. Garrison, R. S. Simons, W. G. Kofron, C. A. Tessier, W. J. Youngs, *Chem. Commun.* **2001**, *0*, 1780–1781.
- [201] J. C. Garrison, R. S. Simons, J. M. Talley, C. Wesdemiotis, C. A. Tessier, W. J. Youngs, *Organometallics* **2001**, *20*, 1276–1278.
- [202] M. V. Baker, B. W. Skelton, A. H. White, C. C. Williams, *Organometallics* **2002**, *21*, 2674–2678.
- [203] I. Klawitter, M. R. Anneser, S. Dechert, S. Meyer, S. Demeshko, S. Haslinger, A. Pöthig, F. E. Kühn, F. Meyer, *Organometallics* **2015**, *34*, 2819–2825.
- [204] H. Jiang, H. Ding, K. Ge, P. Guang, Y. Li, X. Liu, G. Pang, Y. Shi, *hc* **2012**, *18*, 165–167.
- [205] K. Lin, L.-E. Chile, S. C. Zhen, P. D. W. Boyd, D. C. Ware, P. J. Brothers, *Inorganica Chim. Acta* **2014**, *422*, 95–101.
- [206] Y. Tan, K. Ghandi, *Synth. Met.* **2013**, *175*, 183–191.
- [207] P. D. Rao, S. Dhanalekshmi, B. J. Littler, J. S. Lindsey, *J. Org. Chem.* **2000**, *65*, 7323–7344.

- [208] Z. Liu, A. A. Yasseri, R. S. Loewe, A. B. Lysenko, V. L. Malinovskii, Q. Zhao, S. Surthi, Q. Li, V. Misra, J. S. Lindsey, D. F. Bocian, *J. Org. Chem.* **2004**, *69*, 5568–5577.
- [209] H. Kalish, H. M. Lee, M. M. Olmstead, L. Latos-Grażyński, S. P. Rath, A. L. Balch, *J. Am. Chem. Soc.* **2003**, *125*, 4674–4675.
- [210] S. P. Rath, H. Kalish, L. Latos-Grażyński, M. M. Olmstead, A. L. Balch, *J. Am. Chem. Soc.* **2004**, *126*, 646–654.
- [211] A. J. McNeece, M.-C. Chang, A. S. Filatov, J. S. Anderson, *Inorg. Chem.* **2018**, *57*, 7044–7050.
- [212] M. Barbero, S. Cadamuro, J. Degani, R. Fochi, A. Gatti, V. Regondi, **1988**, *53*, 2245–2250.
- [213] T. Higashino, A. Kumagai, H. Imahori, *Chem. Commun.* **2017**, *53*, 5091–5094.
- [214] D. Faye, M. D. Mbaye, S. Coufourier, A. Lator, S. Y. Dieng, S. Gaillard, J.-L. Renaud, *Comptes Rendus Chim.* **2017**, *20*, 492–499.
- [215] C. Kaes, A. Katz, M. W. Hosseini, *Chem. Rev.* **2000**, *100*, 3553–3590.
- [216] C. Cometto, L. Chen, E. Anxolabéhère-Mallart, C. Fave, T.-C. Lau, M. Robert, *Organometallics* **2019**, *38*, 1280–1285.
- [217] C. Cometto, L. Chen, D. Mendoza, B. Lassalle-Kaiser, T.-C. Lau, M. Robert, *ChemSusChem* **2019**, *12*, 4500–4505.
- [218] M. Wang, L. Chen, T.-C. Lau, M. Robert, *Angew. Chem. Int. Ed.* **2018**, *57*, 7769–7773.
- [219] A. Ogawa, K. Oohora, W. Gu, T. Hayashi, *Chem. Commun.* **2019**, *55*, 493–496.
- [220] F.-W. Liu, J. Bi, Y. Sun, S. Luo, P. Kang, *ChemSusChem* **2018**, *11*, 1656–1663.
- [221] S. Min, S. Rasul, H. Li, D. C. Grills, K. Takanabe, L.-J. Li, K.-W. Huang, *ChemPlusChem* **2016**, *81*, 166–171.
- [222] W. Yang, S. Sinha Roy, W. C. Pitts, R. L. Nelson, F. R. Fronczek, J. W. Jurss, *Inorg. Chem.* **2018**, *57*, 9564–9575.
- [223] J.-P. Du, A. Wilting, I. Siewert, *Chem. – Eur. J.* **2019**, *25*, 5555–5564.
- [224] N. P. Liyanage, W. Yang, S. Guertin, S. S. Roy, C. A. Carpenter, R. E. Adams, R. H. Schmehl, J. H. Delcamp, J. W. Jurss, *Chem. Commun.* **2019**, *55*, 993–996.
- [225] H.-Y. Kuo, T. S. Lee, A. T. Chu, S. E. Tignor, G. D. Scholes, A. B. Bocarsly, *Dalton Trans.* **2019**, *48*, 1226–1236.
- [226] M. M. Ali, H. Sato, T. Mizukawa, K. Tsuge, M. Haga, K. Tanaka, *Chem. Commun.* **1998**, 249–250.
- [227] N. G. Connelly, W. E. Geiger, *Chem. Rev.* **1996**, *96*, 877–910.
- [228] R. S. Edmundson, in *Organophosphorus Compd.* 1992, John Wiley & Sons, Ltd, **2006**, pp. 287–407.
- [229] J. A. Dobado, H. Martínez-García, Molina, M. R. Sundberg, *J. Am. Chem. Soc.* **1998**, *120*, 8461–8471.
- [230] D. G. Gilheany, *Chem. Rev.* **1994**, *94*, 1339–1374.
- [231] L. Chen, Z. Guo, X.-G. Wei, C. Gallenkamp, J. Bonin, E. Anxolabéhère-Mallart, K.-C. Lau, T.-C. Lau, M. Robert, *J. Am. Chem. Soc.* **2015**, *137*, 10918–10921.

## Permissions

This Agreement between Mr. Joshua Heidebrecht ("You") and Elsevier ("Elsevier") consists of your license details and the terms and conditions provided by Elsevier and Copyright Clearance Center.

License Number	4696640627637
License date	Oct 26, 2019
Licensed Publisher	Content Elsevier
Licensed Publication	Content Sustainable Materials and Technologies
Licensed Content Title	Why nuclear energy is sustainable and has to be part of the energy mix
Licensed Content Author	Barry W. Brook,Agustin Alonso,Daniel A. Meneley,Jozef Misak,Tom Blee,Jan B. van Erp
Licensed Content Date	Dec 1, 2014
Licensed Content Volume	1
Licensed Content Issue	n/a
Licensed Content Pages	9
Start Page	8
End Page	16
Type of Use	reuse in a thesis/dissertation
Portion	figures/tables/illustrations
Number of 1 figures/tables/illustrations	
Format	both print and electronic
Are you the author of this Elsevier article?	No
Will you be translating?	No
Original figure numbers	Figure 1
Title of your thesis/dissertation	Ligand design for energy conversion and storage applications
Expected completion date	Nov 2019

Estimated size (number of 105  
pages)

Requestor Location	Mr. Joshua Heidebrecht
	Canada
	Attn: Mr. Joshua Heidebrecht
Publisher Tax ID	GB 494 6272 12
Total	0.00 CAD



This Agreement between Mr. Joshua Heidebrecht ("You") and John Wiley and Sons ("John Wiley and Sons") consists of your license details and the terms and conditions provided by John Wiley and Sons and Copyright Clearance Center.

License Number	4696650986842
License date	Oct 26, 2019
Licensed Publisher	Content John Wiley and Sons
Licensed Publication	Content Advanced Energy Materials
Licensed Content Title	Recent Trends, Benchmarking, and Challenges of Electrochemical Reduction of CO <sub>2</sub> by Molecular Catalysts
Licensed Content Author	Kamal Elouarzaki, Vishvak Kannan, Vishal Jose, et al
Licensed Content Date	May 9, 2019
Licensed Volume	Content 9
Licensed Content Issue	24
Licensed Content Pages	33
Type of use	Dissertation/Thesis
Requestor type	University/Academic
Format	Print and electronic
Portion	Figure/table
Number of figures/tables	1
Original figure/table number(s)	Wiley Figure 4
Will you be translating?	No
Title of your thesis /dissertation	Ligand design for energy conversion and storage applications
Expected completion date	Nov 2019
Expected size (number of pages)	105
Requestor Location	Mr. Joshua Heidebrecht

	Canada
	Attn: Mr. Joshua Heidebrecht
Publisher Tax ID	EU826007151
Total	0.00 CAD

Dear Joshua Ethan Heidebrecht,

Your permission requested is granted and there is no fee for this reuse. In your planned reuse, you must cite the ACS article as the source, add this direct link <https://pubs.acs.org/doi/abs/10.1021/acsenergylett.6b00049>, and include a notice to readers that further permissions related to the material excerpted should be directed to the ACS.

If you need further assistance, please let me know.

Sincerely,

Raquel Picar-Simpson  
ACS Publications Support  
Customer Services & Information  
Website: <https://help.acs.org/>

***Incident Information:***

**Incident #:** 3097478  
**Date Created:** 2019-10-26T15:31:14  
**Priority:** 3  
**Customer:** Joshua Ethan Heidebrecht  
**Title:** Reproducing a figure for use in my thesis –  
DOI: 10.1021/acsenergylett.6b00049